MONITORING DAMAGE IN CONCRETE USING DIFFUSE ULTRASONIC CODA WAVE INTERFEROMETRY

A Thesis
Presented to
The Academic Faculty

by

Dennis Patrick Schurr

In Partial Fulfillment
of the Requirements for the Degree
Master of Science in Engineering Science and Mechanics in the
School of Civil and Environmental Engineering

Georgia Institute of Technology
December 2010

MONITORING DAMAGE IN CONCRETE USING DIFFUSE ULTRASONIC CODA WAVE INTERFEROMETRY

Approved by:

Dr. Laurence J. Jacobs, Advisor
School of Civil and Environmental Engineering
Georgia Institute of Technology

Dr. Jin-Yeon Kim
School of Civil and Environmental Engineering
Georgia Institute of Technology

Dr. Karim G. Sabra
The George W. Woodruff School of Mechanical Engineering
Georgia Institute of Technology

Date Approved: August 19, 2010

ACKNOWLEDGEMENTS

Several people supported and helped me with this work, during my year at Georgia Tech as well as with the necessary preparations, and I want to express my sincere gratitude towards everyone. They made this work and my stay at Georgia Institute of Technology possible.

First of all, I want to thank Dr. Laurence J. Jacobs, who was a great advisor, teacher and friend. Thanks for holding up this remarkable exchange program, for all the help and support with organizational matters, academic questions and the encouragement towards this work.

I want to thank in particular Dr. Jin-Yeon Kim. Dr. Kim advised me during my whole research, he shared his deep-rooted knowledge, gave valuable hints, supported me with experiments, provided a very pleasant communication atmosphere and cheered me up when necessary.

My gratefulness goes towards Dr. Karim G. Sabra for fruitful discussions within the considered theory as well as good idea about the experiment setup.

A special thank goes to Prof. Dr.-Ing. Lothar Gaul from the Institut für Angewandte und Experimentelle Mechanik of the Universität Stuttgart for this outstanding exchange program I benefit from. I also want to thank Dipl.-Ing. Helge Sprenger, also Institut für Angewandte und Experimentelle Mechanik, for the effort he put into the organization of the exchange program. Further thanks go to Katja Striegel of the Zentrum für Internationale Angelegenheiten for advisory service and organizational matters. Furthermore, the generous financial support provided by the Deutscher Akademischer Austausch Dienst (DAAD) is greatly appreciated.

I want to express my gratitude towards the student Jun Chen for the help with the

mixing of the concrete samples and for the introduction of the compression machine and towards the student Robert Moser for useful hints for the compression machine. Of course, the workers of the machine shop of the Civil Engineering Department, who manufactured the fixtures and cones, are appreciated.

I would like to express my sincere gratefulness towards my fellow students and friends Thomas Ruiner and Frank Bender for the great time and fun we had together. Furthermore, I want to thank my labmates Katie Matlack, Krzysztof Leśnicki and Sang Ryul Kim for the nice working envorinment.

Finally, I would like to express my loving gratefulness to my family who encouraged me at all times. Your believe and support was the greatest contribution for my stay in the U.S.A.

TABLE OF CONTENTS

LIST OF TABLES

LIST OF FIGURES

LIST OF SYMBOLS OR ABBREVIATIONS

NDE	Nondestructive evaluation
CWI	Coda Wave Interferometry
ST	Stretching Technique
ASR	Alkali-Silica Reaction
HRSX	High-Reactive Sample X
LRSX	Low-Reactive Sample X

$A, a(t)$	Amplitude
a	Scatterer size
A, B	Constants
C_{ijkl}	Linear elastic material modulus (fourth order tensor)
c	Wave speed
c_L, c_T	Longitudinal and transverse wave speed
C_a	Medium constant
CC	Cross-correlation coefficient
$CC_k(\nu)$	Cross-correlation coefficient function
D	Diffusivity parameter
$\mathbf{d}$	Unit vector in direction of particle motion
dV	Differential volume
dt	Differential time delay
dV	Differential velocity delay
E	Young's Modulus
E_S, P_0	Signal Energy

f_l	body force
$f(t)$, f_0, f_1, f_m, Δf	Frequencies
G	Shear modulus
k, $\tilde{k}$, k''	Wavenumbers
K, K_0	Bulk modulus
k	Subscript holds for stress level
k_L, k_T	Longitudinal and transverse wave speed numbers
l, m, n	Murnaghan constants
l, r	Propagation distances
l, p	Spatial distances
l^*	Distance after which energy is randomized
j	Distance from data point to linear fit
n	Number of data points
n_j	Normal vector
$n(t)$	Distortion
$\mathbf{p}$	Unit vector in direction of propagation
R, T	Propagation distances
S	Surface
SD	Standard deviation
t_i	Traction vector
t_w	Center time of time window
T	Signal duration
t_a	Arrival time
U_P, U_{SV}, U_{SH}	Displacement of P-, SV- and SH-wave
$u(x,t)$	Displacement of harmonic waves
$\ddot{u}_l$	Acceleration
V_1, V_2, V_3	Wave velocity in 1-, 2- and 3-direction

V^0	Initial velocity
v_e	Average velocity of energy
V	Volume
W, H	Length and width of concrete specimen
x_1, x_2	Axis of (x_1,x_2)-plane
x, y, z	Coordinate axis
Z	Acoustic impedance
°C	Degree Celsius

α_a	Absorption parameter
α_s	Scattering attenuation coefficient
β	Second order (quadratic) nonlinearity parameter
δ	Third order (cubic) nonlinearity parameter
δ_{ij}	Kronecker delta
ϵ	Strain
ϵ_u	Max. Strain
ϵ_L, ϵ_W	Longitudinal and shear strain
ϵ	Relative time change
Γ	Domain of definition of ν
λ, μ	Lamé constants
λ	Wavelength
ν	Relative velocity change
ν	Poisson's ratio
ω	Circular frequency

$\Phi(t)$, $\phi(t)$	Amplitudes
ϕ, ψ_1, ψ_2, ψ_3	Potential functions
ψ_{in}, ψ_{out}	Input and Output signal-to-noise ratio
ρ, ρ_0	Mass density, mass density at initial state
σ_D	Dissipation rate
$\sigma_{0,c}$, f_c'	Compressive Strength
$\sigma_{0,t}$	Tensile Strength
σ, σ_0	Stress
σ_i, σ_r, σ_t	Incident-, reflected and transmitted wave
τ	Half bandwidth of frequency range
θ_1, θ_2, θ_3	Reflection angles
$\theta_{critical}$	Critical angle
∇	Nabla operator

SUMMARY

The prevalence of concrete and cement-based materials in the civil infrastructure plus the risk of failure makes structural health monitoring an important issue in the understanding of the complete life cycle of civil structures. Correspondingly, the field of nondestructive evaluation (NDE) has been maturing and now concentrates on the detection of flaws and defects, as well as material damage in early stages of degradation.

This defect detection is typically usually done by looking at the impulse response of the medium in question such as a cement-based material. The impulse response of a solid can be used to image a complex medium. Classically, the waveform is obtained by an active setup: an ultrasonic signal is generated at one location and recorded at another location. The waveform obtained from imaging can be used to quantitatively characterize the medium, for example by calculating the material's diffusivity coefficient or dissipation rate.

In recent years, a different monitoring technique has been developed in seismology to measure the velocity of different kinds of waves, the Coda Wave Interferometry (CWI). In this CWI technique, the main focus is given to the late part of the recorded waveform, the coda. CWI is now successfully used in seismology and acoustics.

In the current research, CWI is applied on concrete in different damage states to develop basic knowledge of the behavior of the wave velocity, and how it can be used to characterize cement-based materials. By comparing two impulse responses, the relative velocity change between the two impulse responses is used to characterize damage. Because of the stress-dependency of the velocity change, the calculations

can also be used to directly calculate the Murnaghan's and Lamé's coefficients. The newer technique of CWI is applied – the Stretching Technique (ST) [27]. The first goal of this research is to establish the viability of using CWI in cement-based materials. Next, we use the ST in the application of stress as we compress concrete samples for the detection of thermal damage, ASR-damage and mechanical softening.

CHAPTER I

INTRODUCTION

1.1 Motivation and Problem Description

In 2006, concrete and cement-based materials were, by volume, the largest manufactured product in the world [34]. Due to this prevalence, concrete applications in the civil infrastructure such as buildings, bridges, roads, parking garages and other structures are of special interest in structural health monitoring. As a result, the development of nondestructive evaluation techniques for concrete and cement-based materials is currently of significant interest and one critical area of research is to develop a quantitative evaluation of material damage in the microstructure of these materials.

An important class of work is the quantitative characterization of microcrack damage in the cement paste matrix. Microcrack damage may arise diverse causes, examples are alkali-silica reaction (ASR) damage which occurs around the world [11], thermal damage, and damage through dynamic loading. Recently, various ultrasonic measurement techniques have shown the capability to detect microcrack damage and to characterize material performance. Some techniques concentrate on the attenuation of the wave field traveling through the concrete, while another determines the specific parameters such as the diffusivity coefficient, D or the dissipation rate, σ_D as an indicator of material damage. In the diffuse field technique, Deroo et. all [15] recently demonstrated damage detection using ultrasound diffuse measurements in concrete specimens. The diffuse ultrasonic field is generated by the multiple scattering as the wave travels through the concrete. The degree of scattering depends on the wavelength and on the size and amount of the scatters. At first glance, the

measured diffuse field, and especially the late part of the diffuse field may appear as a jumbled clutter, as scientists believed for a long time. The reason for this is that the late part has traveled for much longer distances through the material than the first direct arrival, the so called ballistic wave.

In last several decades, scientists, especially seismologists, have started looking at the late part of diffuse fields, the so called coda waves, and found the waveform of the coda part to be consistent during multiple measurements [39] and then started comparing the different coda waves. During the recent past years, this idea has been developed to what is now known as Coda Wave Interferometry (CWI). More recent studies show the successful application of CWI in seismology, acoustics and engineering. The advantage of CWI when compared to other diffuse ultrasound measurement techniques is its high sensitivity to very small changes in the medium. Therefore, CWI is a promising new technique to monitor and characterize small cracks.

1.2 Coda Wave Interferometry

CWI is a technique that allows one to see differences in the coda part of a diffuse field. An ultrasonic wave introduced into concrete becomes highly scattered and becomes a diffuse field. Typically, diffuse fields can be separated into two parts: the first arrival, that consists of waves that directly travel the shortest path from source to receiver, and the diffuse part which includes the late coda contribution. The diffuse waves have traveled much longer paths through the medium than the first arrival does, due to multiple scattering [6], so they arrive at the receiver at much later times. The later they arrive, the longer is the path that they travel and the more they interact with the microstructure of the medium.

Because of their relatively long paths, diffuse waves are more sensitive to small changes in the medium. Consequently, diffuse waves carry more information than the first arrival. CWI concentrates on this late, diffuse coda part. The CWI technique

compares two different time series of coda waves with each other, and then determines the degree of correlation between them.

There are two different CWI techniques: the doublet technique [38], which was developed first, and the Stretching Technique (ST). This research employs the ST. The ST is more advanced than the doublet technique and stretches the time axis of a waveform by scaling it. As the time axis gets stretched, the relative time change with respect to the time axis of the original waveform can be obtained. Due to the proportionality between time and velocity, the relative velocity change can be calculated from the scaling factor. The goal of the ST is to stretch one waveform with a relative velocity change factor in a way that the stretched waveform has much in common with a second waveform, e.g. is correlated.

1.3 Research Objective

The first objective of this research is to develop the ST for cement-based materials, specifically developing a reliable and repeatable measurement setup, plus the data processing to get consistent results. To confirm the accuracy of this procedure, these results are compared with those of Larose et. al [27].

The second objective of this research is to determine the basic relationships between different damage types and the relative velocity change. The CWI will be applied to monitor damage in concrete such as thermal damage, ASR-damage and damage through mechanical loading. The work conducted during this study serves as a foundation for future research efforts towards the goal of developing a quantitative NDE method for structural health monitoring.

1.4 Background Information

CWI has undergone a long development process and the newest version of it is the ST. In 1956, K. Aki [2] termed the multiple scattering in the earth as “coda”. Poupinet et al. [39] developed a method for monitoring velocity variations in the coda from the

same earthquake source and named it "doublets," which refers to two nearly identical signals obtained from two closely spaced sensors. He also proposed to use coda waves to monitor velocity changes in scattering media. Roberts et al. [40] used the "doublets" for laboratory experiments in 1992. They monitored changes in attenuation and called it the "active doublet method." Also, in the fields of helioseismology [16] and acoustics [47, 29], it was shown that information can also be extracted from diffuse coda waves. Snieder et. al [43] determined the nonlinear dependence of seismic velocity in granite using the doublet technique and called it for the first time coda wave interferometry. The further development of the doublet technique was done in [30] and [42]: their idea is to interpolate the coda at different moments with various relative velocity changes in order to maximize the correlation of two waveforms. This technique is called the stretching technique and is used in this research.

CWI techniques, the Stretching Technique and the Doublet Technique have their advantages and disadvantages which will be discussed later. Larose et. al [27] employed the ST on concrete to determine the nonlinearity parameter β. Payan et. al [38] employed the doublet technique to investigate differences of velocity changes of shear- (polarized in two different directions) and longitudinal waves.

1.5 Previous Work

Research conducted on CWI is highlighted by Larose [27] and Payan [38]. Larose showed in [26] the possibility of measuring temperature changes using CWI in a concrete structure. He used a vibrating system to introduce waves into a the concrete floor of a room. With an air conditioning device, he changed the temperature of the room, e.g. the concrete floor and made measurements after the temperature change. For the change of 3°C, he noticed a change in dilation e.g. relative velocity of ν=0.45%. In [27], Larose determined the nonlinearity parameter β of a concrete cylinder using CWI. He placed the ultrasonic source and receiver on the cylinder at

the same vertical height and in the horizontal plane the angle between them was 90°. By compressing the cylinder in a step of 50 kPa, starting from 5 MPa and ending at 5.5 MPa, he received velocity changes in the coda. Using Kelly's expressions [21] for the speed of elastic waves in a stressed solid, Larose calculated β. Also, Larose investigated the stability of monitoring weak changes in multiply scattering media [19] for the sake of reconstructing the Green's Function.

Payan et al. [38] achieved different relative velocity changes for different kind of source waves in a concrete cylinder. Source and receiver were attached at the same height and at opposite sides of the cylinder sample. He found that wave polarized in the direction of the applied stress, that was a shear wave, is more sensitive than the pressure- and the other shear wave, both of which were not polarized in direction of the stress. Therefore he used different transducer types. The result is a greater slope of the relative velocity change of the shear wave with polarization in stress direction. According to their results, the big difference between the two shear waves are because the coda waves carry polarization information due to stress-induced birefringence. Meanwhile Larose used as a source signal, a chirp waveform of a few seconds duration, while Payan used a short impulse. Furthermore, Larose used the ST to evaluate his results and Payan used the Doublet Technique. Differences will be discussed later.

1.6 Structure of this Thesis

This Thesis is organized as follows. Chap. 2 describes the material concrete. Some basic knowledge and different damage types such as ASR-damage, thermal damage and mechanical damage are discussed. Furthermore, the phenomena of creep and slow dynamics are presented due to their occurrence at the compression of concrete, which is done in this research. In Chap. 3, a brief survey of wave propagation is given introducing some general technical terms and explain general wave phenomena, which will help develop an intuitive understanding of wave propagation in elastic

solids. This is important for understanding all of the following chapters. In Chap. 3.4, the concept of Pulse Compression is explained. Chap. 4 explains CWI: the Stretching Technique. The theoretical background of ST and the differences of ST and Doublet Technique are presented. Next, Chap. 5 presents the experimental procedure conducted in this research. The used instrumentation, the measurement setup and the measurement procedure are explained. Chap. 6 discusses the results. Finally, in Chap. 7, conclusion and outlook are given.

CHAPTER II

CEMENT BASED MATERIALS

The material used in this thesis is concrete. Concrete is a highly complex material, both in chemical and mechanical viewpoints. It is permeable, porous, heterogeneous and elastically nonlinear. Concrete, as one type of cement-based material, is a multi-phase material. Ultrasonic waves traveling through concrete experience attenuation as well as multiple scattering, because of different ingredient sizes, which causes a diffuse wave field. This chapter introduces typical properties of concrete, types of damage and some aspectes of material behavior.

2.1 Composition and Properties

The ASTM C 125 [3] defines terms and definitions relating to concrete as well as ACI Committee 116 does. The following terms are commonly known in the field of concrete:

Concrete: A mixture that consists essentially of a binding medium within which are embedded particles for fragments of aggregate: fine aggregate (sand), coarse aggregate (gravel) and the cement paste as the binding medium.

Aggregate: Granular Material such as sand, gravel or crushed stone. Coarse aggregate refers to aggregate particles larger than 4.75 mm and fine aggregate refers to aggregate particles smaller than 4.75 mm.

Cement paste: A mixture of cement and water. The water-cement ratio depends on the desired properties. Cement is commonly known as Portland cement

Mortar: A mixture of fine aggregate and cement paste.

Concrete can be classified in many ways [34], for example based on unit weight,

Table 2.1: Typical properties of moderate-strength concrete

Property	Symbol	Value
Compressive strength	σ_{0c}	35 MPa
Tensile strength	σ_{0t}	3 MPa
Young's modulus	E	28 GPa
Poisson's ratio	ν	0.18
Density	ρ	1300 kg/m^3
Strain at failure	ϵ_u	0.001

which is more common in the United States. Concrete weighing about 2400 kg/m^3 is called normal weight concrete. Lightweight concrete refers to concrete weighing less than 1800 kg/m^3 and heavyweight concrete refers to more than 3200 kg/m^3. More common in Europe is the classification through concrete strength: Low-strength concrete (less than 20 MPa), moderate-strength concrete (20-40 MPa) and high-strength concrete (more than 40 MPa) are known.

2.2 Alkali-Silica Reaction Damage

The Alkali-Silica Reaction (ASR) occurs when alkali hydroxides and silica form a gel which may cause cracking. Potassium (K^+) and sodium (Na^+) are alkali metal cations found in concrete [46]. Concrete is a porous material, and in the pores concrete contains the oxides of those cations, that are K_2O and Na_2O. The alkali metals are mostly introduced in concrete through the cement, and sometimes through the aggregates [25]. K_2O and Na_2O react with H_2O and form a hydroxyl ion (OH^-) concentration with pH-values in the range of 12.5 - 13.5. Some forms of silica (SiO_2) in the concrete is unstable at high pH-values and react with hydroxyl ions forming the alkali-silica reaction gel [25]. This gel absorbs water producing a pressure in the cement paste and aggregate, which may lead to expansion of the structure and to cracking of the cement paste and the aggregate.

Applying a high temperature on the concrete sample accelerates the ASR reaction as shown in [22]. Ideker et al. applied a temperature of 60°C to shorten the ASR time

by 75%. In this Thesis, 2 concrete specimens were put in an oven at 60°C to accelerate ASR. Those samples contain, not like other specimen used in this research, the high reactive ingredient Spratt. Spratt reacts faster in terms of ASR. The specimens used in this thesis will be presented in Sec. 5.1.6

2.3 Thermal Damage

Thermal Damage occurs when water evaporates in the concrete causing an increasing of porosity and microcracks [37]. As mentioned earlier, the cement paste of concrete consists of a distinct water cement ratio to achieve certain desired properties. Water-cement ratios vary normally from 0.3 - 0.7. It is known that the lower the ratio is, which means the less water the concrete contains, the higher the strength is but the more porous the concrete is. In [37], concrete is heated up to temperatures of 105°C and higher, causing as a first step free water evaporation followed by dehydration. As the concrete was heated up, more and more microcracks were detected. The process of Thermal Damage is well understood and can be found for example in [10].

2.4 Mechanical Damage

Mechanical Damage, that means damage through an applied load, is one possible failure. The compressive strength of concrete is called f_c' and is the highest strength before failure. Concrete constructions are normally supposed to be loaded about up to 30%-40% of their compressive strength. A higher load would mean a failed construction in terms of seizing and may result in a collapse of the whole structure as happened in June 2010 in Atlanta Midtown, as a whole parking deck collapsed.

According to [34], the stress strain relationship can be seen proportional for 30% of the ultimate strength f_c', as shown in Fig. 2.1: the 30% proportionality. The whole σ-ϵ relationship is nonlinear and can be expressed as follows [13]:

$$\sigma = E\epsilon(1 + \beta\epsilon + \delta\epsilon^2 + ...) \tag{2.1}$$

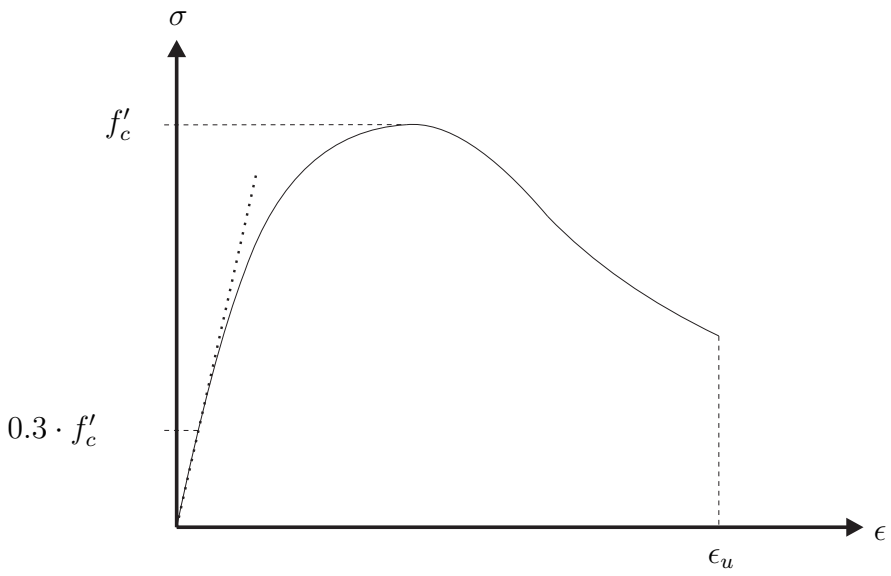

Figure 2.1: Typical Stress-Strain Relationship of Concrete for uniaxial Loading.

where E is the Young's Modulus for uniaxial compression, β quadratic nonlinearity parameter, δ the cubic nonlinearity parameter and so on.

Between the range of 30% and 50% of f'_c the microcracks extend due to stress concentration at the crack tips in the interfacial transition zone, but no cracking occurs in the mortar matrix. Also, crack propagation seems to be stable within this range, that means crack length reaches their final length very guickly if the applied stress is held constant. Between 50% and 75%, the crack system tends to get more unstable. Above 75% of f'_c, crack propagation will be accelerated in the unstable system and complete fracture of the concrete can occur.

Another phenomena is the softening of concrete. If a concrete gets compressed several times with no waiting time in between each compression, the Young's Modulus changes [34] as shown in Fig. 2.2. The concrete gets softened resulting in a reduced Young's modulus. A too strong compression can result in plastic deformation and can be also seen in Fig. 2.2

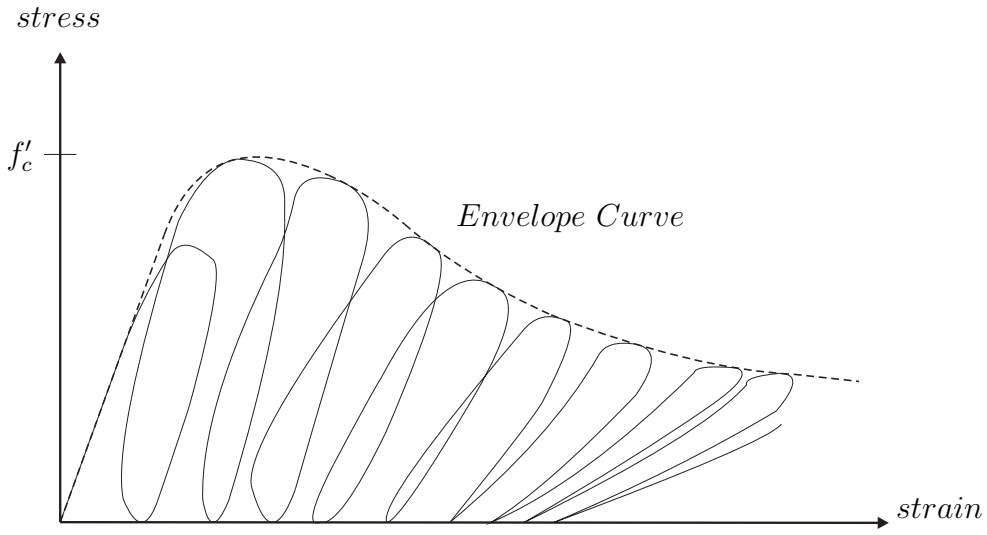

Figure 2.2: Concrete Response to Repeated Uniaxial Loading.

2.5 Slow Dynamics

The effect of slow dynamics was found in consolidated materials such as rocks, damaged materials, concrete and composites [45]. It refers to the change of the Young's Modulus over long time. After concrete is softened by large strain in the elastic response, the Young's modulus has a time-dependent recovery until it reaches its initial value again [9]. For plasticity, this is not valid. Slow dynamics may be seen as the relaxation of the specimen back to its state before stress was applied, but it takes much longer time than the ordinary relaxation. According to [45], the full recovery of the Young's modulus can take minutes to hours, depending on the time on which the strain was applied. Both [45, 9] find the recovery time to be logarithmic e.g. log(time). In [45], the full recovery time was found to be around 2500 seconds of the used specimen, 90% of the Young's Modulus was already recovered after around 500 seconds.

2.6 Creep

Creep is a viscoelastic phenomena that leads to a time-dependent change of the strain when stress is applied [34]. As a concrete is constantly loaded with a stress σ, the strain ϵ will not stay the same for all time. It will increase slightly over time, depending on the magnitude and duration of the load.

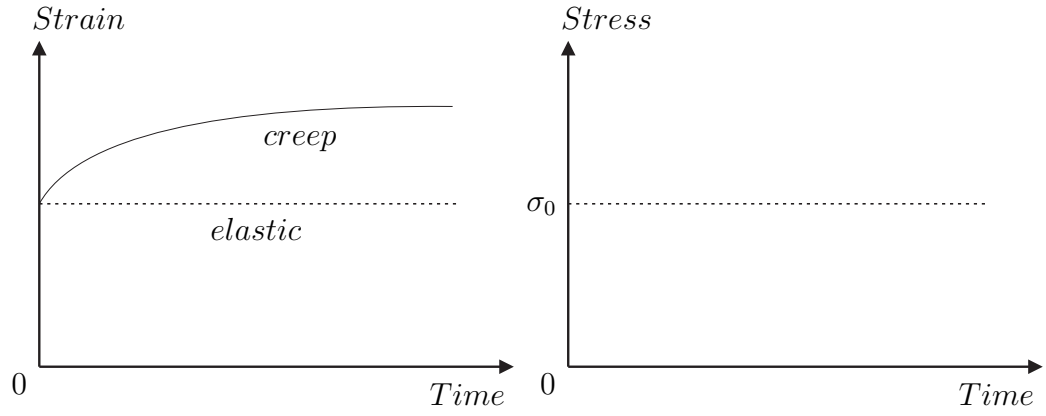

Figure 2.3: Creep over time through constant loading

The removal of absorbed water from the hydrated cement paste [34] is the main reason for creep, what leads to microstrain. This takes into account at long time loading in the order of weeks and years. Secondly, when a concrete sample is compressed to a value greater than 30 to 40 percent of the ultimate stress, some microcracks in the interfacial transition zone start to appear and contribute partly to creep. Thirdly, the delayed elastic response in the aggregate contributes towards creep. After unloading, creep recovery occurs much faster than creep.

CHAPTER III

THEORETICAL BACKGROUND

In this chapter, some fundamentals of the theory of linear elastic wave propagation are provided as well as some important wave phenomena such as reflection and attenuation are described. The governing equations of wave motion are derived and their basic solutions for specific boundary conditions are provided. Mathematical descriptions for reflection and attenuation are discussed. Further information on the topic of wave propagation can be found in numerous sources such as [1, 18]. Next, a short introduction in continuum mechanics followed by the formula for the wave speed in a stressed solid is derived. References can be found in [21, 32]. Furthermore, the technique of pulse compression is explained.

3.1 Wave Propagation

3.1.1 Linear elasticity and equation of motion

In the theory of linear elasticity, the traction vector t_i on a plane described by $n_i x_i = d$ is given by

$$t_i = \sigma_{ji} n_j, \tag{3.1}$$

where σ_{ji} is the stress tensor and n_j is the normal vector perpendicular to the plane.

In an elastic solid, the equations of motion can be derived by the application of the principle of linear momentum to a three-dimensional free body. The free, arbitrary body has the volume V and the Surface S, is supposed to be continuous and has the mass density ρ, as shown in Fig. 3.1. Thus, the balance of linear momentum can be stated in index notation as

$$\int_S \sigma_{kl} n_k \mathrm{d}S + \int_V \rho f_l \mathrm{d}V = \int_V \rho \ddot{u}_l \mathrm{d}V, \tag{3.2}$$

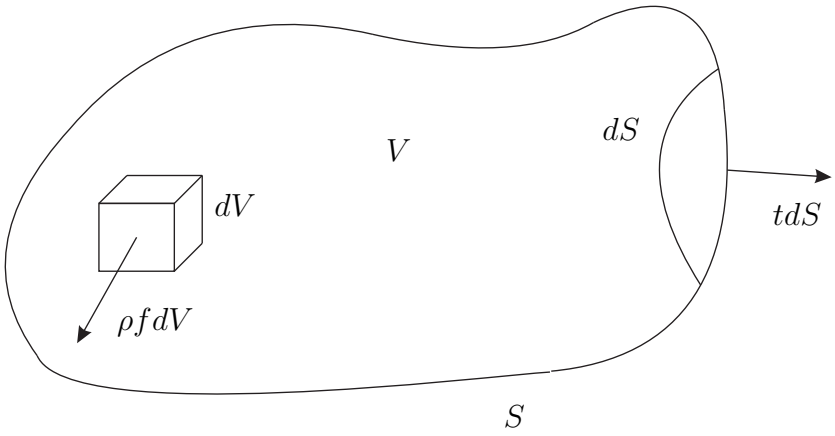

Figure 3.1: Balance of linear momentum.

where f_l is the body force and $\ddot{u}_l$ is the acceleration of a small volume dV in the body V. Using the Gauss' theorem for the first term of Eq. 3.2, the equation can be expressed as

$$\int_V (\sigma_{kl,k} + \rho f_l - \rho \ddot{u}_l) \mathrm{d}V = 0. \tag{3.3}$$

Because Eq. 3.3 is valid for an arbitrary shape, one obtains for a continuous integrand

$$\sigma_{kl,k} + \rho f_l = \rho \ddot{u}_l \tag{3.4}$$

or in vector notation

$$\nabla \cdot \sigma + \rho f = \rho \ddot{u}. \tag{3.5}$$

This is Cauchy's first law of motion. This equation contains the stress tensor σ and the displacement u_l. In the field of wave propagation, it is more convenient to describe Eq. 3.4 solely in terms of u_l and shall be considered next.

Generally, the linear relationship between the stress tensor and the strain tensor is given by

$$\sigma_{ij} = C_{ijkl} \epsilon_{kl} \tag{3.6}$$

where C_{ijkl} is a fourth-order tensor. For an elastic and homogeneous medium the

coefficients of are C_{ijkl} constant, and according to [1] they can be expressed as

$$C_{ijkl} = \lambda\delta_{ij}\delta_{kl} + \mu(\delta_{ik}\delta_{jl} + \delta_{il}\delta_{jk}). \tag{3.7}$$

Plugging Eq. 3.7 into Eq. 3.6 yields

$$\sigma_{ij} = \lambda\epsilon_{kk}\delta_{ij} + 2\mu\epsilon_{ij}, \tag{3.8}$$

where λ and μ are known as the two independent elastic constants or Lamé constants. The strain tensor ϵ_{ij} is related to the displacement u_i by

$$\epsilon_{ij} = \frac{1}{2}(u_{i,j} + u_{j,i}) \tag{3.9}$$

or in vector notation

$$\epsilon = \frac{1}{2}(u\nabla + \nabla u). \tag{3.10}$$

Neglecting the body force f, substituting Eq. 3.9 into Eq. 3.8 and subsequently into Eq. 3.4 leads to Navier's equations of motion

$$\mu u_{i,jj} + (\lambda + \mu)u_{j,ji} = \rho\ddot{u}_i \tag{3.11}$$

Alternatively, this system of three coupled partial differential equations (PDE) may be expressed in vector notation as

$$\nabla^2 u + (\lambda + \mu)\nabla\nabla u = \rho\ddot{u}_i. \tag{3.12}$$

This PDE, completed by an appropriate set of boundary conditions and initial conditions, describes the problem of wave propagation in linear elastic solids. In general, it is hard to solve the three partial differential equations, because it has the feature that it couples the three displacement components, but can be uncoupled using the Helmholtz decomposition. The Helmholtz decomposition uses the scalar potential function φ and three vector potential functions ψ_1, ψ_2 and ψ_3, which have to satisfy the decomposition of the displacement of the form

$$u = \nabla\varphi + \nabla \times \psi. \tag{3.13}$$

This represents a decomposition of the displacement into an irrotational or curl-free part, expressed in the first term, and a solenoidal or divergence-free part, stated in the second term. It should be noted that Eq. 3.13 relates three components of displacement to four potential functions. That means an additional constraint for φ and ψ is necessary for definiteness. Normally, the relation

$$\nabla \cdot \psi = 0 \quad or \quad \psi_{i,i} = 0 \tag{3.14}$$

is taken as an additional constraint condition [1]. Plugging Eq. 3.13 into Naviers equation 3.12 becomes

$$\mu\nabla^2[\nabla\varphi + \nabla \times \psi] + (\lambda + \mu)\nabla\nabla \cdot [\nabla\varphi + \nabla \times \psi] = \rho\frac{\partial^2}{\partial t^2}[\nabla\varphi + \nabla \times \psi]. \tag{3.15}$$

Using the vector identities $\nabla \cdot \nabla \times \psi = 0$ and $\nabla \cdot \nabla\varphi = \nabla^2\varphi$, Eq. 3.15 yields

$$\nabla[(\lambda + 2\mu)\nabla^2\varphi - \rho\ddot{\varphi}] + \nabla \times [\mu\nabla^2\psi - \rho\ddot{\psi}] = 0. \tag{3.16}$$

It can be seen that Eq. 3.16 is satisfied when the two uncoupled wave equations

$$\nabla^2\varphi = \frac{1}{c_L^2}\ddot{\varphi} \quad and \quad \nabla^2\psi = \frac{1}{c_T^2}\ddot{\psi}, \tag{3.17}$$

hold, where c_L represents the wave speed of the longitudinal wave and c_T stands for the wave speed of the vertically and horizontally polarized shear waves. The two wave speeds can be expressed in terms of the mass density ρ and the Lamé constants λ and μ as

$$c_L = \sqrt{\frac{\lambda + 2\mu}{\rho}} \quad and \quad c_T = \sqrt{\frac{\mu}{\rho}} \tag{3.18}$$

As it can be seen from Eq. 3.18, it always holds true that the longitudinal wave is faster than the shear wave, i.e. $c_L > c_S$. Relationships from the Lamé constants λ and μ to the more commonly used material properties Young's Modulus E and Poisson's ratio ν are given by

$$\lambda = \frac{E\nu}{(1 + \nu)(1 - 2\nu)} \quad and \quad \mu = \frac{E}{2(1 + \nu)}, \tag{3.19}$$

or

$$E = \frac{\mu(3\lambda + 2\mu)}{\lambda + \mu} \quad and \quad \nu = \frac{1}{2}\frac{\lambda}{\lambda + \mu}. \tag{3.20}$$

The literature sometimes also uses the bulk modulus which is defined by

$$K = \lambda + \frac{2}{3}\mu \tag{3.21}$$

In analogy to the horizontal and vertical wave speeds, one defines the horizontal and vertical wave speed numbers as

$$k_L = \sqrt{\frac{\omega}{c_L}} \tag{3.22}$$

$$k_T = \sqrt{\frac{\omega}{c_T}} \tag{3.23}$$

3.1.2 Wave phenomena

The wave phenomena discussed in the following sections are based on the assumption of a plane wave meaning a wave with constant properties (ϵ, σ, u) on a plane perpendicular to its propagation direction, $\mathbf{p}$. The mathematical representation of a plane wave is given by

$$u = f(x \cdot \mathbf{p} - ct)\mathbf{d} \tag{3.24}$$

where $\mathbf{d}$ is the unit vector defining the direction of particle motion, called polarization c is either the longitudinal wave speed c_L or the shear wave speed c_T, and f is an arbitrary function that defines the shape of the traveling wave. It can easily be shown that any function of the form $f(x \cdot \mathbf{p} - ct)$ satisfies the Navier's equation of motion. Substitution Eq. 3.24 into the Eq. 3.12 yields

$$(\mu - \rho c^2)\mathbf{d} + (\lambda + \mu)(\mathbf{p} \cdot \mathbf{d})\mathbf{p} = 0. \tag{3.25}$$

The two types of waves that form the basis of the wave propagation theory are obtained by the two possible solutions of the above equation. Since $\mathbf{p}$ and $\mathbf{d}$ are different unit vectors, either $\mathbf{d} = \pm\mathbf{p}$ or $\mathbf{p} \cdot \mathbf{d} = 0$ are possible solutions:

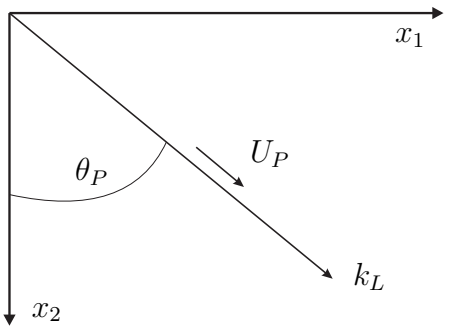

Figure 3.2: Directions of polarization and propagation of a P wave.

1. $\mathbf{d} = \pm\mathbf{p}$ leads to $\mathbf{p} \cdot \mathbf{d} = \pm 1$. In this case and together with Eq. 3.25, one obtains $c = c_L$ as defined in Eq. 3.18. Since $\mathbf{d}$ and $\mathbf{p}$ are linearly dependent, this describes a particle motion in the direction of propagation which therefore describes a longitudinal or compressive (P) wave, as shown in Fig. 3.2.

2. $\mathbf{p} \cdot \mathbf{d} = \pm 0$ leads to $c = c_T$ as defined in Eq. 3.18. In this case, the particle motion and the direction of propagation are perpendicular to each other which is described by the term transverse wave. Considering a two dimensional plane ((x_1, x_2) plane), a wave with an in-plane displacement is called an SV-wave (vertically polarized), while a wave with an out-of-plane displacement is called an SH-wave (horizontally polarized). Both are shown in Fig. 3.3.

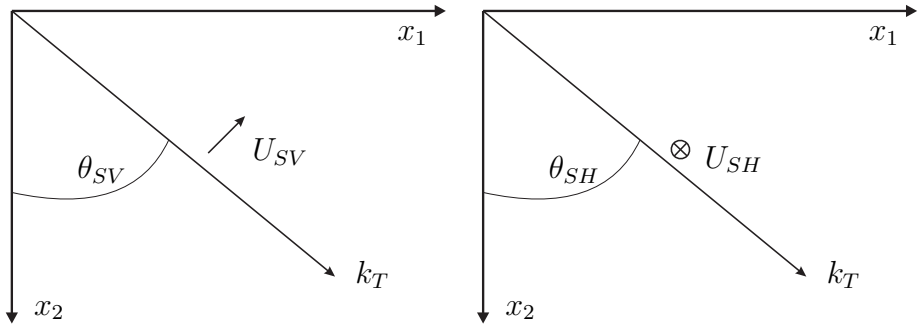

(a) Displacement of SV wave (b) Displacement of SH wave

Figure 3.3: Directions of particle motion and propagation of SV and SH wave

3.1.3 Harmonic waves

The discussed shape of the traveling waveform $f(x \cdot p - ct)$ in the previous section can be of arbitrary form. Nevertheless, it is very often convenient to consider a specific form of waves which show harmonic behavior in time and space and are discussed in the following for 1-D case. A reason for harmonic waves is the practical use, because they can be generated with transducers. Another reason is the mathematics, which becomes a lot easier. The displacement u of a harmonic wave can be described by

$$u(x,t) = A\cos[\omega(\frac{x}{c} - t)] \tag{3.26}$$

where A is the amplitude and $\omega = 2\pi f$ the circular frequency of the wave. Eq. 3.26 can also be written in a complex exponential expression

$$u(x,t) = Ae^{i(kx-\omega t)}, \tag{3.27}$$

where k is the wavenumber of the harmonic wave and is defined as

$$k = \frac{\omega}{c} = \frac{2\pi f}{c} = \frac{2\pi}{\lambda} \tag{3.28}$$

with wavelength λ. The term $(kx - \omega t)$ in the exponent represents the phase of the wave.

In homogeneous, isotropic materials of infinite extent, longitudinal and shear phase velocities c_L and c_T are constant, that is, the waves are nondispersive and means not a function of the circular frequency ω, e.g. are independent. Nevertheless, in more complex materials, this is not the case any more and a dispersion-relationship between frequency and phase velocity has to be found. These media are said to be dispersive.

3.1.4 Reflection and Transmission of One-dimensional waves

Reflection and transmission of traveling disturbances occur when the waves hit an ideal interface of two elastic media with different acoustic properties. Specifically,

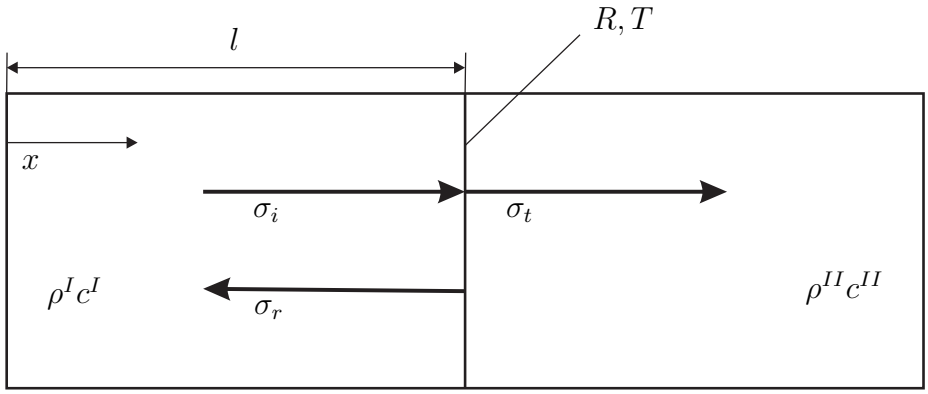

Figure 3.4: Reflection and Transmission of One-dimensional waves.

this properties are defined by the acoustic impedance $Z = \rho c$, i.e. the product of mass density and the phase velocity of the type of wave considered. An impedance missmatch of two joined materials causes a reflected and transmitted portion of the incident wave. This process is illustrated in Fig. 3.4. According to [1], an incident wave σ_i can be written as

$$\sigma_i = f(t - \frac{x}{c}). \tag{3.29}$$

The reflected and transmitted waves can be expressed in terms of the incident wave, which yields

$$\sigma_r = Rf(t - \frac{l}{c} + \frac{x - l}{c}) \tag{3.30}$$

and

$$\sigma_t = Tf(t - \frac{l}{c} + \frac{x - l}{c}). \tag{3.31}$$

for times $t \geqq \frac{l}{c}$ and propagation distance l. R is the reflection coefficient while T is the transmission coefficient. Applying the conditions of stress and displacement continuity at the interface [1], the coefficients are determined to be

$$R = \frac{Z_2 - Z_1}{Z_1 + Z_2} \tag{3.32}$$

and

$$T = \frac{2Z_2}{Z_1 + Z_2}. \tag{3.33}$$

For the limit cases, one obtains that $-1 \leq R \leq 1$ and $0 \leq T \leq 2$. Specifically important is the reflection from a stress-free surface where the neighboring media cannot carry any mechanical waves, i.e. $Z_2 = \rho^{II} c^{II} \to 0$. In this case the reflected form remains in the same shape as the incident one but its sign changes upon reflection. Thus, the reflection and transmission coefficients take the values $R = -1$ and $T = 0$.

3.1.5 Reflection of Two-dimensional P and SV waves

Considering an unbounded and infinite media, P and SV waves propagate independently of each other. Reflection and coupling of the waves occur at the interfaces of materials with different acoustic properties, that are ρ and c. An incident P wave, which is reflected at a stress free boundary, that means $\sigma_{21} = \sigma_{22} = 0$, and the reflected wave normally consists of both, a P wave and a SV wave. In the same manner, a SV wave reflected at a stress free boundary as a P wave and a SV wave. Fig. 3.5 shows the reflections of an incident P and SV wave.

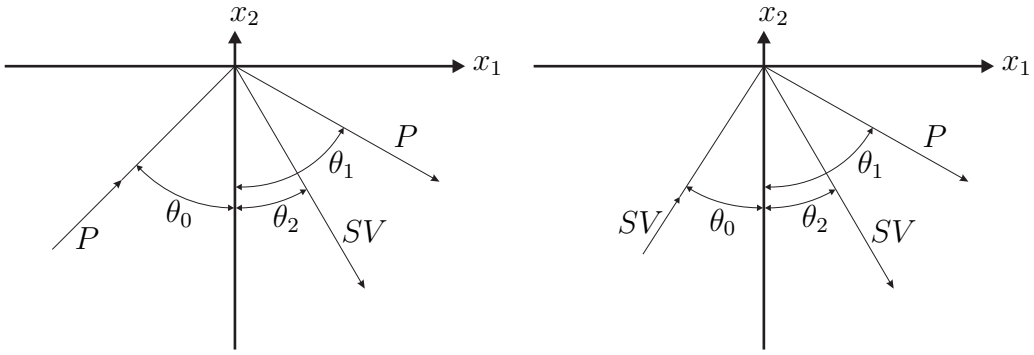

(a) Reflection of a P wave (b) Reflection of a SV wave

Figure 3.5: Wave reflections

The effect that a single type of incident wave reflects as two different waves is called mode conversion. For the plane-strain case of a harmonic wave travelling in the unbounded $(x1, x2)$-plane, a mathematical description of the displacement field is given by

$$u^{(n)} = A_n \mathbf{d}^{(n)} e^{ik_n(x_1 p_1^n + x_2 p_2^n - c_n t)}, \tag{3.34}$$

where n denotes the wave type, longitudinal or transverse, k_n the respective wavenumber, c_n the respective wavespeed, and $\mathbf{d}^{(n)}$ the respective unit vector. According to these definitions, together with the assumption that the angular frequency ω for the incident and reflected wave is equal, one can determine the relationship between the angle of the incident wave and the angles of the reflected waves. These relationships are given in Tab. 3.1.

Table 3.1: Angle relations for reflection on a stressfree surface

Incident (θ_0)	**Reflected P** (θ_1)	**Reflected SV** (θ_2)
P	$\theta_1 = \theta_0$	$\sin\theta_2 = (c_T/c_L)\sin\theta_0$
SV	$\sin\theta_1 = (c_L/c_T)\sin\theta_0$	$\theta_2 = \theta_0$

Non-trivial amplitudes A_n can be obtained if the angles of the incident and reflected waves, θ_0, θ_1 and θ_2 (as defined in Fig. 3.5) satisfy Snell's law of reflection

$$k_0 \sin(\theta_0) = k_1 \sin(\theta_1) = k_2 \sin(\theta_2) \tag{3.35}$$

There are two exceptions to mode conversion. The first is normal incidence with $\theta_0 = 0$. In this case, the waves are reflected as themselves. If the angle θ_0 is greater than a critical angle,

$$\theta_{\text{critical}} = \arcsin\left(\frac{c_{\text{T}}}{c_{\text{L}}}\right), \tag{3.36}$$

then only an SV-wave is reflected. The P-wave part of the reflected signal is then degenerated into the Rayleigh surface wave that travels along the surface with exponentially decreasing amplitude in the negative x_2-direction.

3.2 Attenuation

Ultrasonic waves travelling through concrete experience attenuation. This section will present an introduction regarding attenuation, including several attenuation mechanisms and their underlying physics as well as the mathematical representation of attenuation will be shown.

Usually, attenuation is incorporated in the wave propagation model that was discussed earlier by defining a complex wave number $\tilde{k}$. Extending Eq. 3.28, the complex wavenumber is defined as

$$\tilde{k} = \frac{\omega}{c} + i\alpha = k + i\alpha \tag{3.37}$$

where α denotes the attenuation coefficient. Additionally, it is also possible to define complex wavespeed and complex material properties.

The displacement field which experiences attenuation for a one-dimensional, plane and harmonic wave can be obtained by plugging Eq. 3.37 into Eq. 3.24 which yields

$$u(x,t) = Ae^{i(\tilde{k}x-\omega t)} = Ae^{-\alpha}e^{i(kx-\omega t)}. \tag{3.38}$$

One can now clearly see the effect of the attenuation. The first part of Eq. 3.38 describes an exponential decay in the direction of propagation and the second term is for the harmonic behavior.

The complex wavespeed can be derived by plugging Eq. 3.37 into the dispersion equation Eq. 3.28, and after transposing one obtains

$$c_L = \frac{\omega}{\tilde{k}} = \frac{\omega}{k + k''i\omega}, \tag{3.39}$$

where k is the real part of the wavenumber and $k''\omega$ is α. Eq. 3.39 shows that the wavespeed depends on the frequency, that means dispersion arises or in other words, different frequencies travel with different wavespeeds. Non-geometric attenuation is linked to wave-velocity dispersion by the Kramers-Kronig relationship.

In the following, several different attenuation mechanisms will be explained.

3.2.1 Viscoelastic material behavior - Absorption

In the theory of elasticity, it is assumed that an elastic material stores energy without dissipation during deformation. That is true for a number of materials such as steel or aluminum, which are only dissipative for very high ultrasonic frequencies. But there are also materials of technical interest such as cement-based materials or composites that dissipate nonegligible part of the stored energy also at lower frequencies. Those materials are called viscoelastic since they combine the properties of an elastic solid and a viscous liquid.

During deformation, a part of the energy in these materials is converted into heat due to internal friction which causes an ultrasonic wave to lose some of its energy resulting in a lower amplitude. This attenuation mechanism is also known as material absorption. The absorption in viscoelastic materials is usually assumed to be linearly dependent on the frequency in the range of ultrasound frequencies, and is called hysteresis absorption [41].

The material absorption of a specific material is usually incorporated into the theory of attenuation by applying a material absorption parameter

$$\alpha_a = \frac{C_a}{\lambda}, \tag{3.40}$$

where C_a is a medium constant.

3.2.2 Geometric Spreading

The effect of a decreasing ultrasonic wave due to spreading is called geometric attenuation. This effect is independent of frequency. It depends on the wave mode and the geometry of the investigated elastic body. As an example, Rayleigh surface waves are attenuated by $\frac{1}{\sqrt{r}}$ where r is the propagation distance of the wave. This attenuation type is intrinsic in the wave equation. In the strictest sense, geometric spreading is not counted as attenuation since there is no energy loss associated with it.

3.2.3 Scattering

Another important mechanism of attenuation arises during the course of scattering. In heterogeneous materials, waves are scattered at the interfaces of phases with different acoustic properties. These interfaces can be associated with the grain structure, crystal defects or multiple phases of inclusions within the material, i.e., any inhomogeneity of the material can give rise to wave scattering.

Based on the ratio of scatterer size a and wavelength λ, different domains are distinguished to have different approximations for the frequency dependence of the attenuation coefficient [23], and in each domain the scattering attenuation coefficient $\alpha_{\mathrm{s}}(\lambda, \alpha)$ can be written as follows.

1. In the Rayleigh domain, when the wavelength λ is much longer than the scatterer size a, the following functional form is found:

$$\alpha_{\mathrm{s}}(\lambda, a) \propto \frac{a^3}{\lambda^4} \text{ for } \lambda \gg a \tag{3.41}$$

2. In the stochastic domain, with wavelength of the order of the scatterer size, the following functional form is found.

$$\alpha_{\mathrm{s}}(\lambda, a) \propto \frac{a}{\lambda^2} \text{ for } \lambda \approx a \tag{3.42}$$

3. In the geometric domain, when the wavelength is much smaller than scatterer size, the following functional form is found.

$$\alpha_{\mathrm{s}}(\lambda, a) \propto \frac{1}{a} \text{ for } \lambda \ll a \tag{3.43}$$

The total attenuation is found to be the addition of the previously discussed effects of material absorption and scattering. Thus, the total attenuation can be written as

$$\alpha(\lambda, a) = \alpha_{\mathrm{a}}(\lambda) + \alpha_{\mathrm{s}}(\lambda, a) \tag{3.44}$$

3.3 The acoustoelastic Effect

In this research, stress is applied on concrete and the relative velocity change between reference and stressed state is obtained.

The stress/strain and wave velocity relationship is known as the acoustoelastic effect. Kelly and Hughes [21] derived equations for the speed of elastic waves in a stressed solid. The underlying theory is the Murnaghan's theory of finite deformation. The theory is well understood and can be found in various literature such as [21] and [17].

In an infinitesimal deformation, initially isotropic body and a homogeneous triaxial stress field, Kelly [21] derived the following wave velocity equations:

$$\rho_0 V_1^2 = \lambda + 2\mu + (2l + \lambda)\theta + (4m + 4\lambda + 10\mu)\alpha_1 \tag{3.45}$$

$$\rho_0 V_2^2 = \mu + (\lambda + m)\theta + 4\mu\alpha_1 + 2\mu\alpha_2 - \frac{1}{2}n\alpha_3 \tag{3.46}$$

$$\rho_0 V_3^2 = \mu + (\lambda + m)\theta + 4\mu\alpha_1 + 2\mu\alpha_2 - \frac{1}{2}n\alpha_3 \tag{3.47}$$

where ρ_0 is the density at initial state, V_i^2 the wave velocity in 1-, 2- and 3-direction, λ and μ are the Lamé constants, l,m and n are the Murnaghan's constants, α_1, α_2 and α_3 are the strains in Lagrangian coordinates (deformed state) and θ is defined as $\theta = \alpha_1 + \alpha_2 + \alpha_3$. Using the definition of the bulk modulus of Eq. 3.21, the velocities yields

$$\rho_0 V_{1x}^2 = \lambda + 2\mu - \frac{\sigma}{3K_0}[2l + \lambda + \frac{\lambda + \mu}{\mu}(4m + 4\lambda + 10\mu)] \tag{3.48}$$

$$\rho_0 V_{2x}^2 = \mu - \frac{\sigma}{3K_0}[m + \frac{\lambda n}{4\mu} + 4\lambda + 4\mu] \tag{3.49}$$

$$\rho_0 V_{1y}^2 = \lambda + 2\mu - \frac{\sigma}{3K_0}[2l - \frac{2\lambda}{\mu}(m + \lambda + 2\mu)] \tag{3.50}$$

$$\rho_0 V_{2y}^2 = \mu - \frac{\sigma}{3K_0}[m + \frac{\lambda n}{4\mu} + \lambda + 2\mu] \tag{3.51}$$

$$\rho_0 V_{2x}^2 = \mu - \frac{\sigma}{3K_0}[m - \frac{\lambda + \mu}{2\mu}n - 2\lambda] \tag{3.52}$$

where σ is an axial compressive stress in the direction of the second subscripts of V, that is x,y and z. Measurements of any 3 of these velocities allow the computation of l,m and n. Using the above wave velocity equations and the definition of the nonlinear parameter β written as a combination of Lamé and Murnaghan's constants as

$$\beta = \frac{3}{2} + \frac{l + 2m}{\lambda + 2\mu}, \tag{3.53}$$

one can also derive β in terms of wave velocity, Young's Modulus and stress and is given as [27]

$$\beta_{ij} = -\frac{E}{V_{ij}^0}\frac{\partial V_{ij}}{\partial \sigma} \tag{3.54}$$

where the subscript i stands for the direction of propagation and subscript j holds for particle motion in j-direction. Rewritting Eq. 3.54 yields

$$\frac{\beta_{ij}}{E} = -\frac{1}{V_{ij}^0}\frac{\partial V_{ij}}{\partial \sigma} \tag{3.55}$$

where the term $-\frac{1}{V_{ij}^0}\frac{\partial V_{ij}}{\partial \sigma}$ represents the slope in the $\frac{dV}{V}$-σ-relationship. In this research, the slope is defined as

$$\Phi = \frac{1}{V_{ij}^0}\frac{\partial V_{ij}}{\partial \sigma} = -\frac{\beta_{ij}}{E}. \tag{3.56}$$

One can see that the slope Φ depends on the nonlinear parameter β defined in Eq. 2.1 and the Young's Modulus. Therefore, the slope Φ is a measure of nonlinearity. In this research, relative velocity change and stress relations are of interest, allowing a characterization of nonlinearity of the considered medium.

3.4 Pulse Compression

An impulse response refers to the reaction of any dynamic system in response to an external excitation applied infinitesimally short, which is called the Dirac delta function $\delta(t)$. Specifically, in the field of signal processing the impulse response of a solid medium is its output when a brief input signal is applied. The impulse response

describes the reaction of the system as a function of time, and can also depend on other parameters such as spatial position of excitation and recording.

Classically, in the field of nondestructive testing, scientists have used an impulse as excitation signal [6, 15, 38], because an impulse in the time domain shows broadband behavior in the frequency domain: the sharper the pulse in time, the broader the frequency spectrum. The advantage of a broad frequency spectrum is that waves with different wavelengths can detect different sizes of material damage and stages of degradation. Normally, this is done by active means: a signal generated at one point is recorded at another point, and this record is treated as the impulse response. Passive configurations are also possible, but shall not be discussed here. The impulse response, or band-pass filtered Green's function [19], is needed to image a complex medium such as concrete. The image can be used to extract information like wavespeed, diffusivity or dissipation rate. Fig. 6.2 shows a typical impulse response obtained from a concrete.

Another method to obtain the impulse response is the so called pulse compression. Pulse compression is a well known method and mainly used in radar, sonar and echography [44]. The technique uses, similarly as in the classical way of achieving the impulse response, two sensors: source and receiver. The difference lies in the signal which is introduced into the system by the source. The classical short-pulse is replaced by a longer signal, which can be arbitrary in shape and duration. To obtain the impulse response, a post-processing step is necessary, the so called matched filtering.

Pulse compression offers advantages and disadvantages [44] towards the classical method, but since availability of modern technology , costs as well as the digital data processing improvements have strongly impact data acquisition and processing during the past two decades, advantages outweigh disadvantages by far and make pulse compression a good alternative. The disadvantage is the digital post-processing

step of match filtering, which is simply not necessary in the classical way. Advantages are [44]:

1. Increased signal-to-noise ratio (SNR). The SNR is a measure used in science and engineering to quantify how much a signal has been corrupted by noise. It is defined as the ratio of signal power to the noise power corrupting the signal. All real measurements are disturbed by noise. This includes electronic noise, but can also include external events that affect the measured waves such as vibrations, depending on what is measured and of the sensitivity of the device. It is often possible to reduce the noise by controlling the environment. In general, it can be difficult to get a good SNR. The technique of pulse compression increases the SNR and will be shown later. Note that in this research another method is used to further increase the SNR and will be shown later.

2. Maximum versatility. The shape of the waveform is not limited, meanwhile the shape of a pulse is always the same. That allows applying input signals like rectangle form or cosine, frequency modulated signals in the desired frequencies as well as complete frequency spectra, and can be easily adapted to any system.

3. No time limitations. There is no time limitation of the input signal, meanwhile a pulse is a single sharp peak in the duration of the fraction of a second. Normally, the duration is chosen in the order of seconds [27, 44]. The only limitation here is the fact that more instrumentation is required.

4. Higher energy input. Due to the longer duration of the signal, more energy can be introduced into the system. A higher energy leads to a higher energy output and thus a better SNR, and is useful in terms of monitoring small material changes.

Taking all the advantages together, the technique of pulse compression is more sensitive towards proving a concrete and specifically towards detecting changes in the

concrete as the classical method of applying a short pulse into the concrete is able to do, but this does not mean that a pulse is unable for the sake of monitoring changes, as [38] already showed. The changes of the relative velocity change detected in this research are in the order of $5 \cdot 10^{-5}$ $\frac{dV}{V}$, where $\frac{dV}{V}$ means relative velocity change. These small changes make a very sensitive method desirable to be used.

3.4.1 Basic Principle

In order to obtain the impulse response, two waveforms are needed: the input signal and the output signal.

Let us first consider the input signal. Every continuous time signal $s(t)$ can be written in complex notation as [44]

$$s(t) = a(t)e^{i\varphi(t)}, \tag{3.57}$$

where $a(t)$ is the amplitude depending on the time t, i the imaginary number and $\varphi(t)$ the phase which depends also on time t. The equation can be rewritten as

$$s(t) = a(t) \cdot (cos(\varphi(t)) + isin(\varphi(t))). \tag{3.58}$$

Note that in real time signals only the real part is of interest. It can be seen that for the amplitude or magnitude $a(t)$ holds

$$a(t) = |s(t)| \tag{3.59}$$

and for the phase holds [44]

$$\varphi(t) = arg[s(t)] \tag{3.60}$$

The output signal $r(t)$ is diffuse as a result of multiple scattering and attenuated waves which traveled through the concrete. To obtain the impulse response, the cross-correlation of output signal $r(t)$ and input signal $s(t)$ is computed [44, 27]:

$$h(t) = r(t) * s(t), \tag{3.61}$$

In this context, the cross-correlation operation is also known as matched filter. This operation is defined as

$$h(t) = \int_{t'=-\infty}^{t'=\infty} r(t')s(t-t')\,dt', \tag{3.62}$$

where $h(t)$ is the computated impulse response. In a real measurement, the obtained waveform is not continuous but discrete. To derive discrete formula, the integrals are replaced by summations. That integrals can be rewritten in terms of summations is commonly known and for this purpose, the range of the time t is set as

$$t \in [-\infty, \infty] \tag{3.63}$$

Writing the continuous signals as discrete time signals, Eq. 3.62 yields

$$h(n) = \sum_{k=-\infty}^{k=\infty} r_k s_{n-k}, \tag{3.64}$$

where $h(n)$, r_k and s_{n-k} are discrete time signals written as vectors with n as an index. Since real signals are not infinity in length, the summation range can be set as

$$h(n) = \begin{cases} \sum_{k=0}^{N-n-1} r_{k+n} s_k & \text{for } n \geq 0 \\ h(-n) & \text{for } n < 0 \end{cases} \tag{3.65}$$

where N is the length of vector r and s, and n is the index. The vector $h(n)$ has length $(2 \cdot N - 1)$.

3.4.2 Matched Filtering

The matched filter, also known as North filter [44], is obtained by correlating the input signal with the output signal to detect the presence of the input signal in the output signal [20, 44]. This is equivalent to convolving the output signal with a conjugated time-reversed version of the input signal e.g. cross-correlating the signals. The matched filter is the optimal linear filter for maximizing the SNR in the presence of additive stochastic noise. Pulse compression is an example of matched filtering.

Two-dimensional matched filters are commonly used in image processing to improve SNR for X-ray images.

The input signal s is the matched filter, which maximizes the SNR of the output signal r. The output signal can be written as a combination of the desired signal p and additive Gaussian noise v. The idea behind the filter is of geometrical nature. The filter shall be parallel with the output signal, what leads to increase of the signal output, and shall be orthogonal to noise in order to minimize the noise output.

In the case of getting the impulse response of the filter, the optimal matched filter is the complex conjugate time reversal of the input signal s, what can be achieved in cross-correlating s with the output r. Details as well as different derivations can be found in various literature such as [44, 20].

3.4.3 Pulse compression by linear frequency modulation

In this research, the input waveform $s(t)$ is a linear frequency modulated signal, also called chirp.

In chirp signals, the frequency sweeps linearly, beginning at the start frequency f_0, up to the end frequency f_1. The middle frequency is f_m, the instantaneous frequency $f(t)$, the half bandwidth is called τ and T the duration of the chirp. The situation is shown in Fig. 3.6. The chirp signal can be written by expanding Eq. 3.57:

$$s(t) = \begin{cases} a(t)e^{2i\pi(f_m + \frac{\tau}{T}t - \tau)t} & for\ 0 < t < T \\ 0 & else \end{cases} \tag{3.66}$$

The phase of the chirp signal is the argument of the complex exponential and is

$$\Phi(t) = 2\pi(f_m + \frac{\tau}{T}t - \tau)t, \tag{3.67}$$

which is related to the frequency as

$$f(t) = \frac{1}{2\pi}[\frac{d\Phi}{dt}] = f_m + \frac{2\tau}{T}t - \tau \tag{3.68}$$

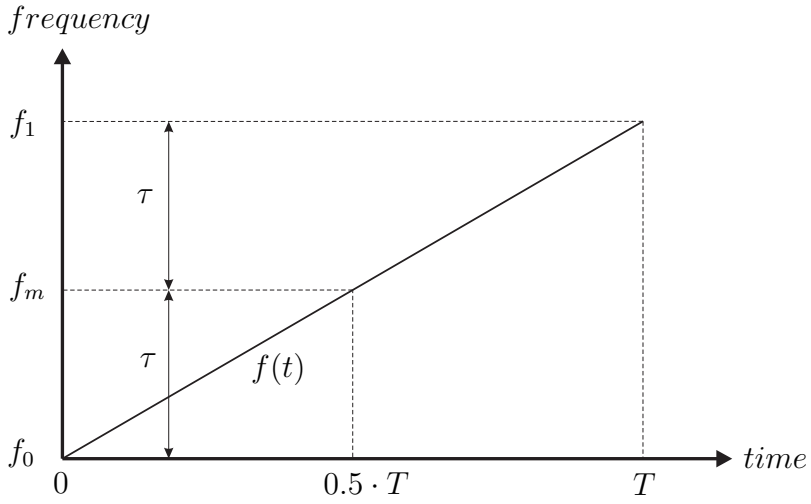

Figure 3.6: Linear up-chirp signal.

Using a linear up-chirp, the cross-correlation operation for pulse compression yields

$$h(t) = \int_{t'=-\infty}^{t'=\infty} r(t')[a(t-t')e^{2i\pi(f_m+\frac{\tau}{T}(t-t')-\tau)(t-t')}]\,dt' \tag{3.69}$$

In Fig. 3.7, a typical response signal $r(t)$ obtained from the receiver is shown. The source signal $s(t)$ was a linear up-chirp signal with $T = 2\,s$, $f_0 = 200\,kHz$ and $f_1 = 800\,kHz$. Cross-correlation of $s(t)$ and $r(t)$ according to Eq. 3.65 yields the impulse response $h(t)$ and is shown in Fig. 3.8. Note that $h(t)$ has length $(2 \cdot N - 1)$ as already described in Sec. 3.4.1. The impulse response of $h(t)$ can be found be extracting the range $[N; N + 2000]$, where N refers to 0 sec. and $(N + 2000)$ refers to 1 msec and is shown in Fig. 3.8.

3.4.4 Energy input and SNR

According to [44], the signal energy introduced into a system can be expressed as

$$E_s = \int_{t=-\infty}^{t=\infty} |s(t)|^2\,dt, \tag{3.70}$$

where E_s is the energy of the signal. Obviously, the longer the time t, the more energy is transmitted.

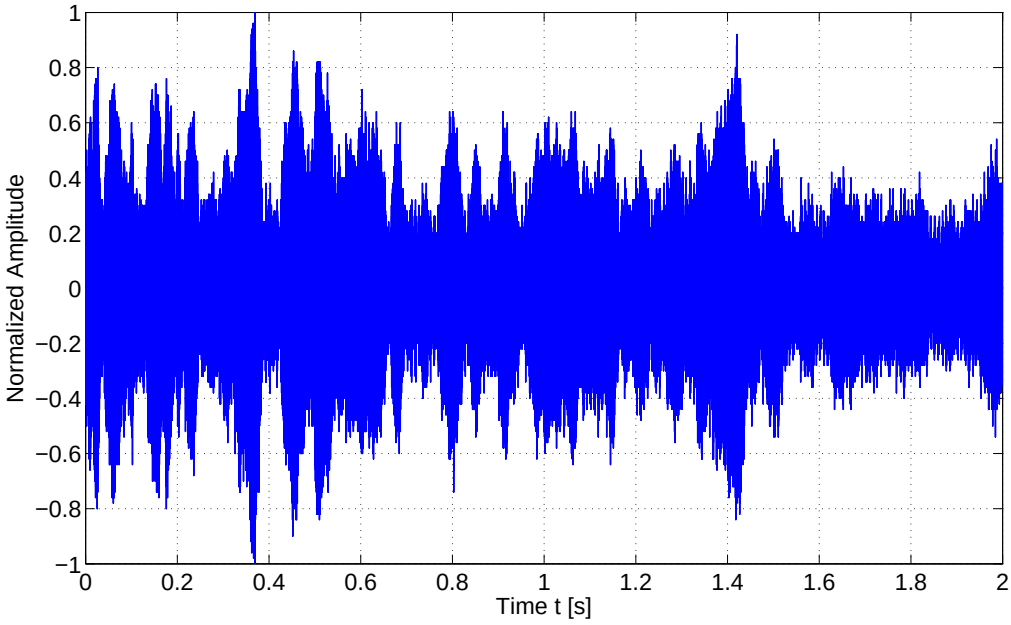

Figure 3.7: Typical Response Signal.

An input signal-to-noise ratio [44] can be defined as

$$\Psi_{in} = \frac{\text{squared signal amplitude } a^2(t)}{\text{average input noise power}}, \tag{3.71}$$

and in the same way the output signal-to-noise ratio:

$$\Psi_{out} = \frac{\text{squared correlation peak } |h(0)|^2}{\text{average output noise power}}. \tag{3.72}$$

where $h(0)$ is the impulse response at time $t = 0$. The SNR gain can be expressed as [5]

$$\Psi_{out} = T\Psi_{in}, \tag{3.73}$$

with T as the total signal duration. Also here it can be seen that the longer the signal is, the higher the SNR gain is.

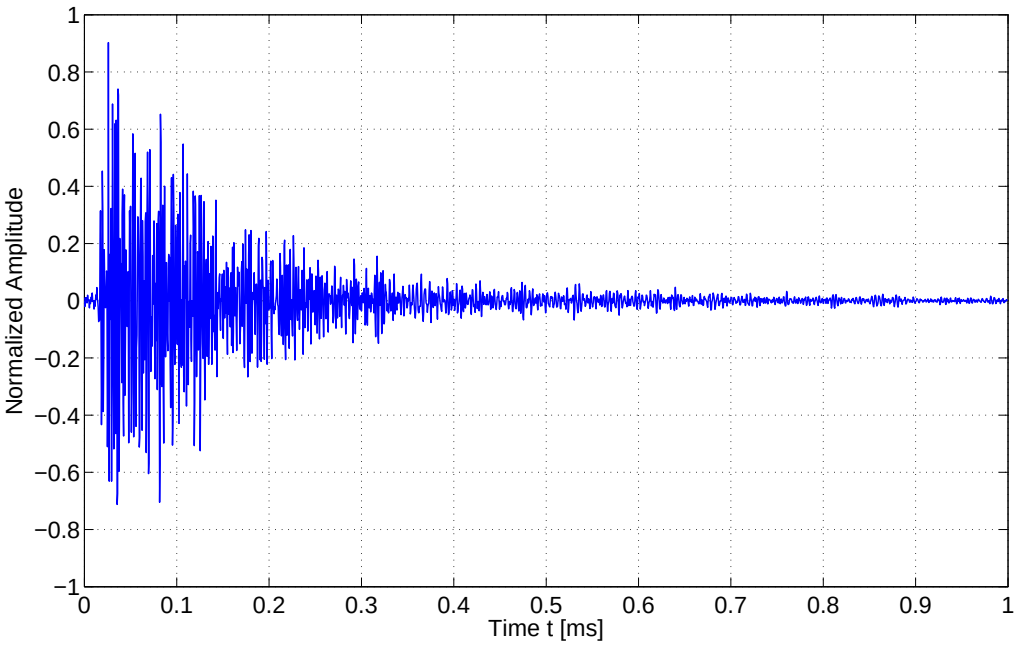

Figure 3.8: Pulse Compressed Response Signal: A typical Impulse Response.

CHAPTER IV

CODA WAVE INTERFEROMETRY

This chapter introduces the technique of Coda Wave Interferometry (CWI). A short introduction will be given followed by the underlying principle of the technique. Next, the mathematical background behind will be presented and the technique's two basic concepts will be compared.

CWI is a technique to compare diffuse fields obtained from fixed source and receiver at two different moments. Stress induced weak velocity variations can be monitored with CWI by comparing two diffuse fields from stressed and unstressed states. There are two different CWI techniques: the doublet technique [39] and the stretching technique (ST) [30, 42]. The doublet technique was first introduced around 20 years ago, whereas ST is a newer technique which was already successfully applied [27]. Both techniques have their advantages and disadvantages and will be discussed in Sec. 4.2.2.

4.1 Stretching Technique

As already mentioned earlier, the used CWI technique in this research is the stretching technique (ST).

4.1.1 Concept of ST

The idea behind ST was developed by [30, 42]. The idea is to stretch (or compress) the axis of a time signal in a way that the signal has much in common with a reference time signal. The time axis gets stretched either by a relative time change

$$t(1+\epsilon) \tag{4.1}$$

or a relative velocity change

$$t(1-\nu), \tag{4.2}$$

where ϵ means relative time change and is defined as

$$\epsilon = \frac{dt}{t} \tag{4.3}$$

with dt as the differential time delay between two time signals, and ν means relative velocity change and is defined as

$$\nu = \frac{dV}{V}, \tag{4.4}$$

with dV as the differential velocity change. The relation between two signals can now be expressed through the relative time change as

$$h_k(t) = h_0[t(1-\epsilon)] \tag{4.5}$$

or through the relative velocity change as

$$h_k(t) = h_0[t(1+\nu)], \tag{4.6}$$

where h_0 represents the reference waveform and h_k means the waveform obtained at the stress level k. Eq. 4.5 and Eq. 4.6 assume that the waveforms are just stretched in time. However, velocity variations will also lead to a weak decorrelation of the waveform, so called distortion [30] which refers to small structural changes of the medium, and can be added to the total change as

$$h_k(t) = h_0[t(1-\epsilon)] + n(t) \tag{4.7}$$

or

$$h_k(t) = h_0[t(1+\nu)] + n(t), \tag{4.8}$$

where $n(t)$ means distortion. For the sake of simplicity of the time stretch, the distortion is ignored:

$$n(t) = 0. \tag{4.9}$$

Considering a spatial distance s, time t and velocity V are related to each other as

$$s = V \cdot t. \tag{4.10}$$

Assuming a small time advance dt in the arrival time with constant distance s leads to small velocity increase dV, which leads to the connection between relative velocity change and relative time change of two waveforms and can be obtained as

$$\frac{dV}{V} = -\frac{dt}{t}. \tag{4.11}$$

Plugging Eq. 4.11 into Eq. 4.5 leads to Eq.4.6. Fig. 4.1 shows the whole situation using arbitrary signals h_0 and h_k. The ν_k of Fig. 4.1 is the ν that fits h_k best to h_0

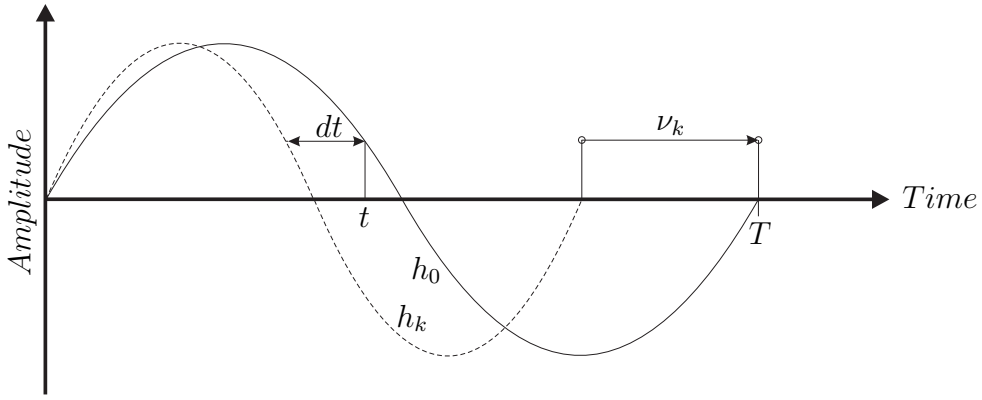

Figure 4.1: Stretching of time axis.

and will be explained in Sec. 4.1.2.

In Fig. 4.3 and 4.4, the same two real waveforms obtained in this research at different stress levels are shown. One can see that the the waveform obtained at a higher stress level (dashed line) arrives first because the waves travel faster (acoustoelastic effect). In Fig. 4.3, the time delay is hardly visible and in Fig. 4.4, which shows a later time section of the same signal, the time delay is clearly visible. Both figures show a time window of $30\mu s$. The subscripts 3.0 and 4.0 represent the stress level the ultrasound measurements were performed: 3.0 MPa and 4.0 MPa.

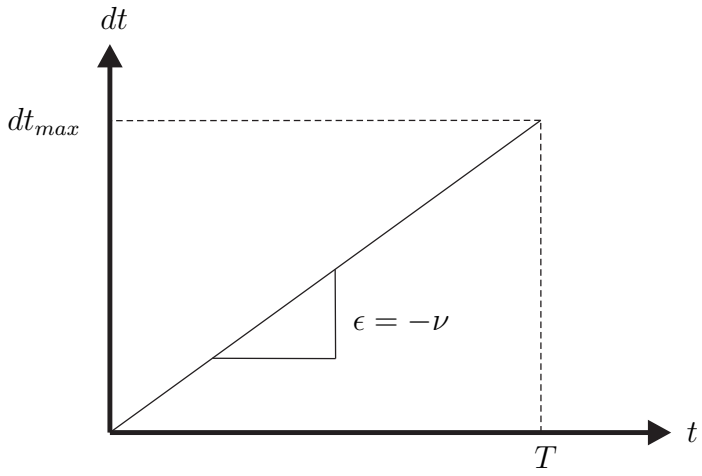

Figure 4.2: Linear time change dt over the whole duration.

According to theory, the time advance (or delay) dt is linear to the time t and related through the constant ν as

$$dt = -\nu \cdot t, \tag{4.12}$$

as shown in Fig. 4.2. That leads to the relation of dV and V which is given by

$$dV = \nu \cdot V \tag{4.13}$$

4.1.2 Cross-Correlation Coefficient Function

As already meantioned in Sec. 4.1.1, the time axis is stretched in a way that the stretched signal has much in common with the reference signal, or in other words the signals are best correlated.

For this sake, the cross-correlation provides a good mean. The Eq. 3.61, 3.62 and 3.64 introduced the cross-correlation operation already in Sec. 3.4.1. Adapting Eq. 3.62 with h_k and h_0 and normalizing [8] yields

$$CC_k(t) = \frac{\int_0^T h_k(t'-t)h_0(t')\,dt'}{\sqrt{\int_0^T h_k^2(t'-t)\,dt' \int_0^T h_0^2(t')\,dt'}} \tag{4.14}$$

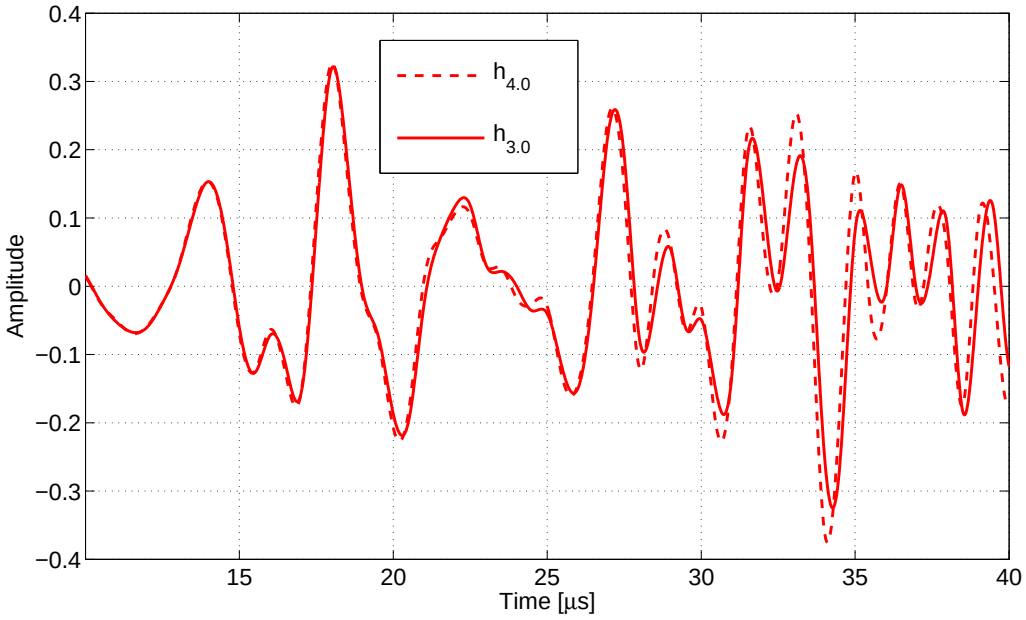

Figure 4.3: Early Time Interval of two real waveforms at different stress level: 3.0 MPa and 4.0 MPa.

where $CC_k(t)$ is the cross-correlation coefficient computed with the reference waveform h_0 and h_k, which was obtained at stress level k. The denominator of the fraction normalizes the function [8] so that the range of $CC_k(t)$ is given by

$$-1 \leq CC_k(t) \leq 1. \tag{4.15}$$

A value of $CC_k = 0$ means that the functions h_k and h_0 are totally decorrelated, whereas $CC_k = \pm 1$ refers to totally correlated waveforms. Changing the argument $(t - t')$ with the time-stretch term of Eq. 4.2, $t(1-\nu)$, the cross-correlation coefficient yields

$$CC_k(\nu) = \frac{\int_0^T h_k[t(1-\nu)]h_0(t)\,dt}{\sqrt{\int_0^T h_k^2[t(1-\nu)]\,dt \int_0^T h_0^2(t)\,dt}}. \tag{4.16}$$

The relative velocity change obtained from Eq. 4.16 for further processing is called ν_k for which the maximum of the cross-correlation coefficient is obtained. The adequate

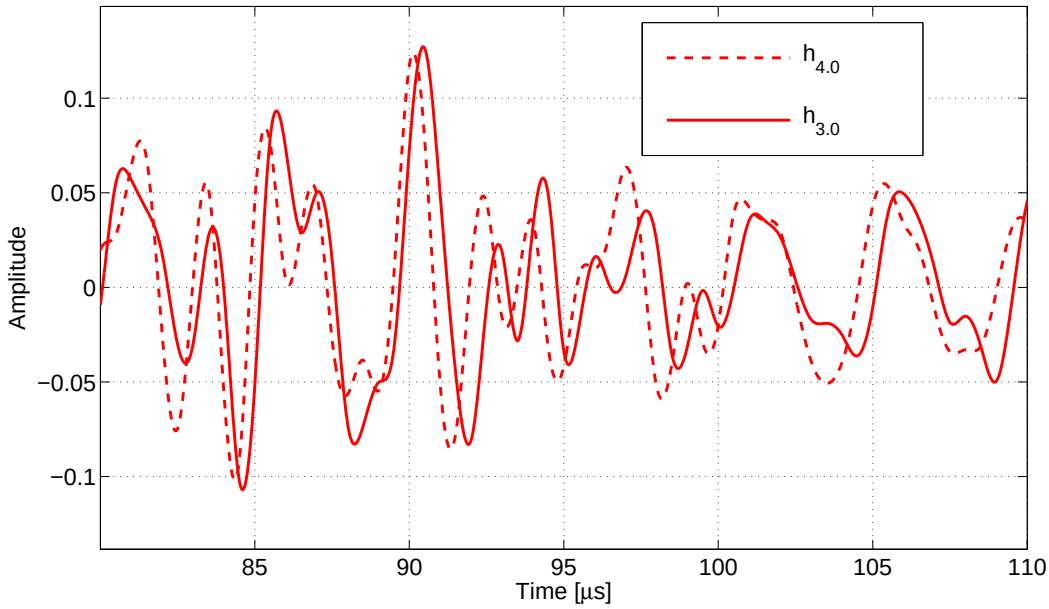

Figure 4.4: Later Time Interval of two real waveforms at different stress level: 3.0 MPa and 4.0 MPa.

mathematical condition is given by

$$\nu_k = \max_{\nu \in \Gamma} CC_k(\nu), \tag{4.17}$$

where Γ is the domain of definition of ν.

4.1.3 Theoretical Approach

If we assume h_k and h_0 to be continuous functions, a theoretical estimate of the cross-correlation coefficient can be written [27] as

$$CC_k(\nu) = A \cdot \frac{\int_{\Delta f} \rho(f) sinc(2\pi f(\nu - \nu_k)T)\, df}{\sqrt{\int_{\Delta f} \rho(f)\, df}} + B(\nu), \tag{4.18}$$

where f is the frequency, Δf is the bandwidth of frequency, $\rho(f)$ the spectral density. The letter A represents a constant which is given by

$$A = \frac{\langle h^2 \rangle}{\langle h^2 \rangle + \langle n^2 \rangle} \tag{4.19}$$

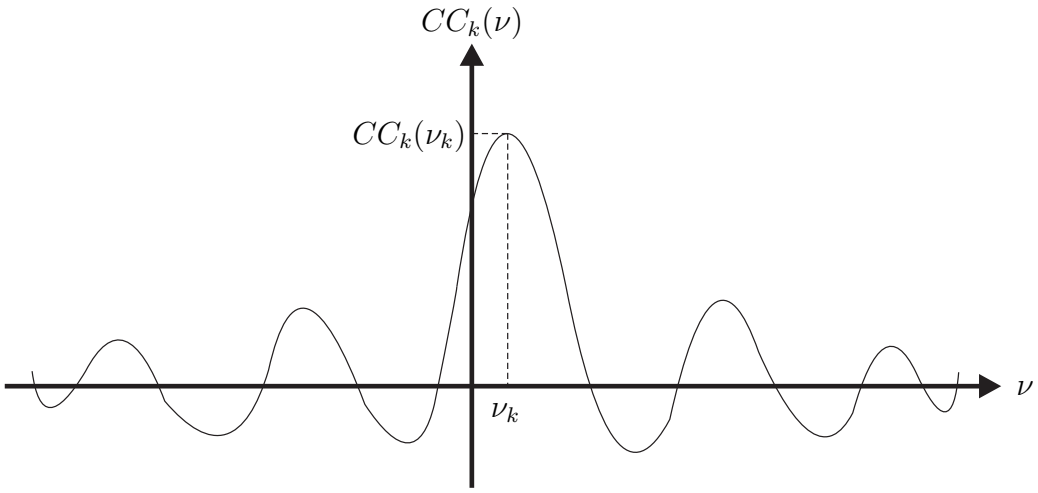

Figure 4.5: Typical $CC_k(\nu)$-curve with maximum at ν_k.

with $\langle h^2 \rangle$ as the variance of h and $\langle n^2 \rangle$ as the variance of additional fluctuations [27] n. $B(\nu)$ represents a random process of zero mean and standard deviation:

$$\sqrt{\langle B^2 \rangle} = \frac{1}{\sqrt{T\Delta f}} \frac{\langle n^2 \rangle + 2\sqrt{\langle h^2 \rangle \langle n^2 \rangle}}{\langle h^2 \rangle + \langle n^2 \rangle}. \tag{4.20}$$

If $A \gg \sqrt{\langle B^2 \rangle}$, the maximum of $CC_k(\nu)$ is found [27] and $\nu = \nu_k$. If the noise or fluctuations $n(t)$ are strong, an increase of the integration time T or the frequency bandwidth Δf can be used to counteract as it can be seen in Eq. 4.18. Furthermore, it can be seen in Eq. 4.18 that $CC_k(\nu)$ looks similar to a sinc-function which has its maximum at v_k, what is shown in Fig. 4.5.

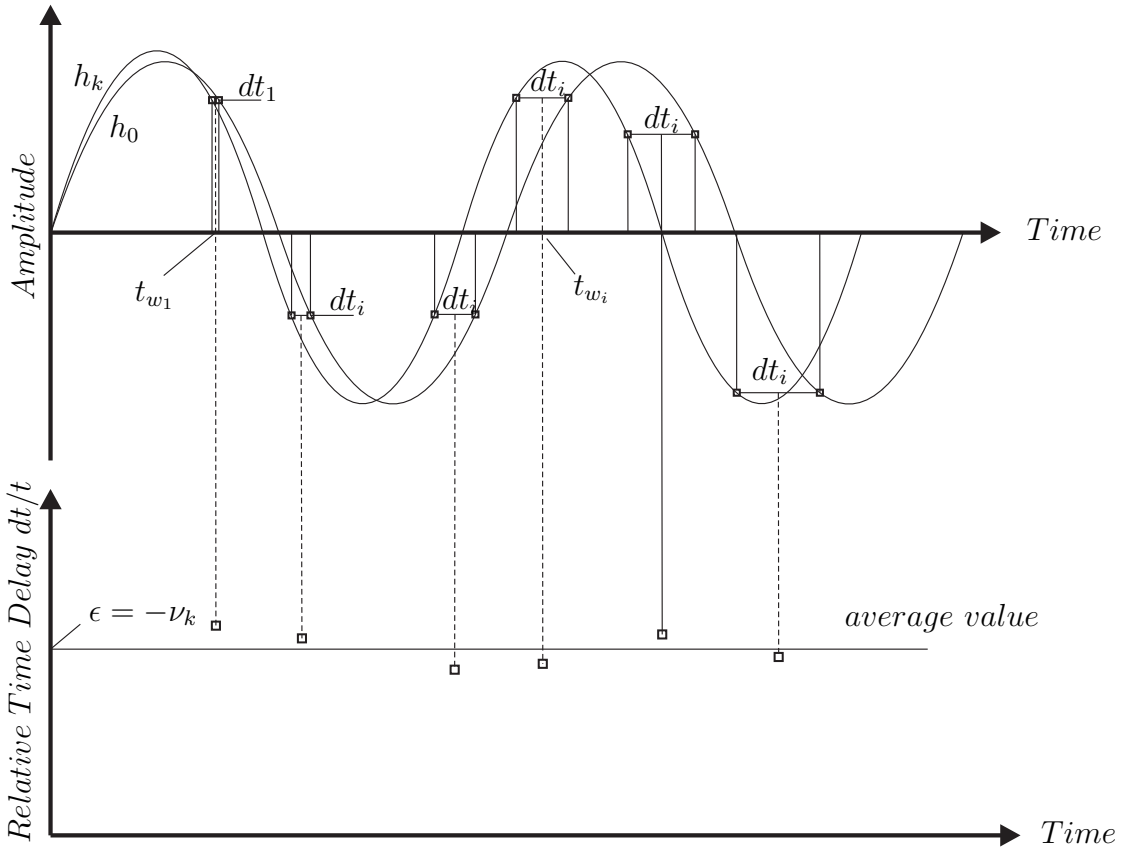

Figure 4.6: Doublet technique.

4.2 ST vs. Doublet Technique

4.2.1 Doublet Technique

To obtain the relative velocity change using the doublet technique, the time delay dt of a time window centered at time t_w is calculated [39]. The relative velocity change can be calculated as $\nu = -\epsilon = -\frac{dt}{t_w}$. To get a more precise value of ν, several time windows are used and each relative time change $\epsilon_i = \frac{dt_i}{t_{w_i}}$ is determined. Plotting all time delays over t and determine the axis intercept (horizontal line) results in a more stable value of ν_k. The situation is shown in Fig. 4.6. Nonoverlapping time windows with a total of 10 waveform cycles were used to calculate ν_k in [38] as well the requirement $t \gg t_w$.

4.2.2 ST vs. Doublet Technique

Both techniques have their advantages and disadvantages and can be summarized as follows.

1. Using ST according to Eq. 4.16, the integration can be done over the whole record in order to obtain a more stable and precise result of the relative velocity change. Furthermore, the integration borders can be easily adapted to the record. The doublet technique uses small time windows for calculating the relative velocity change. These time windows are nonoverlapping and cover only a small portion of the whole record resulting in a less accurate value [27] for ν. To get a good estimate of ν, many time windows are needed [38]. Also, to satisfy the assumption $t \gg t_w$, one cannot use the whole length of the time signal for calculation.

2. The ST is based on the stretching of the time axis. This approach implies that the whole considered integration area is stretched linearly, shown in Fig. 4.2, what is in accordance with the theory. The doublet technique approach calculates the time shift dt in several windows. This approach implies that the time shift is constant within each considered window, what is normally not the case [27] since time delay linearly changes with time.

3. Normally, ST requires a longer computational time than the doublet technique, since integration can be done over the whole signal For the doublet technique, the calculations are limited to numbers in the order of 10 data points [38]. Note that the range of t, the range of ν and the step size of ν is user selected in ST what may lead to big differences in computational time. In addition ST requires interpolation after stretching the signal in order to calculate the correlation function.

CHAPTER V

EXPERIMENTAL PROCEDURE

For the determination of relative velocity change in cement-based materials using diffuse ultrasound, it is crucial to have a reliable and repeatable measurement technique. This chapter describes the instrumentation used in this research. Also, the experimental procedures used for the different experiments are described.

5.1 Instrumentation

5.1.1 Signal Generation

An arbitrary function generator, Agilent 33250A, provides the source signal for the diffuse measurements. The voltage of the function generator can vary within a maximum range of 10 Volt peak-to-peak which refers to an amplitude range in ±5 Volt. The function generator can generate functions of the following shapes: sine, square, ramp, pulse, noise, and arbitrary. Those signals can be additionally modulated by either a sweep function or a burst function. The sweep function provides the opportunity to enter either the start frequency f_0 and the end frequency f_1, or the middle frequency f_m and the half bandwidth τ, also called span. Note that these frequencies are defined in Sec. 3.4.3. Both opportunities fully describe the frequency range. The upper frequency limitation is given by 80 MHz, which is the maximum frequency the function generator can provide. The user can choose between an up-sweep and an down-sweep. The up-sweep signal starts at lower frequency and ends up at a higher frequency, the down sweep performs vice-versa. Furthermore, the sweep can be chosen to be linear or logarithmic in time. For post-processing help, a marker can be set as soon as a prescribed frequency is reached, resulting in a sharp peak at that frequency. The total duration of the signal can be set up to 500 seconds. The signal

Figure 5.1: Function Generator Agilent 33250A.

is chosen to be a sine signal with an overlaying linear up-sweep. The frequency range of the sweep is chosen to be 200 kHz to 800 kHz in the study. The up-sweep is chosen to profit from the characteristics described in Chap. 3.4. Also, the used frequency range enables detection of damage and changes in the material of different sizes. The voltage is chosen to be the maximum available: 10 Volt peak-to-peak in order to have a high energy input. A high voltage is needed due to the high attenuation in cement-based materials as described in Sec. 3.2. The signal duration is chosen to be 2 seconds, what will be explained in Sec. 5.1.4.

A useful tool provided by the function generator is the trigger operation. The function generator can be triggered internally or by an external source, or manually using either a positive or a negative edge. In this research, the function generator is triggered manually with a positive edge by pushing the Trigger-button. The Sync-output channel provides the trigger signal to synchronise the oscilloscope.

5.1.2 Signal Amplification

As already discussed in Sec. 5.1.1, a high input signal and an amplified received signal are essentially needed to get a good signal-to-noise ratio from the concrete specimens used in this research.

For amplification, the instrument Panametrics 5058PR is used. It is not only

an amplifier, but can also be used for pulse generation, or both at the same time. However, in this research it is only used as amplifier. The output signal received from the receiving transducer is being amplified. The signal can be amplified by either 40 dB or 60 dB. In this research, the maximum of 60 dB is chosen. The device also offers the functions to attenuate and to filter the signal. Since attenuation is in total contradiction to the purpose of using this device, the attenuation is set to 0 dB. There is also no need to filter the signal, since the post-processing step matched filtering filters out the frequency range as described in 5.1.1 and as shown in Fig. 6.2 in Sec. 6.2. Accordingly, the high-pass filter and the low-pass filter are turned off. Furthermore, the phase can be inverted by 180°. However, there is no need to invert the phase and has no advantage. The disadvantage of the device is

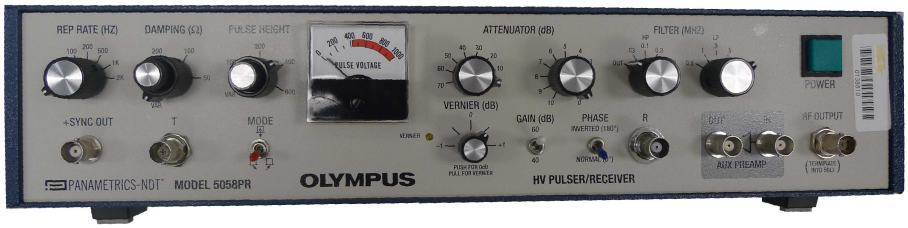

Figure 5.2: Panametrics 5058PR.

the combination of pulse generation at one side and amplification/attenuation at the other side, which leads to cross-talk between them. Cross-talk is an artificial signal, because it is only due to the imperfect electrical isolation in the amplifier and it causes distortion of the amplified received signal by the pulse. Therefore, the pulse on the pulse generation side is turned off, because, the pulse will be seen in the received signal after amplification.

5.1.3 Source/receiver transducer

Both transducers, the source and the receiver, are Panametrics V103 1 MHz broadband transducers with a diameter of 12.5 mm. The calibration sheet of the manufacturer states that the center frequency is around 1 MHz, but the transducers are also capable of detecting much lower and higher frequencies.

The two transducers are coupled to the specimen with a viscous couplant: high vacuum grease from the Dow Corning Corporation.

A simple fixture is designed and manufactured for the source transducer which holds a small spring with a diameter of 11 mm. The spring presses the transducer with a constant force to the surface of the sample. The fixture is clamped to the sample, too.

The manufacturer also provides information for the optimal temperature range of operation. The temperature does not affect the transducers behavior up to 40° C. This is a crucial advantage for the use of the transducers, because the techniques of pulse compression and ST are very sensitive and a temperature change will affect the measurements [30]. Without the consistency of the transducers, relationships and curves have to be found for compensation of the temperature effect. The consistency of the transducers within the above mentioned temperature range was also found in a preliminary test, but shall not be discussed here.

Another effect which has to be considered is phase cancellation. In the strong scattering regime, the diffuse portion of the signal is temporarily and spatially incoherent with the incident signal. Due to fast spatial and temporal fluctuations of the phase and amplitude, the whole diffuse field will converge to zero by averaging over random configurations or averaged in a finite volume. This effect is called phase cancellation [35]. Furthermore, phase cancellation is implicitly done by transducers with finite surface areas [12]; this requires a transducer with a small surface area necessary if the diffuse field is of interest. To get a small surface area, a small cone

Figure 5.3: Receiving transducer with cone

is designed and manufactured. The bottom diameter of the cone is 5 mm, the top diameter is 2 mm and the cone's thickness is 2.2 mm. The cone is made out of aluminum. The cone is attached to the receiving transducer with superglue RP 100 from Instantca. Note that the cone was not detached and reattached again from the transducer. Due to the attached cone on the transducer surface, it was not possible to keep the transducer perfectly perpendicular to the specimen's surface resulting in inconsistent coupling conditions, because the transducer by itself is just unstable. To overcome these inconsistent coupling conditions, a fixture is designed and manufactured to keep the transducer with a cone in a stable and perpendicular position during the tests. With this fixture it is also possible to press the transducer with a constant pressure on the sample's surface. An alternative to the transducer with cone would be a pin-transducer by Valpey-Fisher with a diameter of 1 mm. However, there are

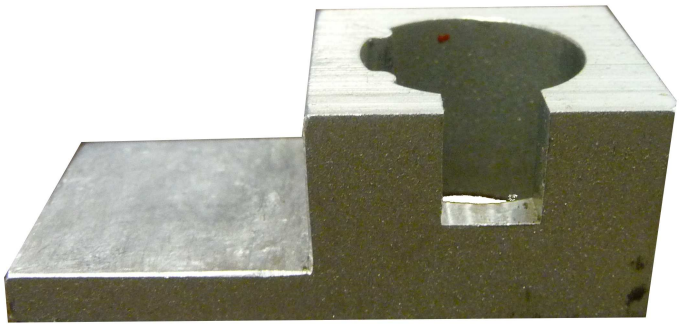

Figure 5.4: Fixture for receiving transducer

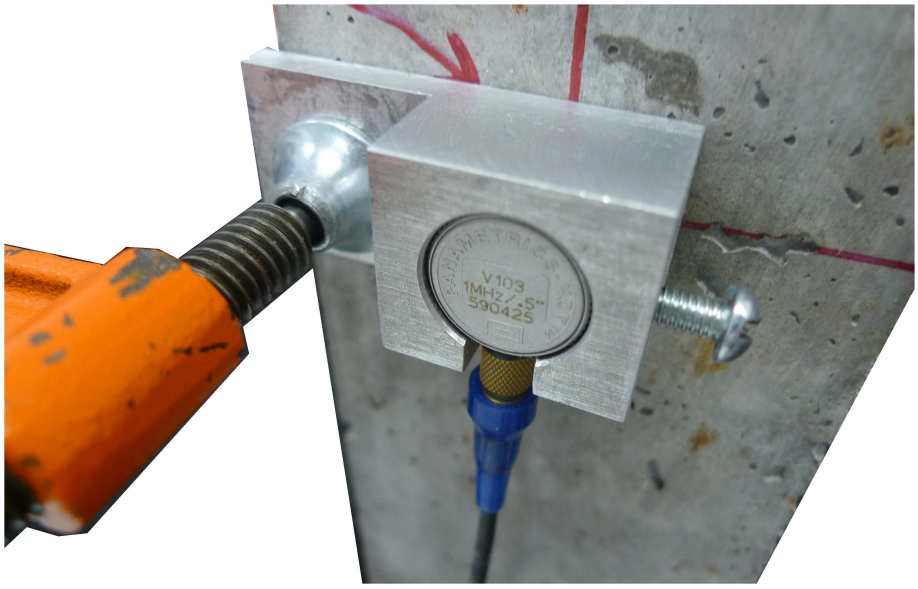

Figure 5.5: Clamp used to hold Fixture with Receiving Transducer.

several problems with these pin-transducers. It is difficult to get consistent coupling conditions, to hold them perpendicular to the surface and to fix them with constant pressure to the sample. Furthermore, they have only narrow-band efficiency [7] and are sensitive to the environment such as electromagnetic fields. For these reasons, pin-transducers are not used in this research.

Furthermore, the cone enables a better point-wise detection, because the receiving surface is much smaller. This helps to reduce coupling effects on the receiver side.

5.1.4 Waveform Acquisition

A digital phosphor oscilloscope, Tektronix TDS5034B, is used for the acquisition of the waveform in this research. The oscilloscope has four acquisition channels and provides a maximum sampling frequency of 5 GSamples per second. Channel 1 was used for acquiring the response signal from the receiving transducer, $r(t)$ as defined in Sec. 3.4.1, and Channel 2 was used for acquiring the input signal $s(t)$ from the function generator, also defined by Eq. 3.61, 3.62 and 3.64 in Sec. 3.4.1. The oscilloscope also provides a trigger function or can be triggered externally. During

Figure 5.6: Spring holds Source Transducer.

the tests, the oscilloscope is triggered externally by the function generator described in Sec. 5.1.1. Once triggered, the function generator provides the source signal and the oscilloscope captures the source and the receiver signal. The oscilloscope is triggered using a cable as direct connection from the Sync-output channel of the signal generator to channel 3 of the oscilloscope. The trigger level in the oscilloscope is set to 100 mV, high enough so that noise will not lead to trigger operation, and low enough so that only the trigger signal of the function generator triggers the oscilloscope. Also, the trigger operation is realized with a positive edge, which is in accordance to the function generator. The oscilloscope runs on Windows 2000 as an operating system and allows saving the files in different formats. Each saved waveform consists of two files: the main file, which contains the values of the waveforms in $*$.dat format, and an auxiliary file, which contains information like the time increment dt between two samples or the total number of data points taken in the measurement. This file is saved in $*$.hdr format. Both files are readable by Matlab and are basically written as column vectors. The waveforms are transferred via usb-connection to a flash drive

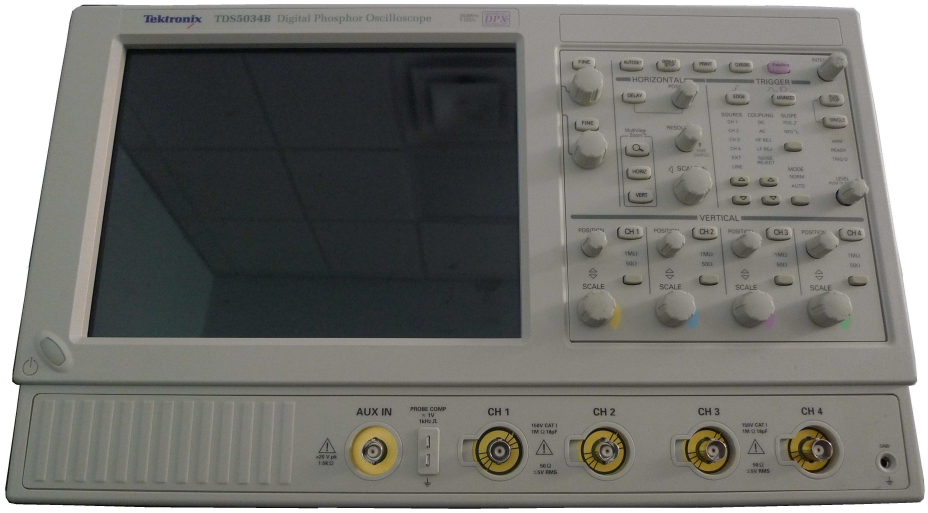

Figure 5.7: Tektronix TDS5034B.

and then to PC.

5.1.4.1 Signal to Noise Ratio

As already defined in Chap. 3.4, the signal-to-noise ratio (SNR) is a measure used in science and engineering to quantify how much the signal has been corrupted by noise.

The method of pulse compression increases the SNR as shown in Chap. 3.4. Furthermore, the signal provided by the function generator is set to its maximum, an amplitude of ±5 Volt, and the received signal from the transducer is amplified. Both methods take essentially part towards the goal of achieving a good SNR.

Another method to increase the SNR is signal averaging. Averaging over several waveforms reduces the noise level by decibel in the order of 20 dB to 30 dB, depending on the number of averaged measurements [14]. According to [7], the reduction of noise level can be shown as follows. Consider a single measurement $X_i = s_i + N_i$, where s_i is the signal and N_i represents noise. Assuming $E[N_i] = 0$ and $E[N_i^2] = \sigma_N$, the mean and variance of X_i is given by:

$$m_{X_i} = E[X_i] = s_i + E[N_i] = s_i \tag{5.1}$$

$$\sigma_{X_i}^2 = E[(X_i - m_{X_i})^2] \tag{5.2}$$

assuming unbiased measurements $E[s_i] = s_i$. The averaged value over N measurements is given by $X = \frac{1}{N}\sum_{i=1}^{N} X_i$. Under the assumption of uncorrelated noise of the N different X_i, one can simply add the variances and calculate the variance of the averaged signal. One obtains

$$\sigma_X^2 = \frac{1}{N^2} E[\sum_{i=1}^{N} (X_i - m_{X_i})^2] = \frac{\sigma_N^2}{N} \tag{5.3}$$

As it can be seen, averaging over N signals decreases the variance by factor N and the standard deviation by $\sqrt{N}$. However, averaging is not done in this research since environmental conditions, such as temperature change, have too much influence on the impulse response obtained through pulse compression and consequently on the relative velocity change.

5.1.4.2 Sampling Rate and Record Length

The sampling rate and the record length are limited and must be chosen in accordance with the function generator and the requirement of the Nyquist-Shannon sampling theorem. The requirement states that the sampling frequency must be at least twice as high as the highest frequency to be measured. The signal provided by the function generator has 800 kHz as its highest frequency. Thus, the sampling frequency of the oscilloscope must be higher than 1.6 MSamples/sec. A sampling frequency lower than 1.6 MSamples/sec. would result in frequency aliasing, which means that higher frequencies were detected as lower frequencies. The signal provided by the function generator is not always the same, it is shifted in phase. This phase-shift is due to the generation principle of the function generator. An electric engine starts rotating as soon as the function generator is turned on in its sweep mode, and once the trigger button is pushed for the whole ultrasound experiment to start, the angle of the engine is not always the same but arbitrary, resulting in an arbitrary phase shift from measurement to measurement. Due to that fact, one can not perform signal averaging, and both, the source signal and the receiver signal have to be measured

and saved. If the signal produced in the function generator always start with the same phase, it would not be necessary to measure the source signal since it can be generated in Matlab for post-processing steps. The oscilloscope is able to save 8 Million data points, that are 4 Million for each signal, the source and the receiver signal. In order to get a sufficiently long signal for the benefits described in Chap. 3.4, the sampling frequency has to be decreased. The longer the signal, the lower the sampling frequency since number of sampling points are limited by 8,000,000 points, and vice-versa. A good trade-off is found with a signal length of 2 seconds and a sampling frequency of 2 MSamples/sec, which is higher than the Nyquist frequency of 1.6 MSamples/sec. The signal duration of 2 sec. is around 2000 times longer than an impulse response, so that a sufficiently long signal is acquired.

5.1.5 Test Frame

The test frame used in this research to apply a load on the concrete specimen is Satec 22EMF. This test frame allows performing tensile tests and compression tests. For compression tests, the top and the bottom grips of the test frame are assembled with round plates. The plates are flat and perfectly parallel to each other. The bottom plate is fixed to the frame and the upper plate is movable in vertical direction. Furthermore, the mounting suspension of the upper plate is realized with a Cardan joint allowing an additional circular motion of the top plate. To move the upper plate down before the test, a manual field controller can be used for a preliminary approach of the top plate to the top surface of the concrete specimen, which is useful to get a quick soft-start. The term soft-start refers to a slow approach level to the concrete's surface up to a load of 200 Newton, but can also be user selected. As tests are performed, the top plate moves down very slowly to get a soft contact with the top surface of the concrete sample and then continue to slowly apply load in a pre-determined range. This soft-start step protects machine and specimen from being

damaged or destroyed by a too high approach rate e.g. too fast moving of the top plate. The machine is able to apply a maximum force of 100 kN, and in between this range the machine has an accuracy of 5 N. The test frame's control variable can be either load or distance e.g. stress or strain. In this research, the machine is driven by load in order to fulfill the purpose of Eq. 3.54, which is in contrast to the strain-driven test by [38]. The test frame is mainly controlled by a control station.

Figure 5.8: Test Frame.

The control station consists of a computer with the control software PARTNER. The whole station is connected to the test frame via GPIB-interface. Also, some sensors like strain gauges are connected to the control station. Unfortunately, the strain gauges are too small for the 7.62 cm long side of the concrete specimen, which does not allow to measure strain with the strain gauges. The comprehensive software allows entering control variables such as soft-start approach rate in force per time, approach rate once soft-start is done, maximum load level or alternatively stress level and duration at the maximum applied load.

The software does not allow programing a time-load protocol according to the load steps required in this research. Instead, the load step protocol can be performed manually by the user. The user simply starts the next load-level manually, for example

to increase the stress in the concrete from 3.2 MPa to 3.3 MPa. While doing so, the information of vertical position of the top plate displacement gets lost, which could be also acquired by the control station if the machine were controlled automatically. As a result, the strain can not be calculated using $\epsilon = -\frac{\Delta L}{L_0}$, where ΔL is the displacement of the top plate once soft-start occurred and L_0 is the original length of the specimen. Consequently, the Young's Modulus can not be determined in this manual control mode.

5.1.6 Specimens

In this research, different concrete specimens were cast to perform the different types of experiments.

Two different kinds of specimens were mixed: Low-reactive specimens and high-reactive specimens. Low reactive and high reactive refers to the reactivity in regard to ASR, as described in Sec. 2.2. In the following, the high-reactive specimens are abbreviated as HRSX and the low-reactive specimens as LRSX, whereas X holds for the specimen number. The difference between the two specimen types lies in their mix design, as shown in Tab.5.1. The fine aggregate used for the high-reactive specimens is Spratt and is highly reactive in terms of ASR, and the fine aggregate used for the low-reactive specimen is Adairsville and has only a very low ASR-reactivity. The mix design was chosen on the basis of the American Standard for Testing and Material *ASTM C 1293* [4] and the mixing procedure was on the basis of the method of *The American Concrete Institute (ACI)*. The mix design is shown in Tab. 5.1. The coarse aggregate portion is given as gradation [33]. The gradation requirements are given in Tab. 5.2. To determine the gradation of aggregates, all aggregates pass through a number of sieves. The sieves holds particles larger than the size of the opening, while smaller particles pass the opening. Sieves with openings greater than 0.25 in. are marked by the size of the opening, while sieves with openings smaller than 0.25

Figure 5.9: Cross Section of Low-Reactive Specimen LRS4.

in. are labeled by the number of uniform openings per linear inch [4]. The gradation of coarse aggregate is shown in Tab. 5.2. No gradation is done for the fine aggregate. The fine aggregate is used as delivered without any gradation.

Ultrasonic waves traveling through the specimens in this research are assumed to be diffuse. In order to justify this assumption, two aspects can be considered: the reflection and transmission coefficients as given by Eq. 3.32 and 3.33 as basis and the Diffusivity parameter as explained in Sec. 6.2 and given by Eq. 6.1. The material properties given in Tab. 5.3 are used to calculate reflection and transmission coefficients in Sec. 5.1.6.3.

5.1.6.1 Curing

Curing of concrete refers to the strength of concrete through cement hydration [34]. Several conditions effect the curing process: time, temperature and humidity. The time-strength relations assume a moist environment (moist-curing): the longer the curing period, the higher is the strength [34]. Fig. 5.10 shows a typical curing curve for concrete. Similarly, it can be said for humidity that moist-cured concrete has higher

Table 5.1: Mix Design of Concrete Specimen

Component	low reactive specimen	high reactive specimen
Cement (kg)	0.8419	0.8419
Water (kg)	0.3789	0.3789
Coarse Aggregate (kg)	2.2113	2.2113
Fine Aggregate		
high reactive Spratt (kg)	-	1.3216
low reactive Adairsville (kg)	1.3216	-
Water-cement ratio		
by weight	0.45	0.45
by volume	1.0002	1.0002
Sample size (cm)	30.48 x 7.62 x 7.62	30.48 x 7.62 x 7.62

Table 5.2: Gradation of Coarse Aggregate

Sieve Size		Retained Mass Fraction/Total Weight (%)
Passing	Retained	
19 mm	12.5 mm	33.3
12.5 mm	9.5 mm	33.3
9.5 mm	4.5 mm	33.3

Table 5.3: Acoustic properties

Material	c_L (m/s)	c_T (m/s)	E (GPa)	ν	ρ (kg/m^3)	Z (kg/sm^2)
Cement paste	3550	2000	20.0	0.26	1950	6922500
Sand	5570	3540	75.4	0.16	2600	14482000
Limestone	5200	2830	55.8	0.29	2700	14040000

strength than air-cured concrete. For the temperature influence, it can be generally said that the higher the temperature the faster the hydration of the Portland cement and the higher the strength of the concrete. The most gain in strength through curing occurs in the first 20 to 30 days. In order to compare results within each experiment, one has to consider the effect of curing e.g. the curing time of specimens used for comparison should be the same.

5.1.6.2 Specimen Preparation

The specimen are prepared before compression tests in order to overcome imperfect boundary conditions at the interfaces between the contact of the top and bottom

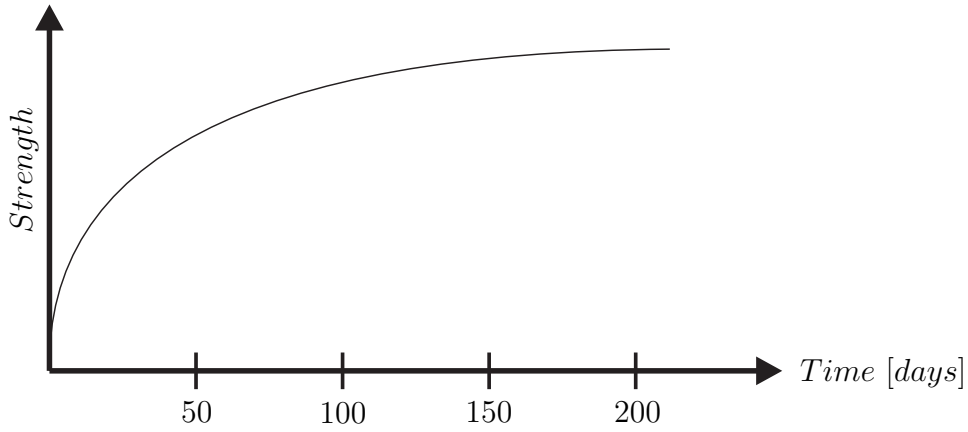

Figure 5.10: Typical time-dependent curing curve of concrete.

surfaces of the specimen and the plates of the test frame. The top and bottom surfaces of the specimens are rough and uneven after removing them from the mold. Thus, the specimen's longitudinal axis is not perpendicular to the surface of the top and bottom plate resulting in shear stress when compressed. The situation is depicted in Fig. 5.11. Therefore, the top and bottom surfaces are grounded to get a flat plane perpendicular to the specimen axis resulting in uniaxial vertical stress. Note that Eq. 3.54 is only valid for uniaxial stress.

Furthermore, the position of the receiving and source transducer is marked on the specimens. One transducer is attached in the middle of a side face, the other transducer is attached also in the middle of a neighboring face as shown in Fig. 5.12. The two neighboring faces used are chosen based on surface quality e.g. smoothness. During the ASR- and Thermal-tests the transducers are removed in order not to damage the transducers during heating and are reattached at the same position again. Note that it is not possible to reattach them at exactly the same position, which results in a measurement error and will be discussed later.

5.1.6.3 Reflection and Transmission

As already mentioned in Sec. 3.1.4, reflection and transmission coefficients can be calculated using the impedances $Z^i = \rho^i c^i$ of two neighboring media. Since it is assumed

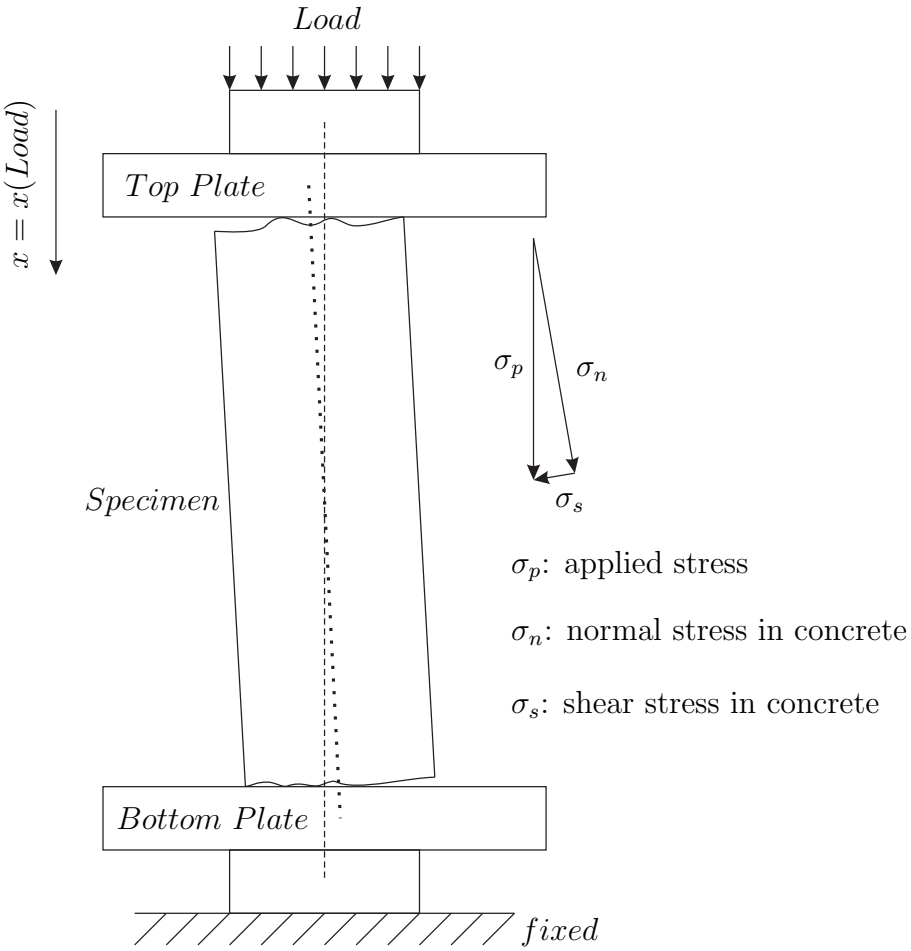

Figure 5.11: Imperfect Boundary Conditions.

that there is no contact between aggregates, these coefficients of the sand/aggregate combination are not necessary. Note also that the coarse aggregates Spratt-Limestone and Adairsville-Limestone do have slightly different acoustic properties as those of properties of limestone shown in Tab. 5.3, but are close enough for a first rough estimation of reflection and transmission coefficients [14]. Using Eq. 3.32, Eq. 3.33 and the values of Tab. 5.3, one obtains

$$T_{paste/gravel} = 1.3395 \tag{5.4}$$

$$R_{paste/gravel} = 0.3395 \tag{5.5}$$

$$T_{paste/sand} = 1.3532 \tag{5.6}$$

$$R_{paste/stone} = 0.3532 \tag{5.7}$$

These values show that ultrasound waves are scattered as much as what is necessary for a diffuse field. Furthermore, the values show that ultrasound waves travel through all materials as is necessary to detect small changes in the different phases of the medium.

5.2 Experimental Procedure

Three different experiments were performed in this research: the thermal damage experiment, the ASR damage experiment and the cyclic loading experiment. The basis of all three experiments is made up of ultrasonic measurements during the uniaxial compression of the specimens, which is the same for all three experiments and this compression is performed several times in each experiment. The differences between the three experiments is on what is done during the intermediate time between the acoustoelasticity measurements. In the following, the common compression cycle for the acoustoelasticity measurement is explained which is the common ground for all three experiments. Next, the three different experiments are explained.

5.2.1 Experimental Setup and Procedure

The basis of all three experiments are ultrasonic measurements during the compression cycle of the specimens towards the goal of a post-processing evaluation of the data using Eq. 3.54. The setup of the compression cycle is shown in Fig. 5.12. The compression of the concrete is performed starting at 3 MPa up to 4 MPa. It was compressed in a step of 100 kPa. The preliminary load of 3 MPa was applied because concrete shows a large nonlinear behavior at lower stress levels. Preliminary tests were performed in this research at lower stress levels, starting from 0 MPa up to 3 MPa. No good results were obtained from these tests: there was no visible trend of relative velocity change ν . As a consequence, a preliminary load of 3 MPa was applied at all tests of this research. Note that also [27] applied a preliminary load of 5 MPa. As described in Sec. 2.4, the concrete's microstructure begin to change

at stress levels of 30% of the ultimate strength f_c'. For this reason, the preliminary load is set as low as possible in order not to induce any change in the conrete's microstructure during the compression cycle. A preliminary load of 3 MPa is a good compromise between a too low stress level that results in incosistent data and a too high stress level that may result in initial microdamage. The step size of 100 kPa and the highest stress level of 4 MPa allows to get enough data points for a linear fit to the data points.

The total time of one compression cycle with ultrasonic measurement is a bit less than 12 minutes. At each of the 11 stress levels (including stress level of 3 MPa), the stress (load) was constant and long enough to perform the ultrasonic measurement (according to Fig. 5.12) and to save the acquired waveforms h_0 and h_k in the oscilloscope. The time-stress history is shown in Fig. 5.13. Compression of concrete leads to creep as described in Sec. 2.6. The total duration of one compression cycle is less than 12 minutes, but noticeable creep can occure in the order of days [34]. Furthermore, the maximum stress of 4 MPa is just not high enough to cause microcracks in the interfacial transition zone, which is also described in Sec. 2.6. Subsequently, it is feasible to neglect the effect of creep and any damage due to this load.

5.2.2 Thermal Damage Procedure

The complete thermal damage procedure for a concrete specimen consists of four compression cycle in total. Between each cycle, the specimen is placed in an oven and heated up to 120° Celsius for about 3 hours in order to introduce thermal damage in the concrete as described in Sec. 2.3. The total time in the oven was 9 hours. After removing the specimen from the oven, it was cooled down to room temperature for 1 day in order not to allow a temperature change of the specimen during the compression cycle. The whole thermal damage procedure is shown in Fig. 5.14. Note that 21° C

refers to room temperature.

5.2.3 ASR Damage Procedure

The ASR damage procedure is similar to the thermal damage procedure. The complete ASR damage procedure for a concrete specimen consists of 4 compression cycle. Between each cycle, the specimen was placed in an oven with humid environment in order to introduce ASR damage in the concrete as described in Sec. 2.2. The time in the oven between each ultrasonic measurement was 15 days. The temperature in the oven was 60° C. After removing the specimen from the oven it was cooled down to room temperature for 1 day in order not to get a temperature change of the specimen during the compression cycle with ultrasonic measurement. The whole ASR damage procedure is shown in Fig. 5.15.

5.2.4 Cyclic Loading Procedure

The cyclic loading procedure differs from thermal damage procedure and ASR damage procedure. After one compression cycle with ultrasonic measurement was done, the next compression cycle immediately followed after a few seconds time to allow setting the test frame. In that way, a total of 12 compression cycles are performed with a total duration of a bit less than 3 hours. The specimen was placed a day before in the room with the test frame in order to adapt to the temperature in that room since the duration of this experiment is longer than the other two and temperature may affect the result. Also here, the effect of creep can be neglected. The duration of almost 3 hours is much longer than the two other experiments, but since creep takes into account in terms of days, and since there is a brake of around 1 minute between each compression cycle causing a partial recovery from softening, it is feasible to neglect the effect of creep. The whole cyclic loading procedure is shown in Fig. 5.16.

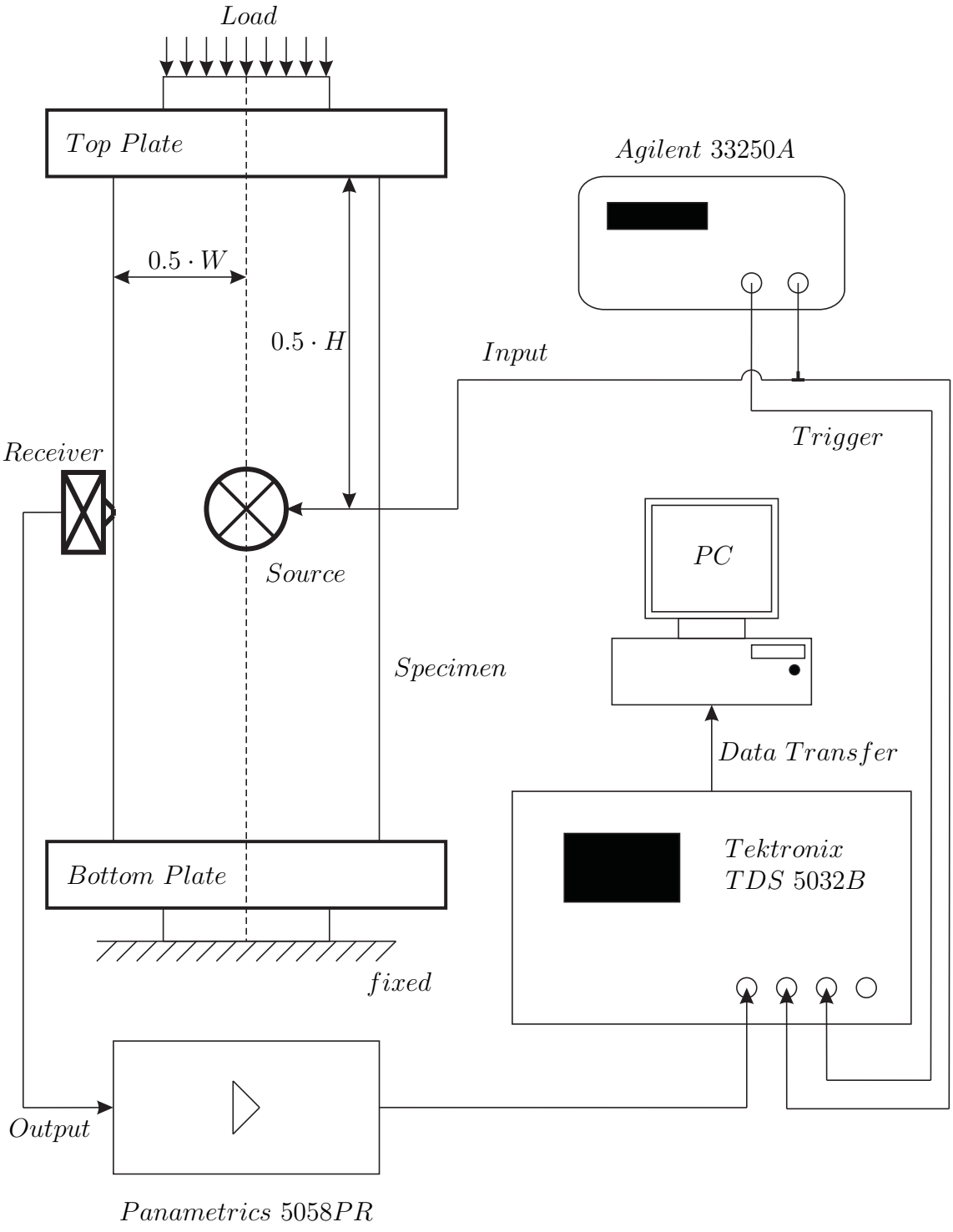

Figure 5.12: Experimental Setup of Compression Cycle.

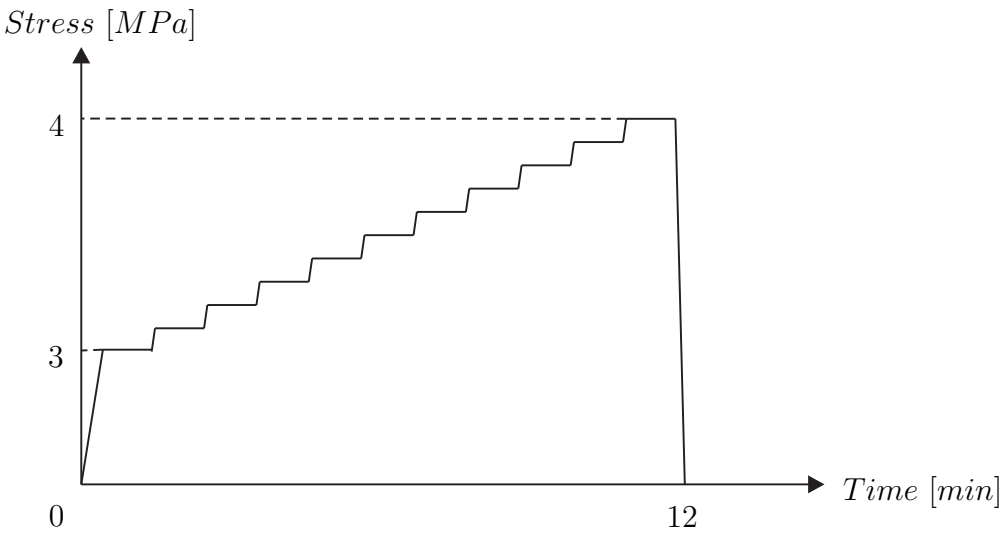

Figure 5.13: Time-Stress History of One Compression Cycle.

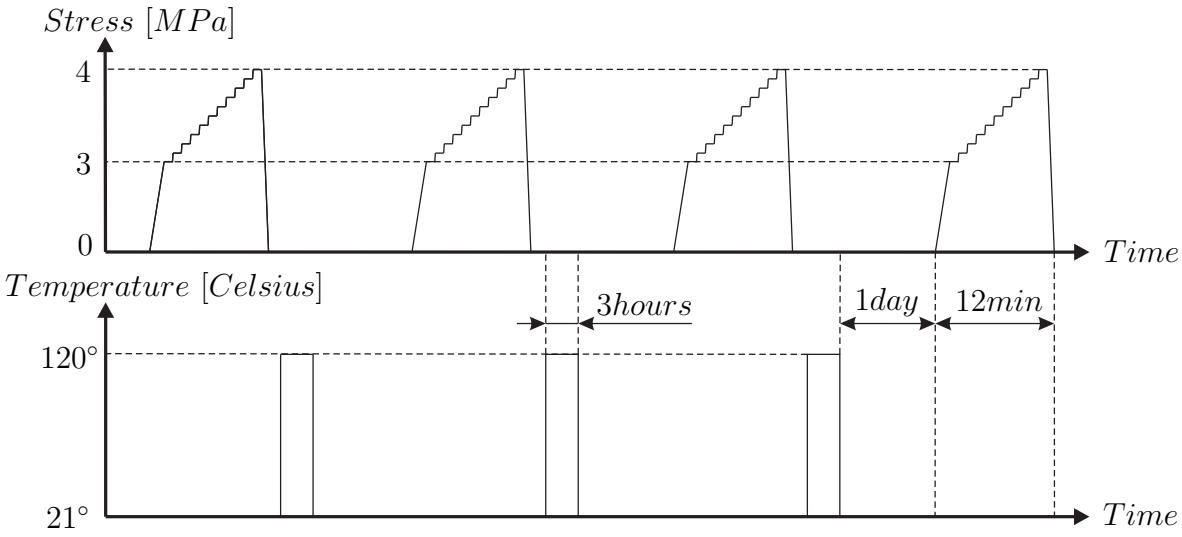

Figure 5.14: Thermal Damage Procedure over Time.

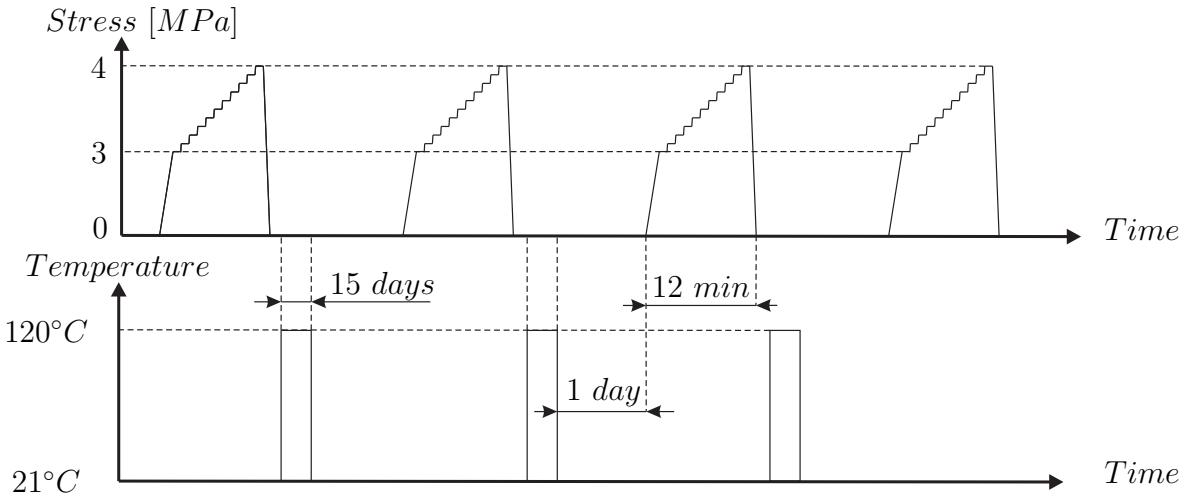

Figure 5.15: ASR Damage Procedure over Time.

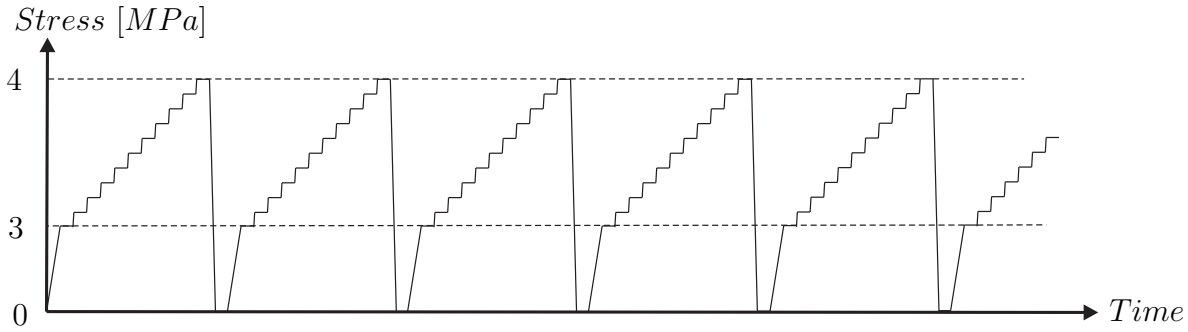

Figure 5.16: Cyclic Loading Procedure over Time. Total of 12 Cycles.

CHAPTER VI

RESULTS

The results of the three experiments are considered as well as possible influences such as temperature and strain are described and discussed. Furthermore, the repeatability of the measurements and the post-processing steps are described and discussed.

6.1 Relative Velocity Change as a Function of Stress

The results of this research are given as relative velocity change as a function of Stress.

As explained in Chap. 4, the relative velocity change between two waveforms is the result of ST. According to Sec. 3.3, the more a medium gets compressed, the faster waves travel. Thus, we expect the relative velocity change to increase as concrete gets compressed. For every stress level, shown in Fig. 5.13, the relative velocity change is calculated using the same h_0 obtained at the first stress level. The complete data of one compression cycle is shown in one relative velocity change over stress plot such as Fig. 6.13. The post-processing steps will be explained in Sec. 6.5. The slope of these data yields a measure of nonlinearity as already stated in Sec. 3.3. In the following, the relative velocity change results and the nonlinearity are presented for all three experiments.

6.2 Transducer Configuration

The choice of the transducer position on the specimens is mainly because of two reasons.

First, a directly opposed configuration of the transducer set would result in a significant portion of ballistic waves in the impulse response. As already described, the ballistic waves are the first arrivals and travel without much scattering directly

from transducer to transducer. Accordingly, they are less sensitive to microcracks and damage in the medium than the later arrivals and therefore not very capable of detecting any change. Since they carry a huge amount of energy and are not sensitive to change but applicable in the impulse response, they are not practical for ST and would corrupt the result of relative velocity change. Therefore, the transducer were placed in a way that their axes make up a 90° angle between them, resulting of a significantly smaller portion of ballistic waves in the impulse response. The cross section of the specimens with the used perpendicular and the unused opposite configuration is shown in Fig. 6.1.

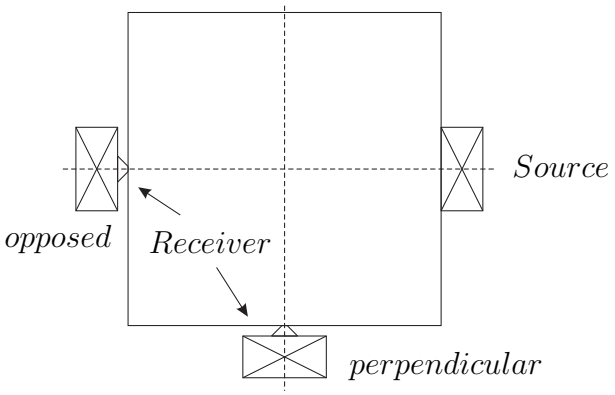

Figure 6.1: Transducer Positions: opposite and perpendicular.

Secondly, the grip through the top and bottom plates of the test frame result in different boundary conditions at those surfaces compared to the 4 side surfaces. This may effect waves traveling to the fixed surfaces and backscattering of those waves can lead to different waveforms measured with the receiving transducer. In this case, the boundary conditions given through the top and bottom plate of the test frame need to be considered.

The length of the specimens is given with $H = 30.48cm$. Placing the transducers at $0.5 \cdot H$ results in the longest possible distance to top and bottom plate, as shown in Fig. 5.12. Consider a typical impulse response obtained from one of the specimens, shown in Fig. 6.2. The impulse response can be described by the diffusion envelope

[14]

$$E = \frac{P_0}{4D\pi t} e^{-r^2/(4Dt)} e^{-\sigma_D t} \tag{6.1}$$

where P_0 is the released source energy, D the diffusivity parameter, t the time, r

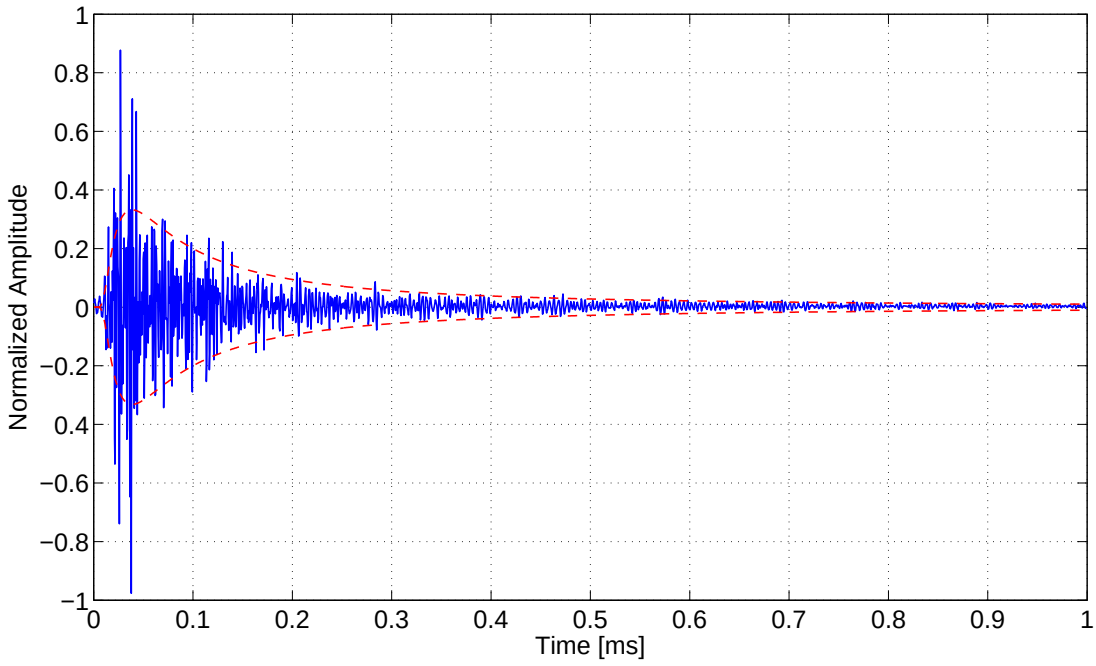

Figure 6.2: Typical Impulse Response with Diffusion Envelope (dashed line).

the distance between source and receiver and σ_D is the dissipation rate. It was found that the diffusion envelope described by Eq. 6.1 fits the impulse response from Fig. 6.2 best for $D = 25\frac{m^2}{s}$ and $\sigma_D = 50\frac{m}{s}$. The two values are a rough estimation but are in agreement with the literature [14]. The high value of the diffusivity parameter D clearly indicates the strong scattering regime, what is in agreement with Sec. 5.1.6.3. To make sure that waves which travel to the bottom or top plate and back do not influence the measured diffuse field, one can compare the the energy amplitudes. Waves traveling from source to top or bottom and back to the receiver pass at least a distance of $2 \cdot l$. Waves traveling directly from source to receiver pass a distance of p. The situation is shown in Fig. 6.3. Waves traveling to top or bottom and back

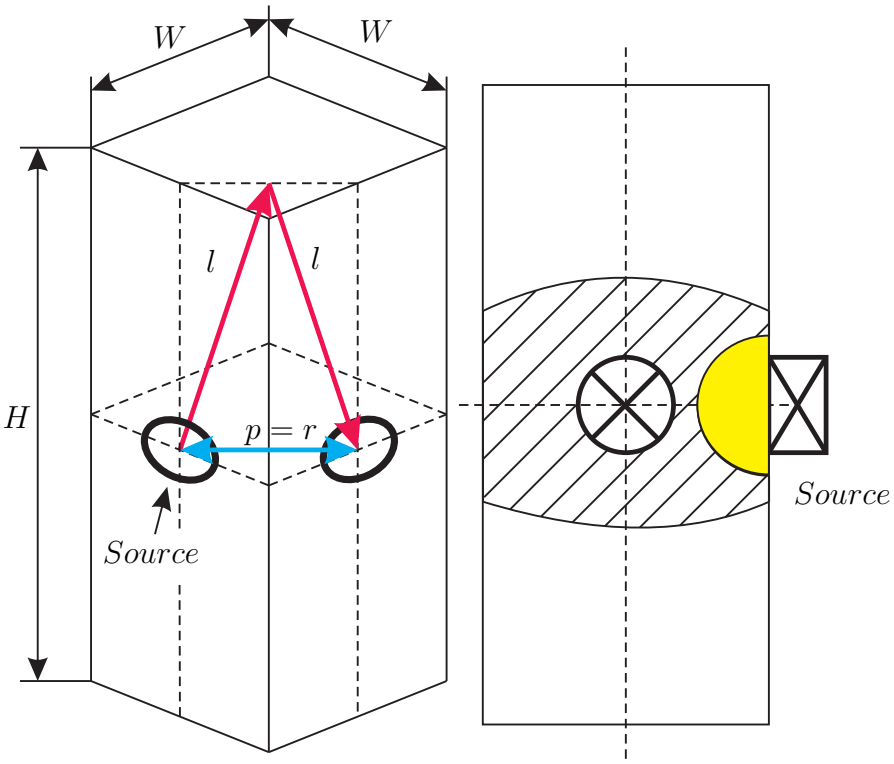

Figure 6.3: Distances (left) and Diffuse Field (right).

travel a distance of $2l = 30.952cm$ and direct waves travel a distance of $p = 5.388cm$. Eq. 6.1 becomes only a function of the distance r since σ_D, D and P_0 are the same for both distances. Adapting Eq. 6.1, the amplitude ratio is now given by

$$R_A = \frac{E_{2m}}{E_p} = \frac{e^{-(2m)^2}}{e^{-p^2}} \approx 0. \tag{6.2}$$

An amplitude ratio of approximately 0 indicates that waves traveling to top or bottom have an amplitude of 0 when they would arrive at the receiver. Thus, they do not exist anymore and do not effect the diffuse field. This means that any change through local damage occurring at the top and bottom plate of the specimen due to the load plates will not be detected by the receiving transducer.

The diffusivity can now be used to calculate the transport mean free path l^*. The transport mean free path is the mean distance after which the direction of propagation of the energy is fully randomized [36]. Thus, after a distance l^*, starting from the

source, the diffuse field is assumed to begin and can be calculated [36] using

$$l^* = \frac{3D}{v_e} \tag{6.3}$$

where v_e is the average velocity at which energy is transported. To make sure that waves are diffuse before they reach the receiver, the distance l^* must be smaller than the source-receiver distance as shown in Fig. 6.3. The energy velocity can be approximated using the arrival time t_a of the first waves extracted from the typical impulse response of Fig. 6.2 and is shown in Fig. 6.4. The velocity is calculated using $v_e = \frac{r}{t_a}$ with the spatial distance r between the two transducers that is given by $r = 5.388\,cm$ as shown in Fig. 6.1. An arrival time of $t_a = 11\mu s$ is extracted from Fig. 6.4. The energy velocity yields $v_e = 4752\frac{m}{s}$, what is in accordance with the literature [14], and the transport mean free path yields $l^* = 0.0157m$. This rough approximation of the transport mean free path concludes that diffuse field is fully generated before waves arrive ar the receiver. The situation is shown in Fig. 6.3. The blackened area with radius l^* indicates the volume no diffuse field is assumed. Outside this volume, diffuse field is expected and the assumed area is indicated as hatched lines. Out of this area the energy is sufficiently low.

To summarize, the perpendicular position of the transducer is necessary to eliminate the ballistic waves and to concentrate on the diffuse field. The position at the height $0.5 \cdot H$ assures that local change due to the top and bottom plate do not affect diffuse measurement.

6.3 Temperature Influence

The temperature change between a compression cycle can affect the results of relative velocity change [30, 31]. A huge temperature increase during an compression cycle would probably result in an volumetric extension of the specimen. The spatial distance between source and receiver would change and therefore the arriving times would be different.

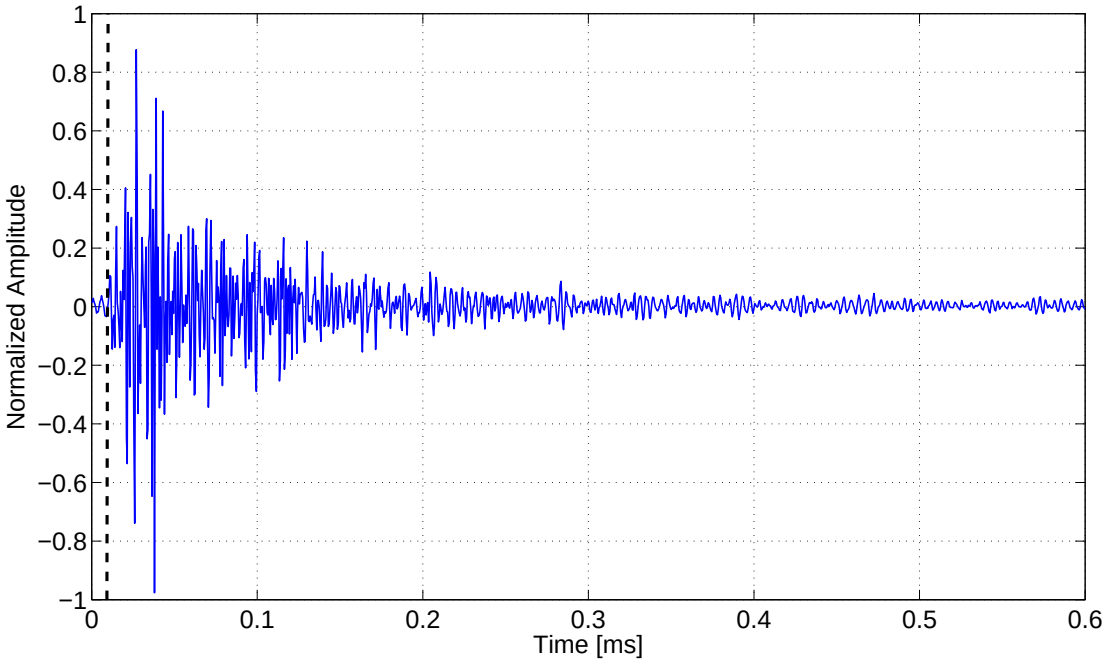

Figure 6.4: Impulse Response of Fig.6.2. Dashed line indicates arrival time.

In this research, the used concrete specimen was placed in the room with the compression machine for one day before testing in order to adapt to air temperature. Furthermore, the air temperature was measured before and after each compression cycle close to the specimen using a thermo couple. The temperatures of each experiment are given in Sec.6.7, 6.8 and 6.9. The temperature changes are in the order of 0.2° C-0.5° C. Such small changes would not induce large velocity changes since thermal diffusion is very slow [27] and the duration of one compression cycle is less than 12 minutes.

6.4 Influence of Strain

Compressing the concrete in length leads to an increase in width. This relationship is described by the Poisson's ratio ν and is defined as the ratio between relative change

in length over relative change in width

$$\nu = -\frac{\Delta W/W}{\Delta H/H} = -\frac{\epsilon_W}{\epsilon_L} \tag{6.4}$$

with W and H as defined in Fig. 5.12. One can also link the Young's Modulus E to the shear modulus G using the Poisson's ratio [34]:

$$E = 2G(1 + \nu). \tag{6.5}$$

The concrete specimens used in this research are moderate-strength concrete specimens according to the mix-design. Typical Young's modulus of moderate-strength concrete are in the order of 28 GPa according to Tab. 2.1. Maximum compressive stress range at which ultrasound measuremens are performed in this reseach is 1 MPa, that is the difference between maximum stress of 4 MPa and preliminary stress of 3 MPa, as shown in Fig. 5.13. Calculating the longitudinal strain change due to 1 MPa using $\epsilon_L = -\frac{\sigma}{E}$ yields $\epsilon_L = -3.5714 \cdot 10^{-5}$. Using Eq. 6.4 and a typical value for the Poisson's ratio given by [34] with a range of $0.15 \leq \nu \leq 0.2$ or $\nu = 0.18$ for moderate-strength concrete from Tab. 2.1 yields in a thickness increasing by $\epsilon_W = 6.4286 \cdot 10^{-6}$. Assuming a constant velocity, the thickness strain ϵ_W is equal to the relative time change and due to Eq. 4.11 it is equal to the negative of the relative velocity change. The relative velocity changes measured in this research due to stress are on the order of $1 \cdot 10^{-4}$ per MPa. Thus, the strain induced relative velocity change of $6.4286 \cdot 10^{-6}$ per MPa is around 16 times smaller, that is smaller than one order of magnitude than stress induced relative velocity change and can be therefore neglected, what is also consistent with the literature [27].

6.5 Post-Processing Steps

After the waveforms obtained from the experiment have been saved in the oscilloscope they are transferred to a computer. The reference waveforms are named s_0 and r_0, also described in Sec. 3.4.1, where s means source signal and r means receiver signal.

The number 0 indicates the reference stress level. The other waveforms are called s_k and r_k, where $k \in [1;10]$ corresponds to these signals at each applied stress level. Each s_k and r_k makes a pair. All waveforms are given as vectors. The post-processing is mainly done with Matlab and the steps are as follows:

1. Pulse Compression. Perform the cross-correlation operation according to Eq. 3.61 of each waveform pair s_k and r_k for $k \in [0;10]$. The result is h_k for $k \in [0;10]$, where h_0 represents the reference waveform. The vectors h_k are of length $(2N-1)$ as it can be seen in Eq. 3.65 and described in Sec. 3.4.1. The impulse response in h_k can be found in the range [N,N+2000]. N represents the time 0 and N+2000 represents 1 ms. Cut vectors h_k in a way that they consist only of the range [N,N+2000]. The impulse response is now visible. The same range is used the signal shown in Fig. 6.2.

2. Coda Wave Interferometry. The interferometry is done over $600\mu s$ since the amplitude after $600\mu s$ is very low and does not effect the result, what is in accordance with the literature [27]. Therefore, h_k is cut down to vector length of range [0,1200]. Next, each h_k for $k \in [0;10]$ is compared to h_0 using Eq. 4.16 (note that the result of comparing h_0 with h_0 is always the expected relative velocity change $\nu = 0$). The range of ν is user-selected and is chosen to be $-0.005 \leq \nu \leq 0.005$. The algorithm used for Eq. 4.16 and 4.17 is as follows:

   1. Stretch (or shrink) the time axis of h_k (begin with k=1: h_1) with the first ν of the given range.

   2. Cut h_k in order to have the same length in time as h_0 since it is longer in time after stretching (equivalent to zero-padding of h_0).

   3. Interpolate h_k using spline functions with the time axis of h_0 as new time axis. The vector components of h_k fit the vector components of h_0 now in time, that means Δt for h_k matches Δt for h_0.

In the first 3 steps, the time-stretch term of Eq. 4.16, that is $t(1-\nu)$ of h_k, is done so far.

4. Calculate the cross correlation coefficient for the new h_k and h_0.

5. Determine the ν that maximizes the cross-correlation coefficient (CC_k).

6. Save both values, the ν and the corresponding CC_k.

7. Perform step 1 to 6 again for the whole user-selected range of ν.

One has now calculated $CC_k(\nu)$ (Eq. 4.16) and obtained all extrema CC-values over ν.

8. Determine the maximum CC_k-value of $CC_k(\nu)$.

9. The corresponding ν to the maximum CC_k of step 8 is the relative velocity change ν_k. Note that the obtained maximum CC_k values in this research are in the order of 0.994 representing good correlation of two waveforms.

One has now determined the relative velocity change between h_0 and h_1 according to Eq. 4.17.

10. Do step 1 to 9 again for h_k for $k \in [2;10]$ and determine ν_k for $k \in [2;10]$.

One now obtains the relative velocity changes over the stress-levels e.g. $\nu_k(\sigma)$, since each k represents one stress-level.

3. Nonlinearity. Fit a linear equation to $\nu_k(\sigma)$. Determine the slope of the linear fit. The slope's unit is $[\frac{\nu}{\sigma}]$. According to Eq. 3.55, the slope is equal to $-\frac{\beta}{E}$, a measure of nonlinearity.

4. Experiments. In the thermal damage experiment, 4 compression cycles were done resulting in 4 different linear fit curves and 4 slopes. Accordingly, the previous steps must be done 4 times. In the ASR-damage experiment, also 4 compression cycles were done resulting in 4 linear fit curves and slopes and in

the cyclic loading experiment 12 compression cycles were done resulting in 12 curves and slopes.

6.6 Repeatability

In order to compare measured results $[\frac{\beta}{E}]$ at different damage levels, the measurement itself must be repeatable. In the thermal damage experiment and in the ASR-damage experiment the two transducers were taken off from the specimen for the heating phase in the oven. Detaching the transducer before heating phase and reattach them again for the next compression cycle may result in a measurement error. In a preliminary test, this possible error was assessed. A concrete specimen was compressed 5 times

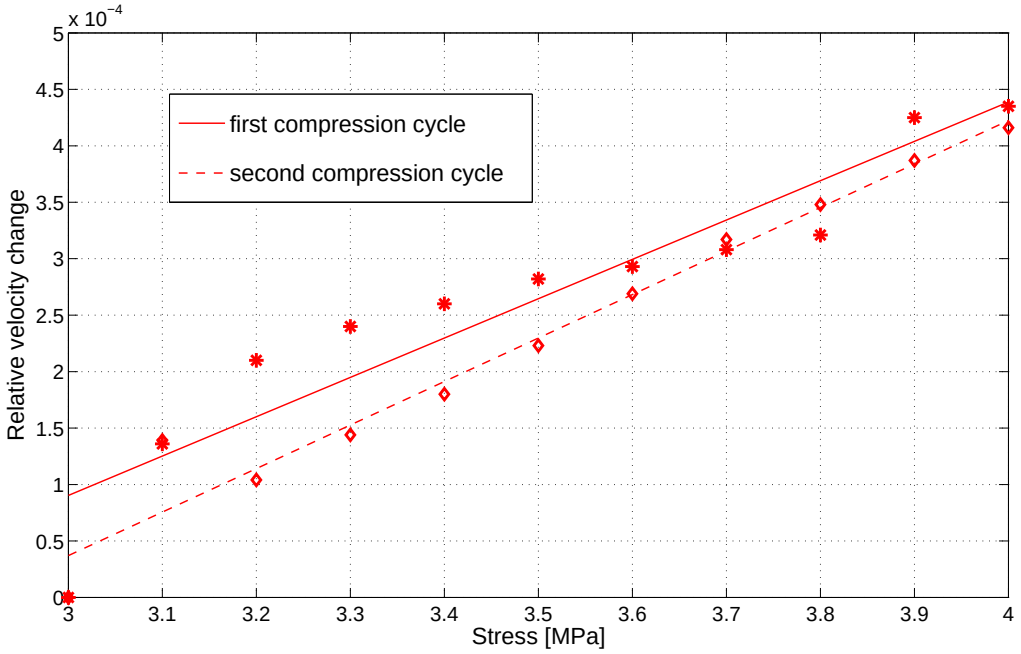

Figure 6.5: Repeatability. Slopes of first and second compression cycle.

according to the described setup (Fig. 5.12) and procedure (Fig. 5.13). Between each compression cycle, the transducers were detached and reattached again to simulate the ultrasonic measurements for the thermal- and ASR-damage samples. Furthermore, the time between each compression cycle was at least 5 hours for full recovery of the Young's modulus since Young's Modulus may change if compressed directly after each

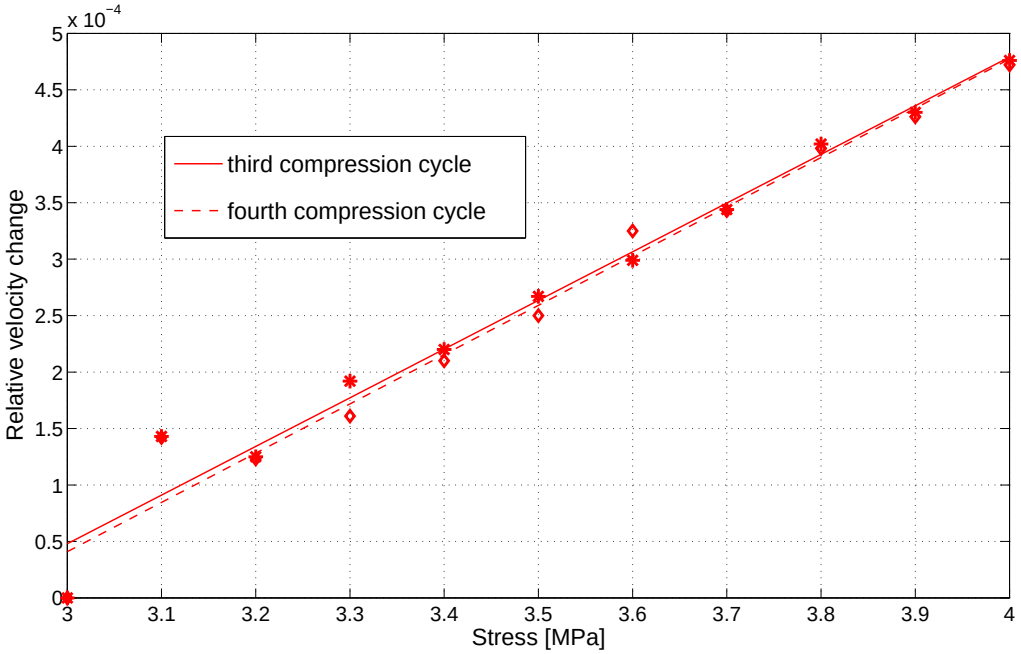

Figure 6.6: Repeatability. Slopes of third and fourth compression cycle.

other, as shown in Fig. 2.2 and explained in Sec. 2.4. The post-processing steps were performed and the 5 slopes were obtained and compared. The results are shown in Fig. 6.5, 6.6 and 6.7.

The maximum slope variation is $\frac{\Delta\nu}{\Delta\sigma} = 8 \cdot 10^{-5}$, representing the maximum error through detaching and reattaching the transducers to the specimen. The error is mainly due to the following 2 reasons: firstly, it is impossible to reattach the transducers at the exact same position again as they were during the previous compression cycle. The resulting error due to that reason is small since we do not measure absolute velocities, but relative velocities. And relative velocities are calculated in comparison to h_0 which is measured at each compression cycle again. Secondly and mainly, the bigger portion on the error may be due to the couplant gel which couples transducers to the concrete surface. It is very hard to keep the thickness and amount of the couplant layer the same for all measurements resulting in different transducer sensitivity and characteristic. The wave velocity changes in the concrete due to stress, but not

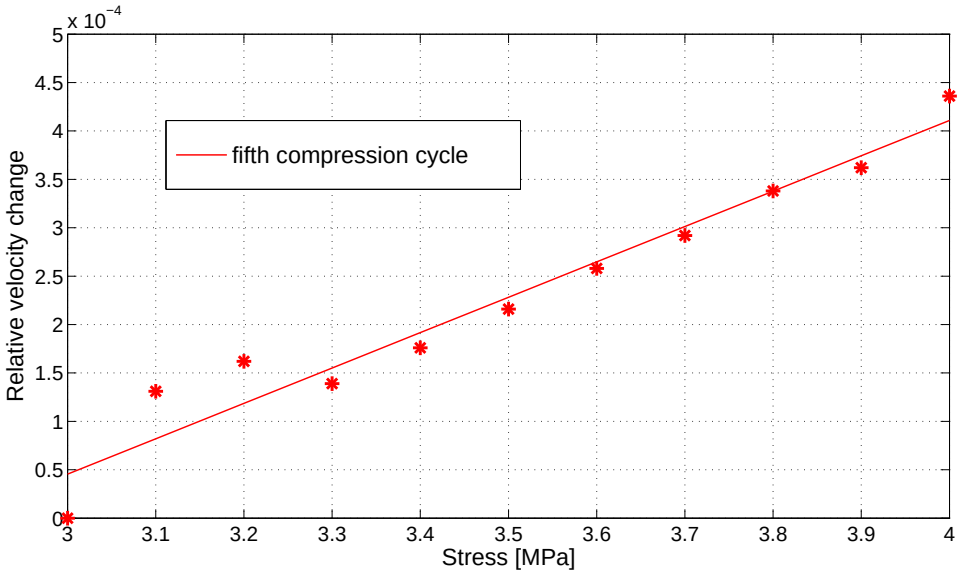

Figure 6.7: Repeatability. Slope of fifth compression cycle.

in the couplant since it is not compressed in any way or is not much affected of the concrete compression.

6.7 Results of Thermal Damage Experiment

The thermal damage experiment was performed for 3 specimens: LRS7, LRS8 and LRS9. The curing time of all three specimens was 6 days before the first compression of thermal damage experiment. In the following, the 4 linear fit curves of all 3 specimens resulting from the compression cycles are shown (Fig. 6.8-Fig.6.13). For each curve, the standard deviation of the linear fit is calculated using

$$SD = (\frac{1}{n}\sum_{i=1}^{n} j^2)^{\frac{1}{2}} \tag{6.6}$$

where j is the distance from measured point to the linear fit and the number of data points, e.g. $n = 11$. As it can be seen, the slopes increase from cycle to cycle as more and more thermal damage is introduced into the specimens. This relationship can be seen in Fig. 6.14. Note that the quality of the data in terms of linearity is always the worst for the first compression cycle, which can be seen especially in Fig. 6.8 or in Fig. 6.12. In Fig. 6.8, some relative velocity values are lower than the

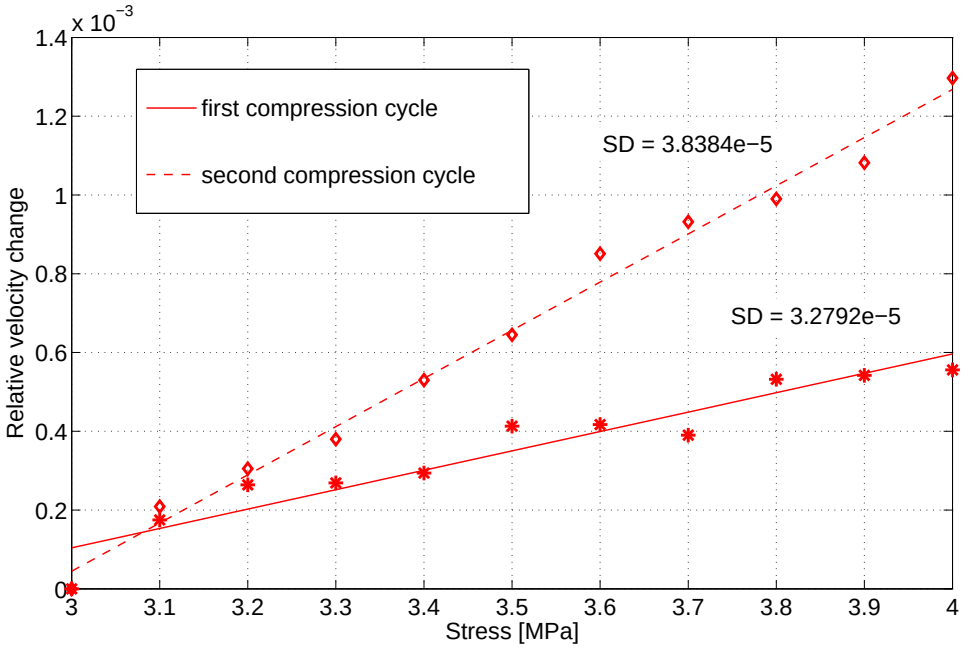

Figure 6.8: Thermal Damage: Results of first and second compression cycle of LRS7.

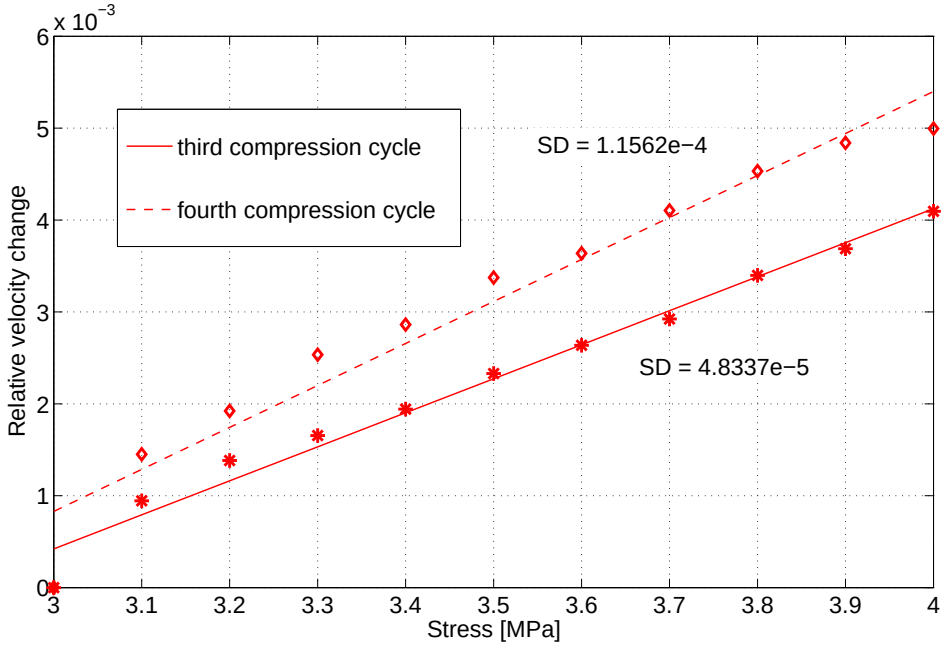

Figure 6.9: Thermal Damage: Results of third and fourth compression cycle of LRS7.

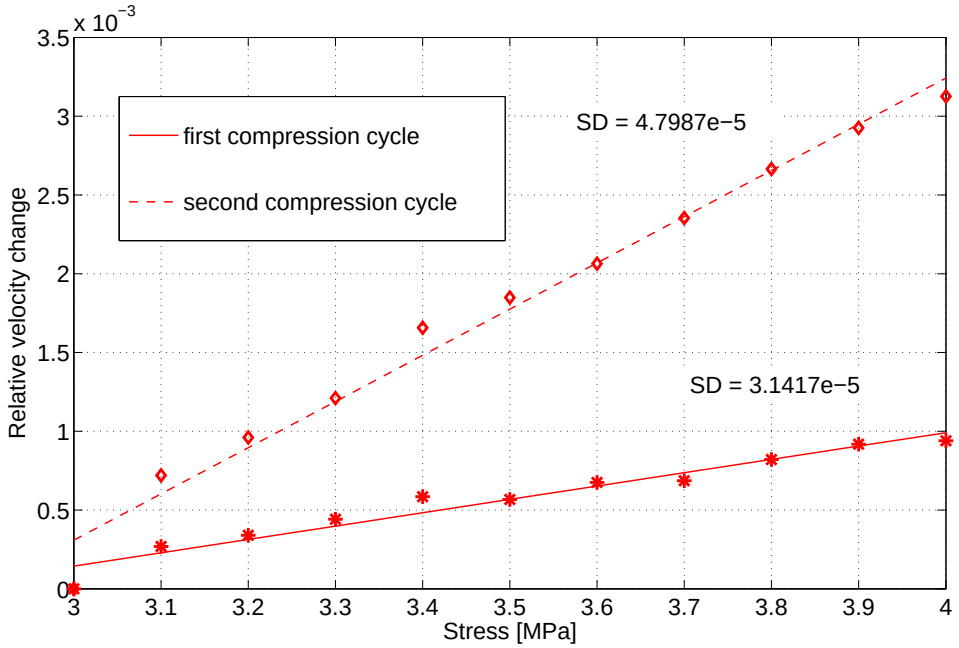

Figure 6.10: Thermal Damage: Results of first and second compression cycle of LRS8.

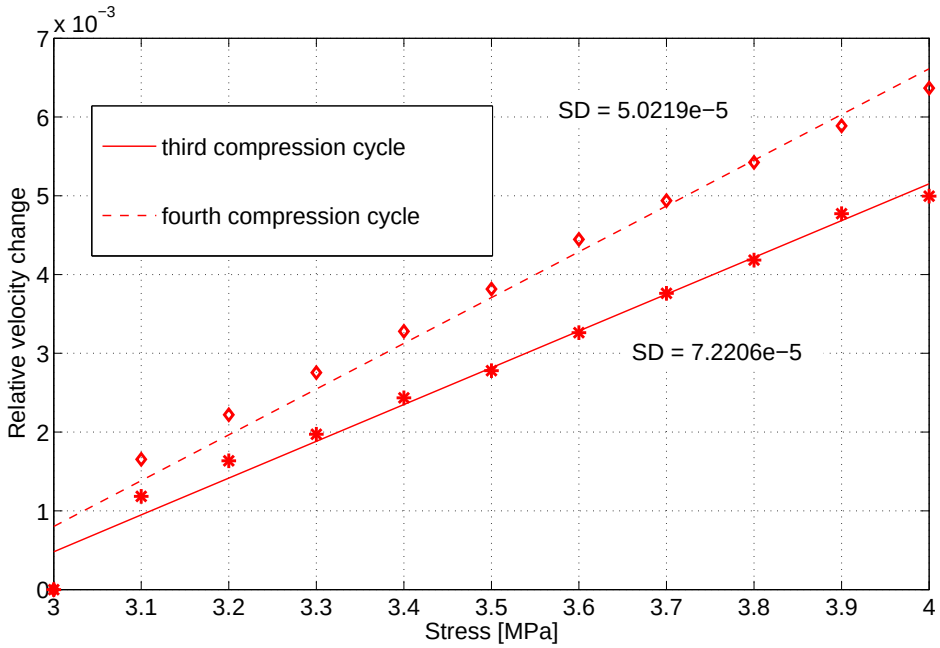

Figure 6.11: Thermal Damage: Results of third and fourth compression cycle of LRS8.

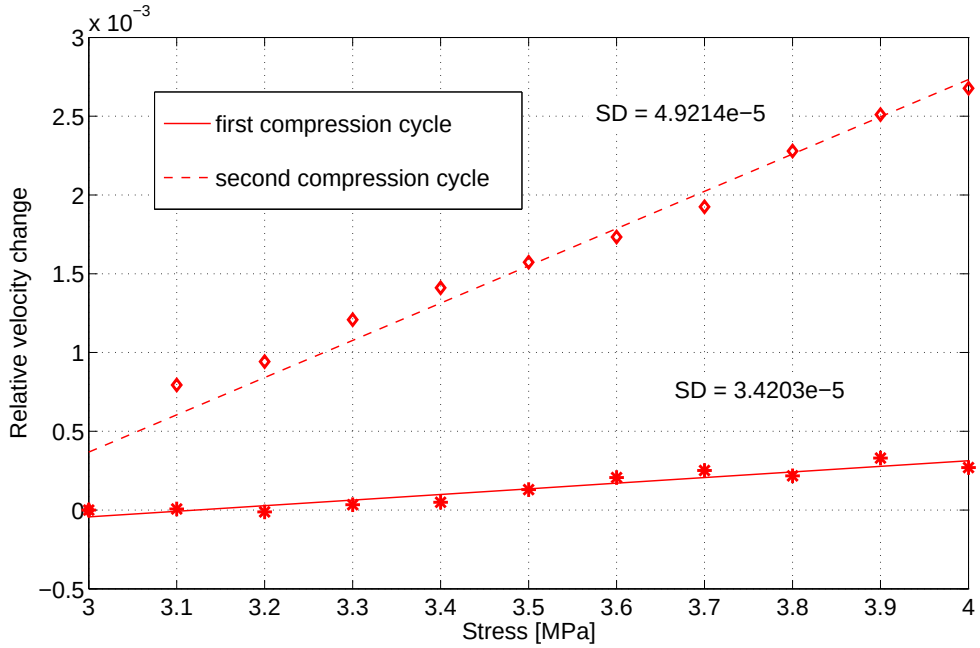

Figure 6.12: Thermal Damage: Results of first and second compression cycle of LRS9.

previous ones and Fig. 6.12 shows a negative relative velocicty value at 3.2 MPa. It is very hard to get a good linearity at the very first compression cycle which is consistent with preliminary tests conducted during this research. The measured room temperature at those tests varied, like at the other tests, with a temperature change of max. 0.6°C. The minimum and maximum measured temperature were 22.1° and 23° Celsius. Because of the short time of one compression cycle and because of the small temperature changes within one compression cycle, the temperature influence can be neglected, as already discussed in Sec. 6.3

6.8 Results of ASR Damage Experiment

The ASR damage experiment was performed with 2 specimens: HRS1 and HRS2. The curing time of both specimens was 19 days (time between removing them from the molds until first compression cycle). In the following, the 4 linear fit curves for both specimens resulting from the compression cycles are shown (Fig. 6.15-Fig.

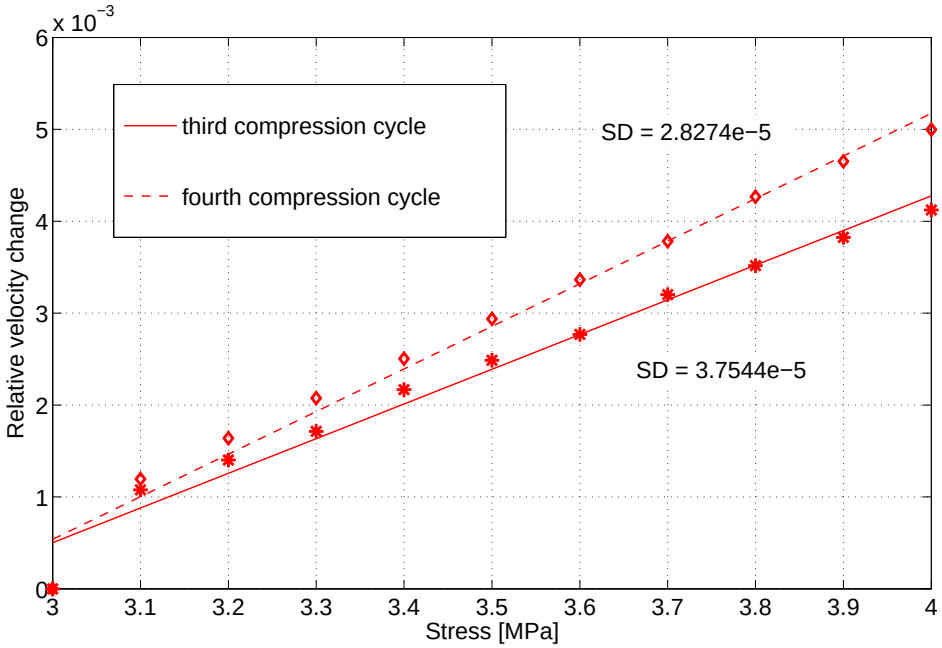

Figure 6.13: Thermal Damage: Results of third and fourth compression cycle of LRS9.

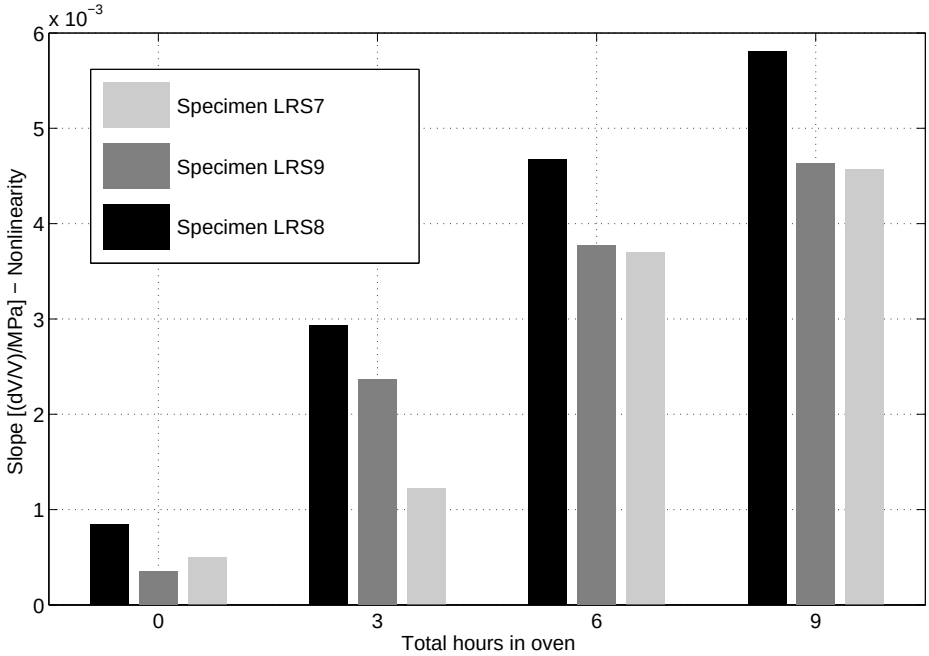

Figure 6.14: Thermal Damage: Slope increasing over time in oven.

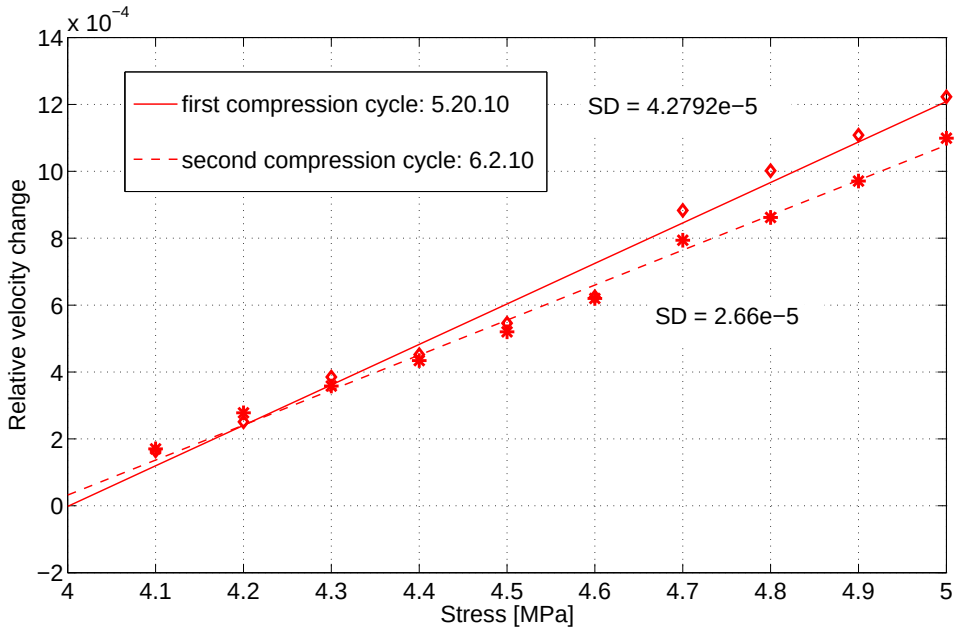

Figure 6.15: ASR Damage: Results of first and second compression cycle of HRS1.

6.18). The standard deviations for each linear fit are shown and the slope increase over exposure time (oven time) is shown in Fig. 6.19. Note that the stress range used for the compression cycles here is from 4-5 MPa, and not 3-4 MPa as in the two other experiments, because the ASR damage experiment began first, before the two other experiments, and linearity was found good for a range of 4-5 MPa. Later on, it was also found that a good linearity can be achieved for a range of 3-4 MPa. Also here, it is seen that the quality of linearity for the first compression cycle is not so good as those for higher number compression cycles. Also, the results of the second compression cycle of specimen HRS2 are not of very good quality. The temperature variation during the tests were similar as in the thermal damage experiment, minimum and maximum measured temperatures were 22.2° and 22.8° Celsius. Also here, the temperature influence can be neglected.

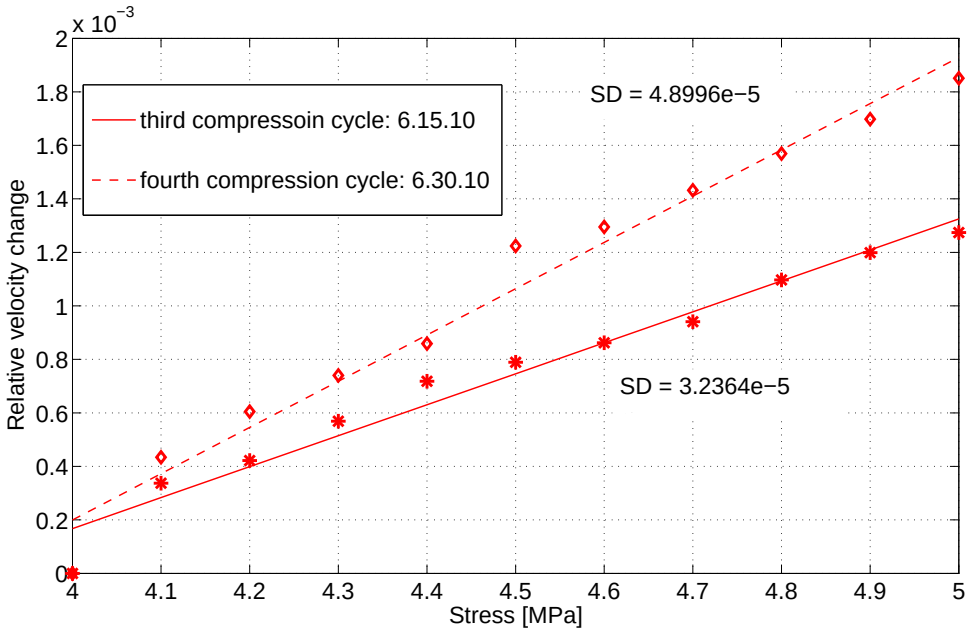

Figure 6.16: ASR Damage: Results of third and fourth compression cycle of HRS1.

6.9 Results of Cyclic Loading Experiment

The cyclic loading experiment was performed for two specimens LRS10 and LRS11. The curing time for LRS10 was 15 days and for LRSS11 16 days. Twelve repetitive compression cycles were performed resulting in 12 linear fit curves for each specimen. The standard deviations for each linear fit are shown and the slope increase over number of compression cycles is shown in Fig. 6.32. The quality of linearity at the first compression cycle of LRS11 is not as good as for higher number compression cycles and for LRS10, the linearity was so bad that there is even no trend visible. For this reason, the result for the first compression cycle of LRS10 is not shown in Fig. 6.20. Note also that due to saving difficulties the waveforms in the first compression cycle of LRS11 at stress level 3.8 MPa got lost and, therefore, this data point can not be shown in Fig. 6.26. Temperature variations were around the same range as in the other two experiments and can be therefore neglected. Also, during the twelfth cycle of LRS11 only the range from 3 - 3.5 MPa could have been saved, shown in Fig.

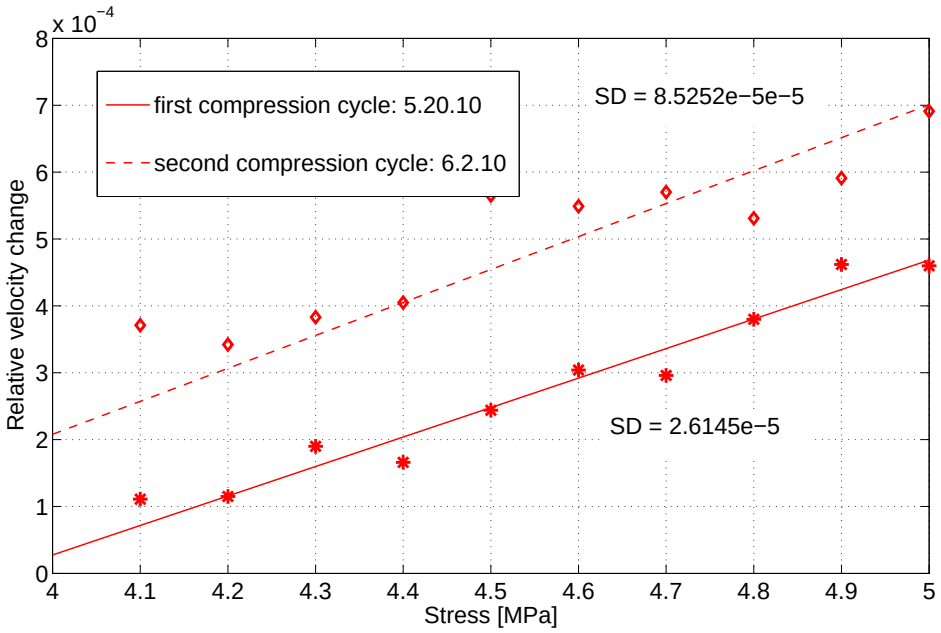

Figure 6.17: ASR Damage: Results of first and second compression cycle of HRS2.

6.31. Although the data for the range from 3 - 3.5 MPa shows a good linearity, the slope is not used in Fig. 6.32 due to insufficient data points.

6.10 Summary of Results

1. The technique of diffuse ultrasonic coda wave interferometry was successfully established. Larose found in [27] a linear fit slope of about $1 \cdot 10^{-6} \frac{\nu}{kPa}$. The slope of LRS7 of the first compression cycle (undamaged) is about $0.5 \cdot 10^{-6} \frac{\nu}{kPa}$, the first slope of LRS8 is about $0.8 \cdot 10^{-6} \frac{\nu}{kPa}$ and the first slope of HRS1 is about $1.2 \cdot 10^{-6} \frac{\nu}{kPa}$. The range of those values are in the same order of magnitude as Larose's value. This variation $(0.5 - 1.2 \cdot 10^{-6})$ is attributed to the variation of sample properties, which is inherent to these materials.

2. All slopes Φ are positive, meaning that the higher the stress, the faster the waves travel through the medium. This is in accordance with the theory.

3. The quality of linearity at the first compression cycle is generally not as good

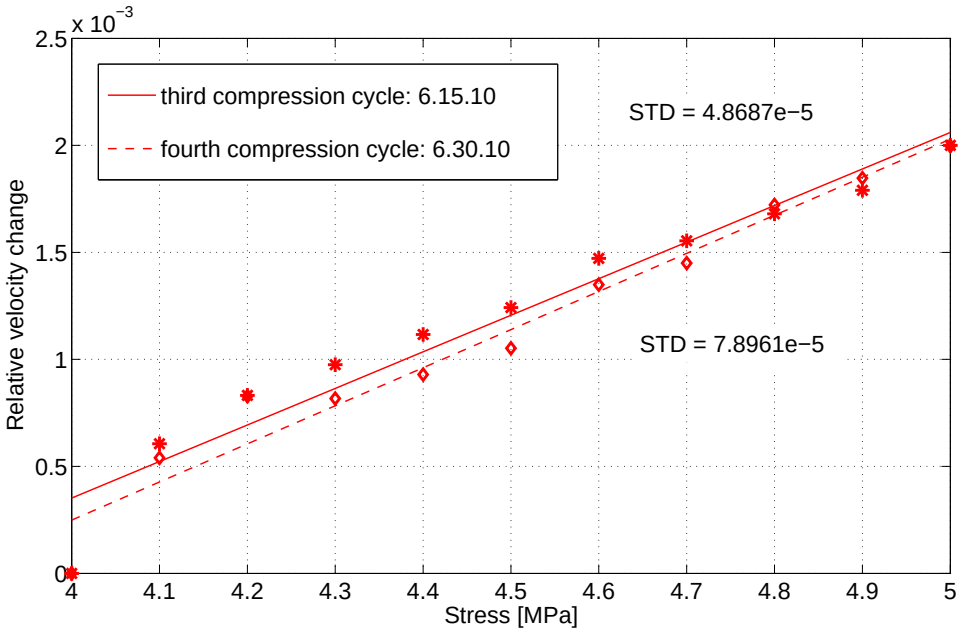

Figure 6.18: ASR Damage: Results of third and fourth compression cycle of HRS2.

as those of the following compression cycles. At the first compression cycle of LRS10, there could not even a reasonable linear fit be calculated since the relative velocity changes do not show any trend at all. This phenomena was also observed at a few preliminary tests.

4. The increase of relative velocity change from the first data point ($\nu = 0$) to the second data point is often the highest measured increase, resulting in a positive value for the linear fit curve to cross the ν-axis. Note that the value where the linear fit crosses the ν-axis has no physical meaning. Only the slope has meaning.

5. The relative velocity change through thermal damage seems to be higher in absolute magnitude than than the change through mechanical loading. The relative velocity change due to ASR-damage is the smallest measured, but since the alkali-silica reaction is of much longer time than the 43 days of reaction in

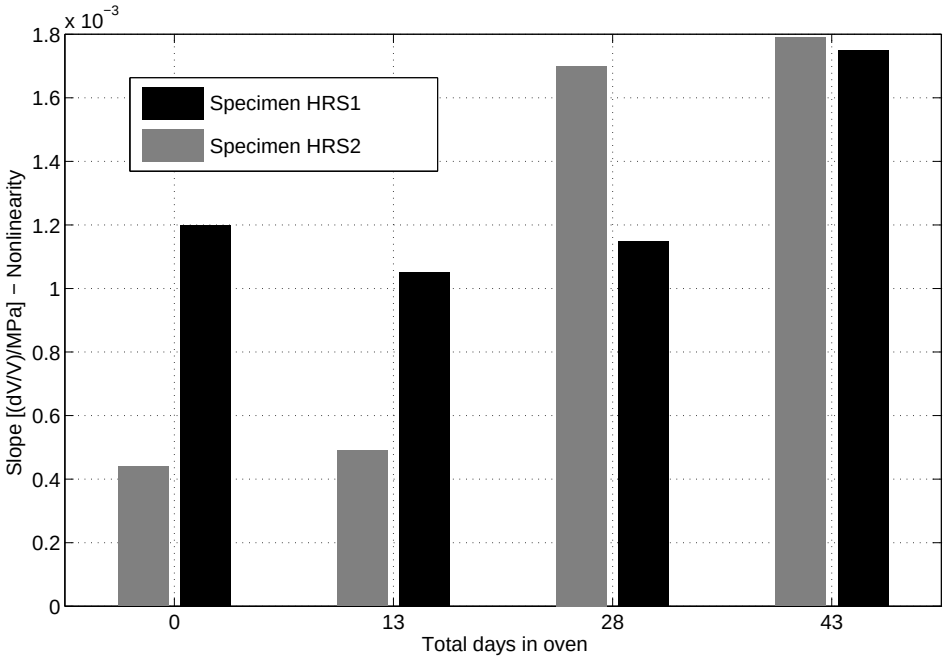

Figure 6.19: ASR Damage: Slope increasing over time in oven.

this research, the slope are assumed to increase further and to be higher in later stages of ASR-damage.

6. The slopes of the cyclic loading tests seem to converge for high cycle numbers. Most of the softening and increase in nonlinearity seems to occur in the first few cycles.

7. The results show that damage (small changes in the material) can be monitored using diffuse ultrasonic coda wave interferometry. The technique was found to be very robust compared to other ultrasonic measurement techniques.

8. All 3 damage types cause an increase of nonlinearity (slope Φ is increasing) of concrete. Theoretical models should be investigated to distinguish between the different damage types over time in real structures.

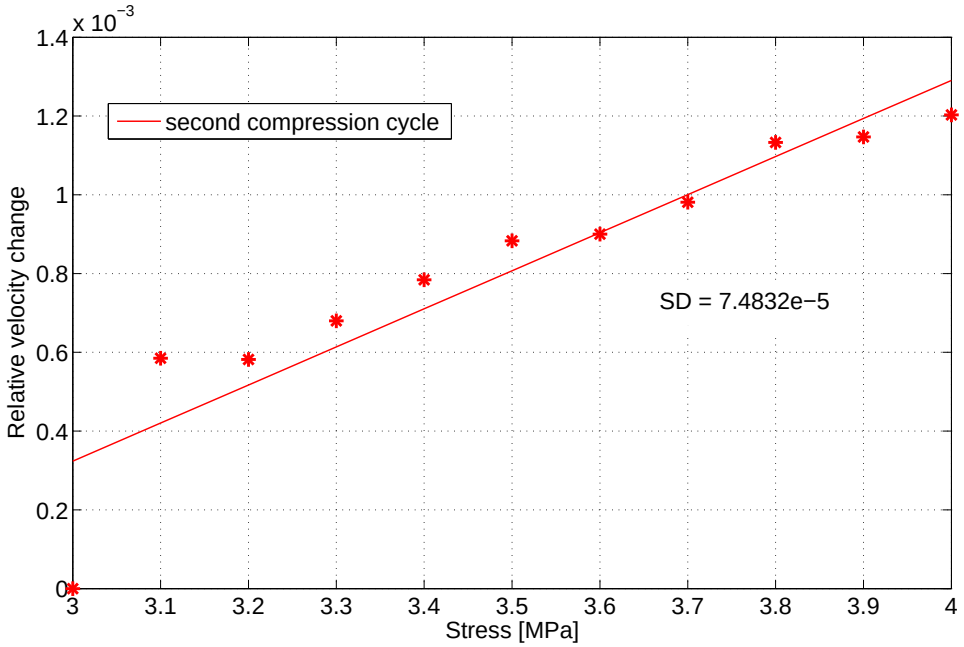

Figure 6.20: Cyclic Loading: Results of second compression cycle of LRS10.

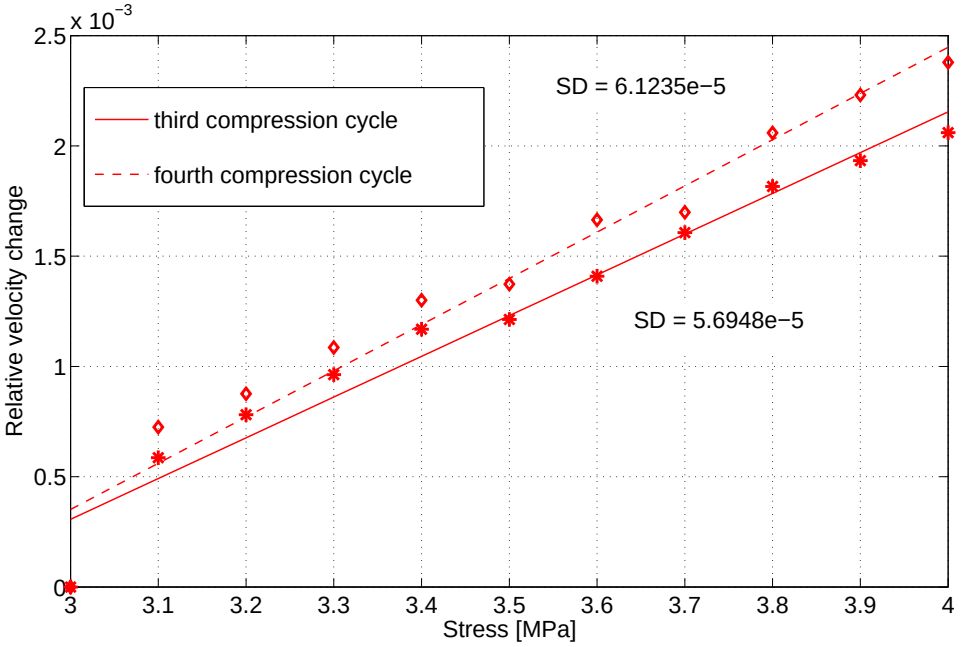

Figure 6.21: Cyclic Loading: Results of third and fourth compression cycle of LRS10.

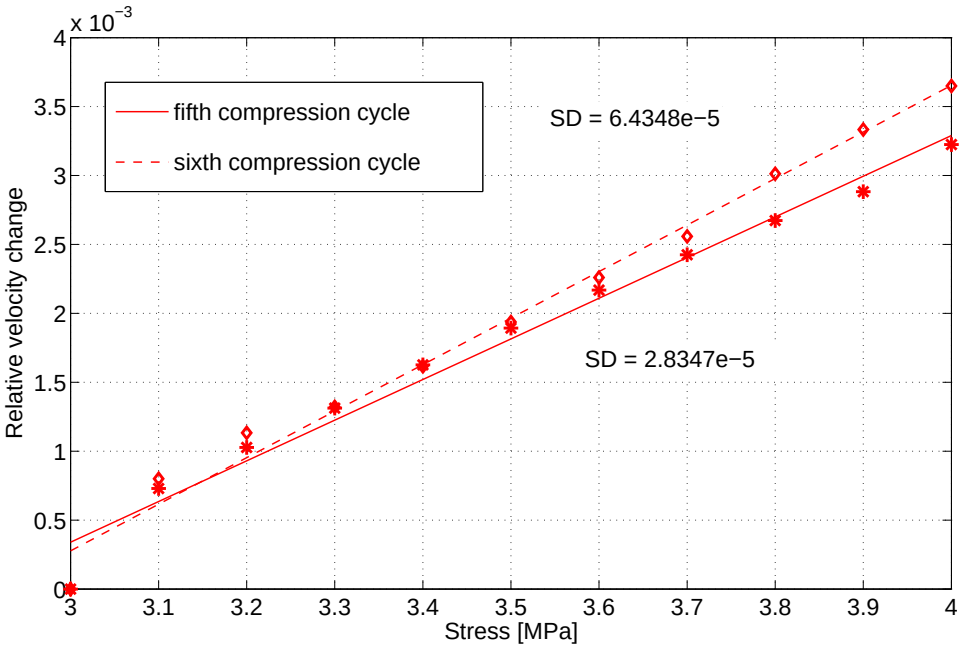

Figure 6.22: Cyclic Loading: Results of fifth and sixth compression cycle of LRS10.

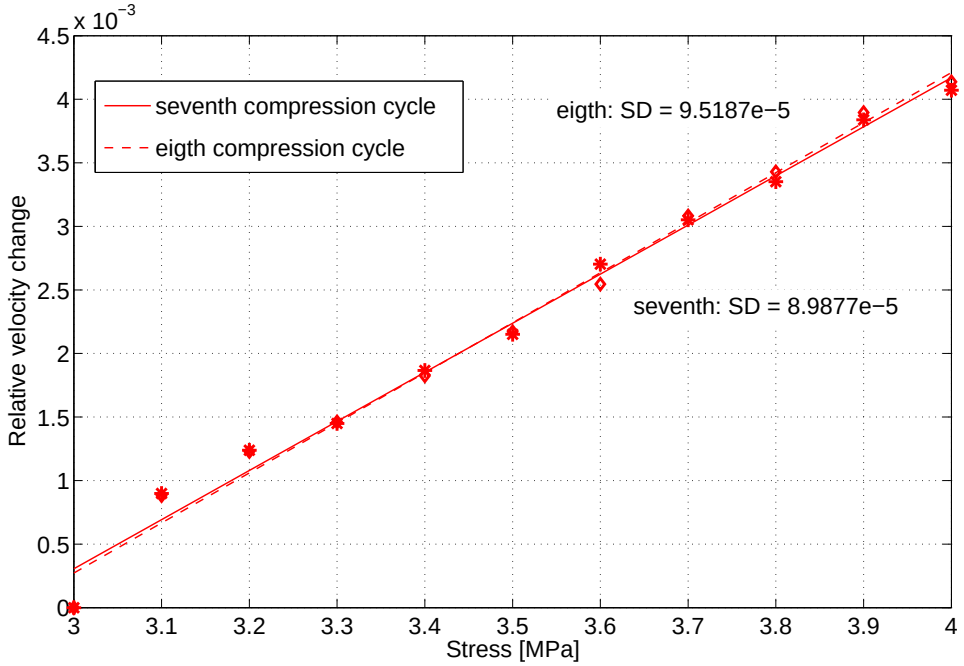

Figure 6.23: Cyclic Loading: Results of seventh and eighth compression cycle of LRS10.

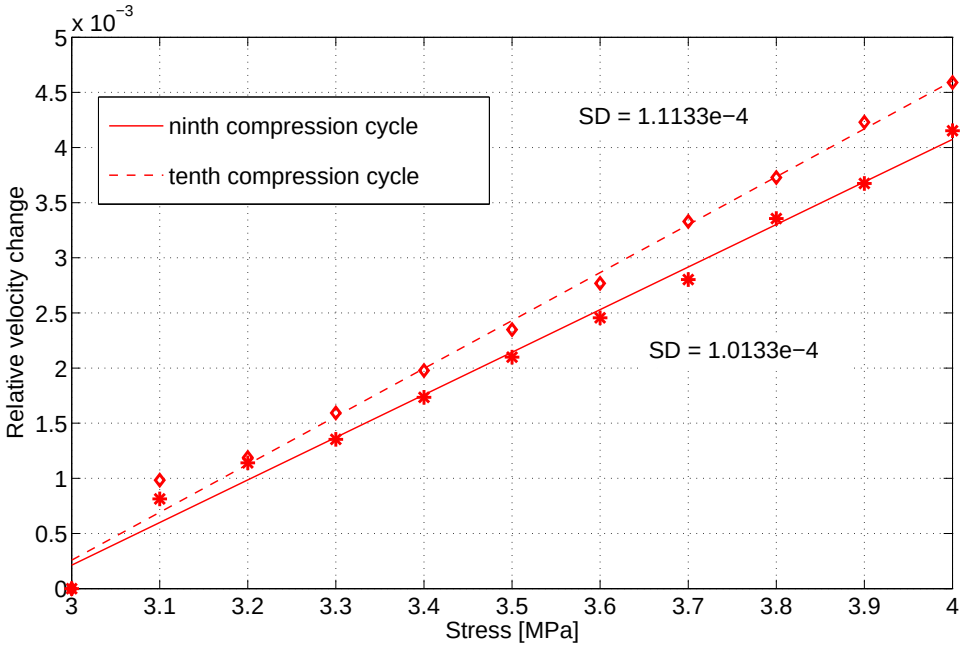

Figure 6.24: Cyclic Loading: Results of ninth and tenth compression cycle of LRS10.

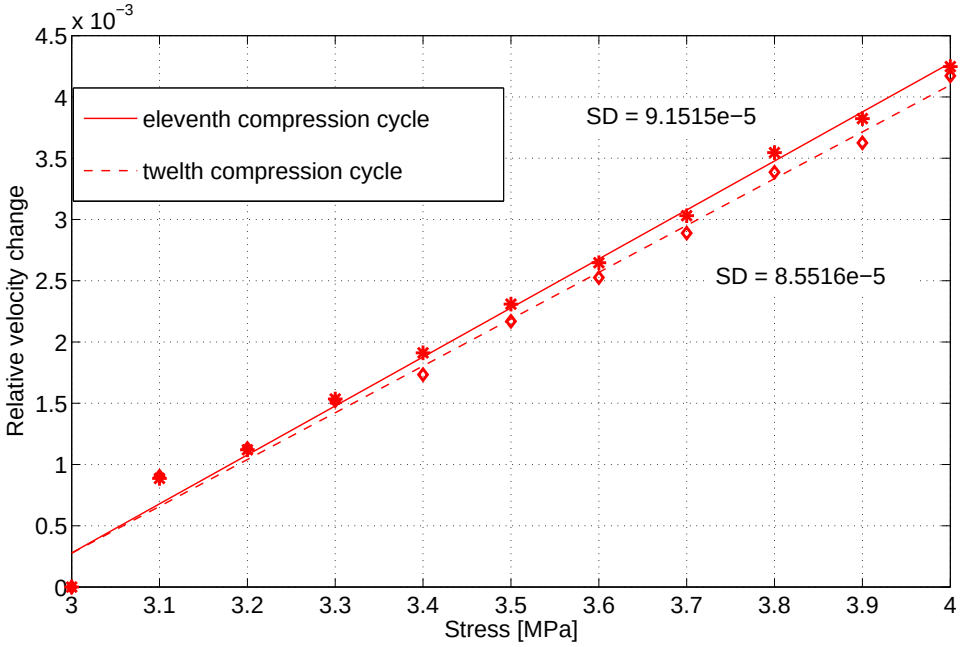

Figure 6.25: Cyclic Loading: Results of eleventh and twelve compression cycle of LRS10.

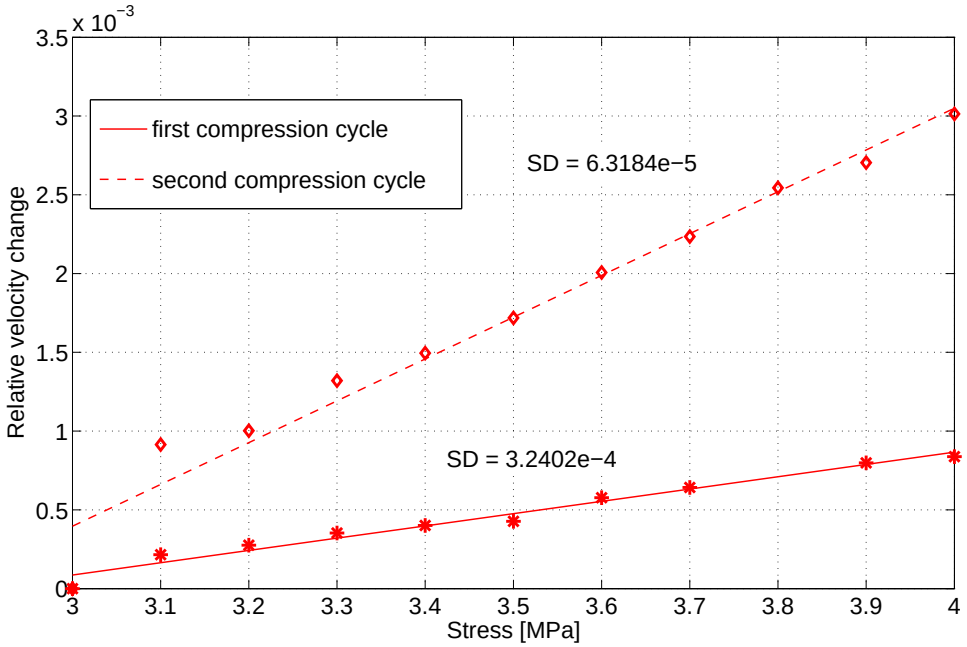

Figure 6.26: Cyclic Loading: Results of first and second compression cycle of LRS11.

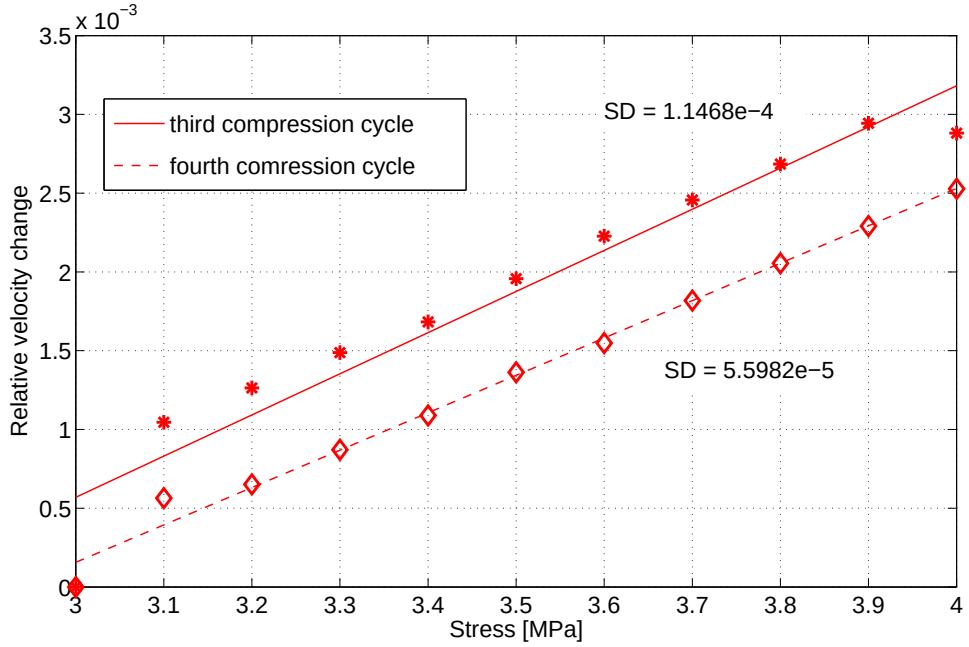

Figure 6.27: Cyclic Loading: Results of third and fourth compression cycle of LRS11.

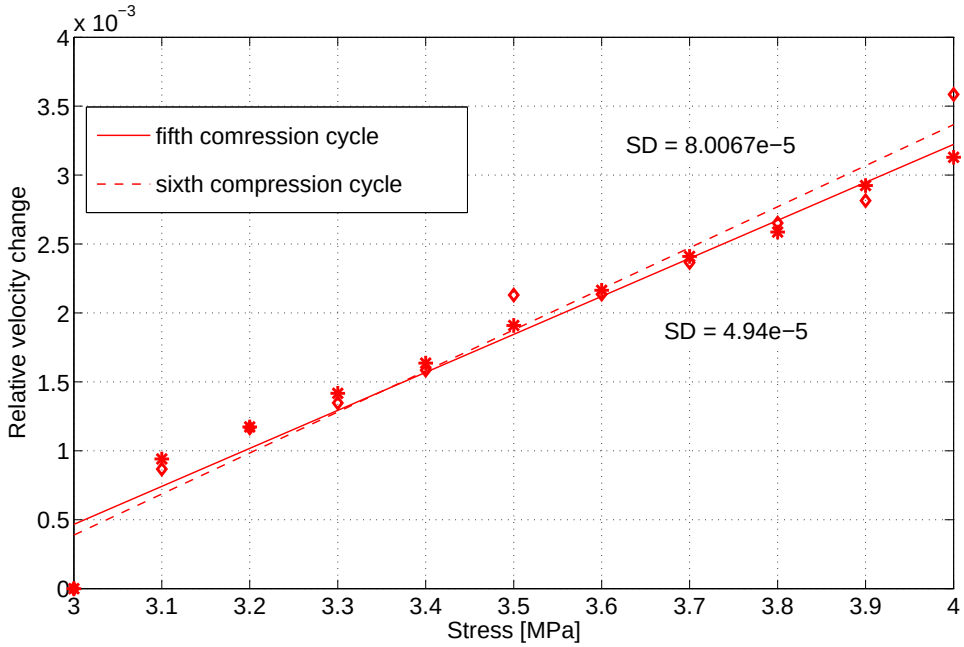

Figure 6.28: Cyclic Loading: Results of fifth and sixth compression cycle of LRS11.

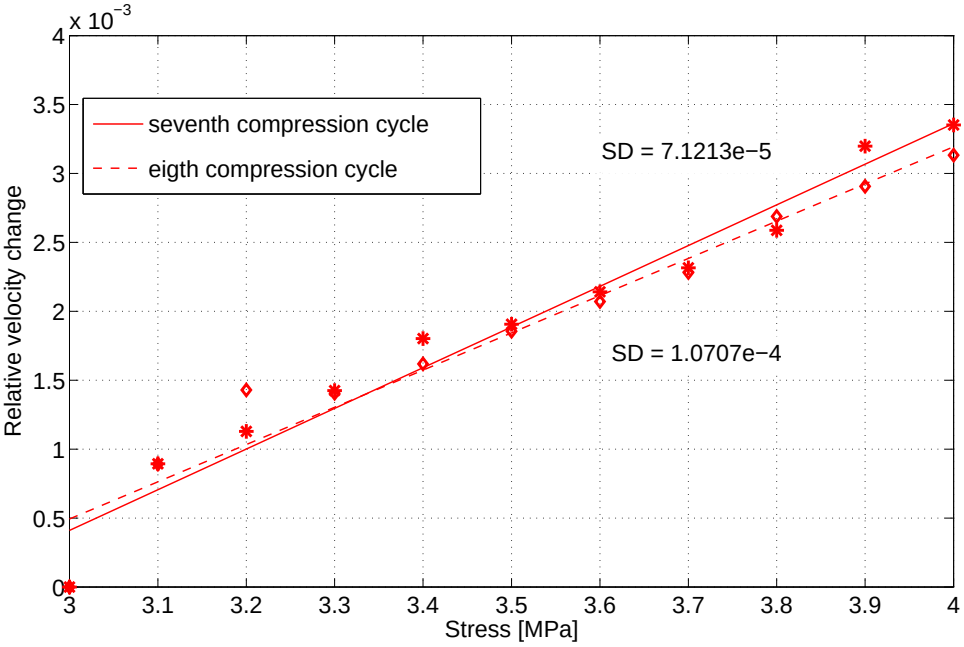

Figure 6.29: Cyclic Loading: Results of seventh and eighth compression cycle of LRS11.

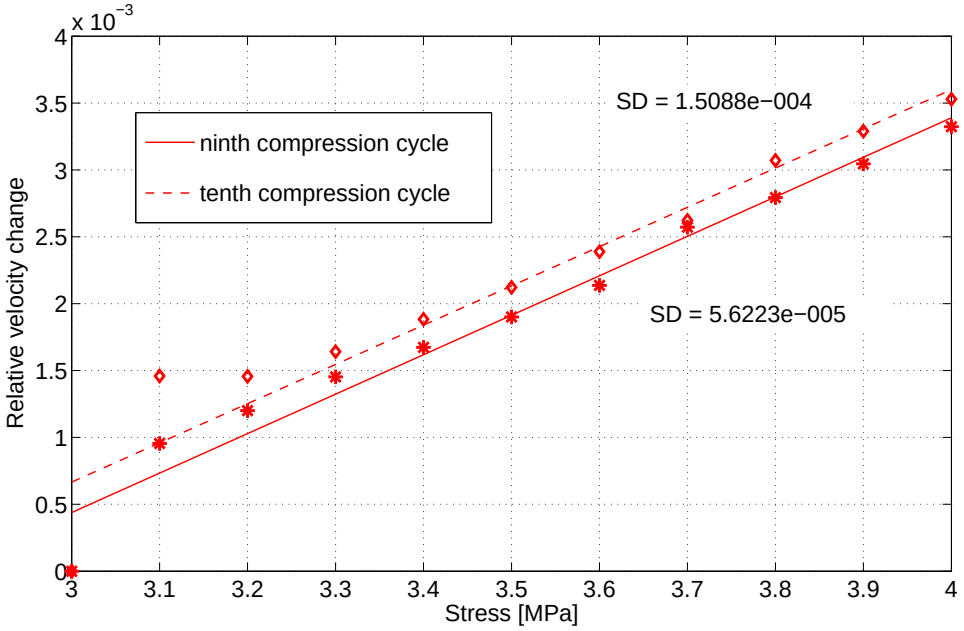

Figure 6.30: Cyclic Loading: Results of ninth and tenth compression cycle of LRS11.

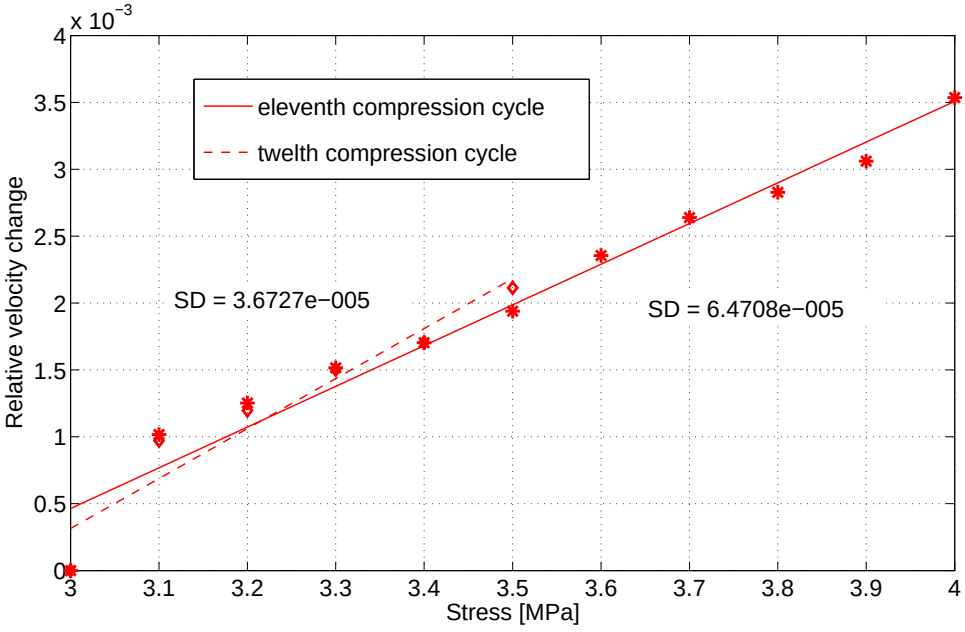

Figure 6.31: Cyclic Loading: Results of eleventh and twelfth compression cycle of LRS11.

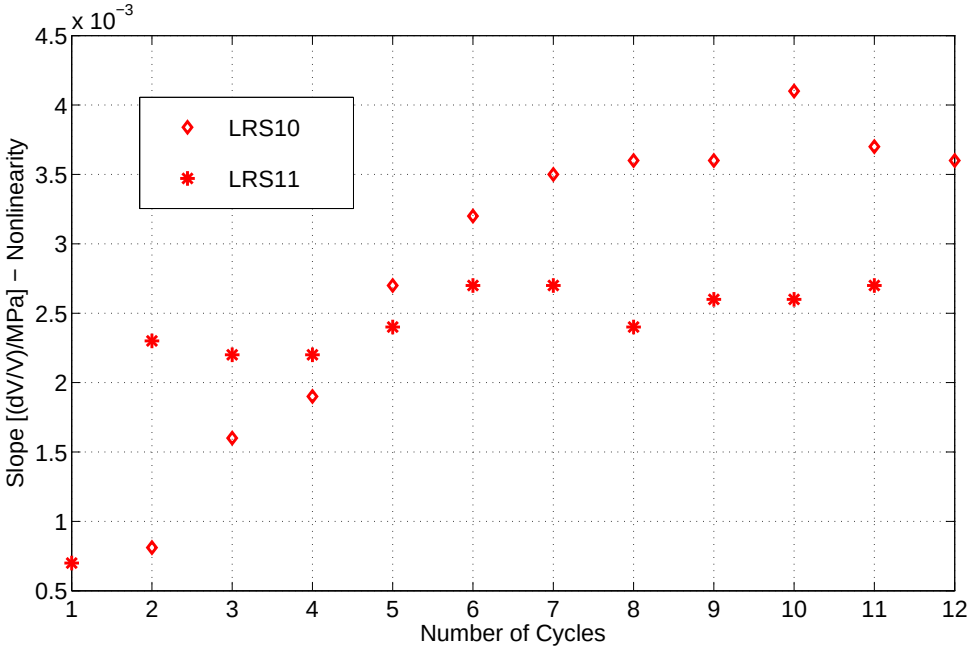

Figure 6.32: Cyclic Loading: Slopes over number of compression cycle for LRS10 and LRS11.

CHAPTER VII

CONCLUSION AND OUTLOOK

7.1 Conclusion

This research demonstrates that it is possible to distinguish between different types of damage in concrete samples in a reliable and reproducible fashion using the diffuse ultrasonic coda wave interferometry, and to use the slope, Φ as a measure of damage and nonlinearity. The procedure used in this research was shown to be very robust, not only because of the fixtures used for the source and receiver which ensured consistent coupling conditions, but rather because of the technique itself.

The resulting slopes measured for undamaged concrete sample show about the same values as presented in [27]. The slope results for the different damaged stages were typically multiple times higher of those at the undamaged stage. It was shown that all slopes are positive, and the slope increased with increasing damage level. The results of the thermal damage experiment show a clear increasing trend of nonlinearity Φ, and the increase in nonlinearity Φ seems to be higher than those for the two other loading/damage conditions. The slopes of the cyclic loading experiment start to saturate as the number of cycle increases, meaning that after a few cycles, there is not much change in the microstructure of the concrete specimens. The ASR damage experiments were conducted at the very beginning of ASR damage production. Nevertheless, some damage was introduced into the specimens, and the differences are visible in the result. The slopes of Fig. 6.19 show that ASR damage production is different from specimen to specimen, as expected. Depending on the location where ASR damage occurs, the amount of damage and the reactivity time differs between the specimens, resulting in a different slope increase as shown.

7.2 Outlook

The technique should be applied to characterize ASR damage through the whole period of degradation process since only the beginning of ASR damage process was monitored in this study.

Since the method proves to be capable of detecting damage, future work should concentrate on improving the experiment setup and on putting some research effort in the effect of different geometry and boundary conditions e.g. samples with different geometries and sizes as well as different transducer positons can be used. This will require improvements on the receiving side to still achieve a higher signal-to-noise ratio, maybe in the form of amplifying the input signal or using a longer signal which also improves the signal-to-noise ratio

Attempts should be made to use a laser interferometer on the receiving side. This would enable true point-like detection and would also eliminate coupling effects that will always be present using ultrasonic contact transducers. Unfortunately, a laser system was not at hand for this research and therefore could not be tested yet.

Different characterization techniques like microscopy can be used to independently validate the level of damage in each specimen. Since the slope represents a measure of damage, more damage is expected in samples with higher slopes.

All three damage types show an increasing in slope with an increasing in damage. It is very difficult to distinguish between each type of damage in real structures, when they are occurring simultaneously. Therefore, theoretical models for the prediction of damage type and/or portions of each damage type should be developed.

REFERENCES

[1] Achenbach, J. D., *Wave propagation in elastic solids*. North-Holland, 1973.

[2] Aki, K. *J. Phys. Earth*, vol. 4, p. 71, 1956.

[3] ASTM-International, "Standard terminology relating to concrete and concrete aggregates 09a."

[4] ASTM-International, "Standard test method for determination of length change of concrete due to alkali-silica reaction c 1293 08b," 2008.

[5] Baier, A., *Digitale signalangepasste Filter und Korrelatoren zur Detektion von Bandpasssignalen*. VDI-Verlag, 1987.

[6] Becker, J., , Jacobs, L. J., and Qu, J., "Characterization of cement-based materials using diffuse ultrasound," *Journal of Engineering Mechanics*, vol. 129, pp. 1478–1484, December 2003.

[7] Becker, J., "Investigation of the microstructure of hegerogeneous materials using ultrasonic waves," Master's thesis, Civil and Environmental Engineering, Georgia Institute of Technology, August 2002.

[8] Bendat, J. S., *RANDOM DATA - Analysis and Measurement Procedures*. John Wiley & Sons, Inc., second ed., 1986.

[9] Bentahar, M., Aqra, H. E., Guerjouma, R. E., Griffa, M., and Scalerandi, M., "Hysteretic elasticity in damaged concrete: Quantitative analysis of slow and fast dynamics," *Physical Review B*, vol. 73, 2006.

[10] Castillo, C., "Effect of transient high temperature on high strength concrete," Master's thesis, Rice University, 1987.

[11] Chen, X.-J., Kim, J.-Y., Kurtis, K., Qu, J., Shen, C., and Jacobs, L., "Characterization of progressive microcracking in portland cement mortar using nonlinear ultrasonics," *NDT&E International*, vol. 41, pp. 112–118, 2008.

[12] Cowan, M. L., Beaty, K., Page, J. H., Liu, Z., and Sheng, P., "Group velocity of acoustic waves in strongly scattering media: Dependence on the volume fraction of scatterers," *Physical Review E*, vol. 58, pp. 6626 – 6636, November 1998.

[13] Delsanto, P. P., ed., *Universality of Nonclassical Nonlinearity*. Springer, 2007.

[14] Deroo, F., "Damage detection in concrete using diffuse ultrasound measurements and an effective medium theory for wave propagation in multi-phase materials," Master's thesis, Civil and Environmental Engineering, Georgia Institute of Technology, December 2009.

[15] Deroo, F., Kim, J.-Y., Sabra, K. G., Qu, J., and Jacobs, L. J., "Detection of damage in concrete using diffuse ultrasound," *journal of the Acoustical Society of America*, vol. 127, p. 3315, June 2010.

[16] Duvall, T. L., Jeffferies, S. M., harvey, J. W., and Pomerantz, M., "Time-distance helioseismology," *Nature*, vol. 362, pp. 430–432, April 1993.

[17] Egle, D. M. and Bray, D. E., "Measurement of acoustoelastic and third-order elastic constants for rail steel," *Journal of the Acoustical Society of America*, vol. 60, p. 741 ff, September 1976.

[18] Graff, K. F., *Wave motion in elastic solids*. Dover Publications, 1973.

[19] Hadziioannou, C., Larose, E., Coutant, O., Roux, P., and Campillo, M., "Stability of monitoring weak changes in multiply scattering media with ambient noise correlaiton: Laboratory experiments," *Journal of the Acoustical Society of America*, vol. 125, pp. 3688 – 3695, April 2009.

[20] Hein, A., *Processing of SAR Data: Fundamentals, Signal Processing, Interferometry*. Springer, 2004.

[21] Hughes, D. S. and Kelly, J. L., "Second-order elastic deformation of solids," *Physical Review*, vol. 92, pp. 1145 – 1149, December 1953.

[22] Ideker, J. H., Easst, B. L., Folliard, K. J., Thomas, M. D. A., and Fournier, B., "The current state of the accelerated concrete prism test," *Cement and Concrete Research*, vol. 40, pp. 550–555, 2010.

[23] Jacobs, L. J. and Owino, J. O., "Effect of aggregate size on attenuation of rayleigh surface waves in cement-based materials," *Journal of Engineering Mechanics*, vol. 126, pp. 1124–1130, November 2000.

[24] Klieger, P. and Lamond, J. F., *Significance of tests and properties of concrete and concrete-making materials*. American Society for Testing and Materials, August 1994.

[25] Kurtis, K. E. and Monteiro, P. J. M., "Chemical additives to control expansion of alkali-silica reaction gel: proposed mechanisms of control," *Journal of Material Science*, vol. 38, p. 2027 2036, 2003.

[26] Larose, E., de Rosny, J., Margerin, L., Anache, D., Gouedard, P., Campillo, M., and van Tiggelen, B., "Observation of multiple scattering of khz vibrations in a concrete structure and application to monitoring weak changes," *Physical Review E*, vol. 73, pp. 016609–1 – 016609–6, January 2006.

[27] Larose, E. and Hall, S., "Monitoring stress related velocity variation in concrete with a 2x10?5 relative resolution using diffuse ultrasound (l)," *Journal of the Acoustical Society of America*, vol. 125, p. 4, April 2009.

[28] Larose, E., Roux, P., Campillo, M., and Derode, A., "Fluctuations of correlations and greens function reconstruction: Role of scattering," *Journal of Applied Physics*, vol. 103, 2008.

[29] Lobkis, O. I. and Weaver, R. L., "On the emergence of the greens function in the correlations of a diffuse field," *Journal of the Acoustical Society of America*, vol. 110, pp. 3011–3018, December 2001.

[30] Lobkis, O. I. and Weaver, R. L., "Coda-wave interferometry in finite solids: Recovery of p-to-s conversion rates in an elastodynamic billiard," *Physical Review Letters*, vol. 90, pp. 254–302, 2003.

[31] Lu, Y. and Michaels, J. E., "A methodology for structural health monitoring with diffuse ultrasonic waves in the presence of temperature variations," *Science Direct*, vol. 43, pp. 717–731, 2005.

[32] Malvern, L. E., *Introduction to the Mechanics of a Continuous Medium*. Prentice-Hall, 1969.

[33] Mamlouk, M. S. and Zaniewski, J. P., *Materials for Civiil and Construction Engineers*. Prentice-Hall, second ed., 2006.

[34] Mehta, P. and Monteiro, P., *Concrete - Microstructure, Properties and Materials*. McGrawHill, 3^{rd} ed., 2006.

[35] Page, J. H., Schriemer, H. P., Bailey, A. E., and Weitz, D. A., "Experimental test of the diffusion approximation for multiply scattered sound," *Physical Review E*, vol. 52, pp. 3106–3104, September 1995.

[36] Page, J. H., Schriemer, H. P., Jones, I. P., Sheng, P., and Weitz, D. A., "Classical wave propagation in strongly scattering media," *Physical Review A*, vol. 241, pp. 64–71, 1997.

[37] Payan, C., Garnier, V., Moysan, J., and Johnson, P. A., "Applying nonlinear resonant ultrasound spectroscopy to improving thermal damage assessment in concrete," *Journal of the Acoustical Society of America*, vol. 121, April 2007.

[38] Payan, C., Garnier, V., Moysan, J., and Johnson, P. A., "Determination of third order elastic constants in a complex solid applying coda wave interferometry," *Applied Physics Letters*, vol. 94, pp. 011904–1 – 011904–3, January 2009.

[39] Poupinet, G., Ellsworth, W. L., and Frechét, J., "Monitoring velocity variations in the crust using earthquake doublets: An application to the calaveras fault, california," *Geophysical Research*, vol. 89, pp. 5719 – 5731, 1984.

[40] Roberts, P. M., Phillips, W. S., and Fehler, M. C., "Development of the active doublet method for measuring small velocity and attenuation changes in solids," *Journal of the Acoustical Society of America*, vol. 91, pp. 3291–3302, June 1992.

[41] Rose, J. L., *Ultrasonic waves in solid media*. Cambridge University Press, 1999.

[42] Sens-Schönfelder, C. and Wegler, U., "Passive image interferometry and seasonal variations of seismic velocities at merapi volcano, indonesia," *Geopysical Research Letters*, vol. 33, November 2006.

[43] Snieder, R., Grt, A., Douma, H., and Scales, J., "Coda wave interferometry for estimating nonlinear behavior in seismic velocity," *Science*, vol. 295, pp. 2253 – 2255, March 2002.

[44] Steffen, A., *Digital Pulse Compression using Multirate Filter Banks*. Hartung-Gorre Verlag, 1991.

[45] TenCate, J. A., Smith, E., Byers, L. W., and Shankland, T. J., "Slow dynamics experiments in solids with nonlinear mesoscopic elasticity," *Nonlinear Acoustics at the Turn of the Millennium: ISNA 15*, vol. CP524, pp. 303 – 309, 2000.

[46] Tritthart, J., "Chloride binding in cement i. investigations to determine the composition of porewater in hardened cement," *Cement and Concrete Research*, vol. 19, pp. 586–594, 1989.

[47] Weaver, R. L. and Lobkis, O. I., "Ultrasonics without a source: Thermal fluctuation correlations at mhz frequencies," *Physical Review Letters*, vol. 87, pp. 134301–1 – 134301–4, September 2001.